Meteorology and Atmospheric Physics

Multi-Scale Numerical Simulations of the Synoptic Environment, Diablo Windstorm, and Wildfire Formation Mechanisms for the Tubbs Fire (2017)

--Manuscript Draft--

Manuscript Number:	MAAP-D-22-00177R2
Full Title:	Multi-Scale Numerical Simulations of the Synoptic Environment, Diablo Windstorm, and Wildfire Formation Mechanisms for the Tubbs Fire (2017)
Article Type:	Original Paper
Corresponding Author:	Yuh-Lang Lin, Ph.D. North Carolina Agricultural and Technical State University UNITED STATES
Corresponding Author Secondary Information:	
Corresponding Author's Institution:	North Carolina Agricultural and Technical State University
Corresponding Author's Secondary Institution:	
First Author:	Jackson T. Wiles, M.S.
First Author Secondary Information:	
Order of Authors:	Jackson T. Wiles, M.S.
	Yuh-Lang Lin, Ph.D.
	Michael L. Kaplan, Ph.D.
Order of Authors Secondary Information:	
Funding Information:	Directorate for Geosciences (1900621) — Prof. Yuh-Lang Lin
	Directorate for Geosciences (2022961) — Prof. Yuh-Lang Lin
Abstract:	The Advanced Research Weather Research and Forecasting (WRF-ARW) model was used to simulate the downscale evolving atmospheric dynamical processes conducive to the intensification and propagation of the Tubbs Fire (2017). This wildfire impacted Napa and Sonoma Counties, California, spreading quickly and erratically through complex mountainous terrain due in large part to downslope Diablo Winds. The Tubbs Fire spread over 36,000 acres and destroyed 5,636 structures, killing 22. The simulations and supporting observations during the pre-Diablo Wind period indicate a well-defined inverted surface trough in Northern California's Central Valley, along with a strong amplifying trough in the mid-troposphere and attendant cold frontogenesis over the Sierra Nevada. Mid-upper tropospheric jet streak flow, along with simulated and observed soundings from Reno, Nevada, indicate a mid-upper tropospheric jet indirect, exit-region, descending, secondary circulation in conjunction with lower-mid tropospheric cold air advection caused by the southwestward low-level jet under the upper-level jet's entrance region. These adjustments enabled the organization of a deepening and ascending inversion over the Sierra Nevada, as well as a self-induced wave critical layer between 850 hPa and 700 hPa prior to Diablo Wind formation. As the organizing jet streak departed, the discontinuously stratified atmosphere over the Sierra Nevada and coastal mountains in Northern California provided a favorable environment for mountain wave amplification. Intensifying leeside sinking motion coupled with wave steepening resulted in strong downslope winds in Northern California. Upward propagating mountain waves are present coinciding with the steepening of the isentropic surfaces consistent with the resonant interaction of nonlinear gravity waves. The model also simulated the development of a hydraulic jump in the lower troposphere on the lee side of the mountain range during Diablo Wind development. The simulation and observations indicate that favorable environment for Diablo Winds resulted from the baroclinic jet-front system propagating over the Sierra Nevada when it produced a highly discontinuously stratified

	atmosphere favorable for nonlinear mountain wave amplification. However, the main surge of momentum down the leeside is only indirectly coupled with the jet streak's exit region, being the result of cold frontogenesis, which allows for vertically differential cold air advection and its attendant discontinuously stratified vertical atmospheric structure.

COMMENTS TO THE AUTHOR:

Reviewer #1: I reviewed this paper one more time in this round of the revision.
And, I found that the revised paper has been improved significantly after the authors have been addressing all of the reviewers' comments and suggestions during the first round of the revision process.
The authors showed that the synoptic and meso-alpha scale processes related to the influence of jet stream is not the direct cause for the Diablo windstorm related to the Tubbs Fire.
Additional analyses and figures confirmed that the background condition of cold frontogenesis provides strong northeasterly flow across the Sierra Mountains in north California in lower-level.
They focused on two mesoscale processes. 1) Hydraulic jump mechanism and 2) Wave induced self critical level. As suggested below, there are three minor points that need to be address in the revised manuscript before it will be published in the journal.

1) For Hydraulic jump mechanism, they focused on hydraulic jump patters in the lee of Sierra Nevada mountain range and coastal mountains in north CA. Here, I suggest them to discuss more about the flow separation suggested by Smith (1985).
Smith, R. B. (1985). On severe downslope winds. Journal of the Atmospheric Sciences, 42(23), 2597-2603. https://doi.org/10.1175/1520-0469(1985)042<2597:OSDW>2.0.CO;2

Thank you for this comment. More details have been included regarding flow separation and minor revisions have been made to better represent the meaning of the Hydraulic Jump Theory.

2) For Wave induced self critical level, I see that there are wind reversal in sounding at Reno, NE. This seems to provide a favorable condition for strong turbulent flows below background critical level (Lane et al. 2009).
I believe those can help provide more reasonable condition for flow separation and bores in the lee side of mountains.
Lane, T. P., J. D. Doyle, R. D. Sharman, M. A. Shapiro, and C. D. Watson, 2009: Statistics and dynamics of aircraft encounters of turbulence over Greenland. Mon. Wea. Rev., 137, 2687-2702, https://doi.org/10.1175/2009MWR2878.1.

Thank you for this comment. This reference has been included and briefly discussed in the "Key Windstorm Theories and Mesoscale Dynamics" section.

3) Combination of those can help rapid intensification of wave amplification and strong downslope windstorms with hydraulic jump? I suggest one reference (Shin et al. 2022) regarding the classification of synoptic patterns related to mesoscale mechanisms of local downslope windstorm in Korea, which can be a reference need to be included in the discussion and conclusion for future study of the relationship of Diablo winds and Synoptic patterns.

Shin, Y., J.-H. Kim*, H.-Y. Chun, W. Jang, and S.-W. Son, 2022: Classification of Synoptic Patterns for Downslope Windstorms in Korea using the Self-Organizing Map. J. Geophys. Res-Atmos., 127, e2021JD035867, https://doi.org/10.1029/2021JD035867.

Thank you for the comment. This reference has been added in the appropriate place and allows for future scientific exploration.

Reviewer #2: I would like to thank the author for carefully addressing all reviewers comments from the previous round of review. I believe the paper is now in good shape with several valuable findings and insights for the studied events. The paper, for the first time, provides mesoscale analysis using both observational data sources and simulations. This approach has offered some valuable findings to better understand the weather condition during the event. I just have a few editorial comments for the author. I suggest accept after minor revision.

1) Line 115: It is not cleared what is "the threshold"

Thank you for the comment. The sentence has been adjusted to demonstrate that “the threshold” refers to the minimum Diablo Wind criteria.

2) Line 238: this sentence is problematic. "reanalysis" data is not needed to initialize WRF. Forcing data is needed to initialize WRF simulation such as ERA5, GFS, and HRRR.

Thank you. I understand the confusion and misrepresentation. The sentence has been corrected per your recommendation.

3) Lines 228 to 236: I would recommend to move these cross sections description to the results where the cross sections are going to be discussed for an easier to follow text.

I agree with this recommendation. It is now easier to read when the cross-sectional descriptions are included prior to the discussion of the results instead of in the methods section. Figure numbers have been updated to correspond to this change.

4) Section 2.2: The authors should add proper reference for ERA5 data.

Thank you for pointing this error out. A proper reference for ERA5 data has now been included in the reference section as well as in text citation.

5) Line 364: the sentence should be revised to a proper academic English sentence.

Thank you for this suggestion. The sentences starting on lines 363, 364, and 365 have all been modified.

Multi-Scale Numerical Simulations of the Synoptic Environment, Diablo Windstorm, and Wildfire Formation Mechanisms for the Tubbs Fire (2017)

Jackson T. Wiles[1], Yuh-Lang Lin[1, @], Michael L. Kaplan[2]

[1]Department of Physics and

Applied Science & Technology Ph.D. Program

North Carolina A&T State University, NC 27411, USA

[2] Division of Atmospheric Sciences,

Desert Research Institute

Reno, NV USA

Meteorology and Atmospheric Physics

https://doi.org/xxxxxxxxxx

Submitted: 21 November 2022

Revised: 17 October 2023

[@]Corresponding author address: Dr. Yuh-Lang Lin, 302H Gibbs Hall, North Carolina A&T State University, 1601 E. Market Street, Greensboro, NC 27411. Email: ylin@ncat.edu

KEY WORDS Tubbs Fire (2017), Diablo Winds, Severe Downslope Winds, Complex Terrain, Numerical Modeling, Advanced Research Weather Research and Forecasting (WRF-ARW) model

ABSTRACT

The Advanced Research Weather Research and Forecasting (WRF-ARW) model was used to simulate the downscale evolving atmospheric dynamical processes conducive to the intensification and propagation of the Tubbs Fire (2017). This wildfire impacted Napa and Sonoma Counties, California, spreading quickly and erratically through complex mountainous terrain due in large part to downslope Diablo Winds. The Tubbs Fire spread over 36,000 acres and destroyed 5,636 structures, killing 22. The simulations and supporting observations during the pre-Diablo Wind period indicate a well-defined inverted surface trough in Northern California's Central Valley, along with a strong amplifying trough in the mid-troposphere and attendant cold frontogenesis over the Sierra Nevada. Mid-upper tropospheric jet streak flow, along with simulated and observed soundings from Reno, Nevada, indicate a mid-upper tropospheric jet indirect, exit-region descending, secondary circulation in conjunction with lower-mid tropospheric cold air advection caused by the southwestward low-level jet under the upper-level jet's entrance region. These adjustments enabled the organization of a deepening and ascending inversion over the Sierra Nevada, as well as a self-induced wave critical layer between 850 hPa and 700 hPa prior to Diablo Wind formation. As the organizing jet streak departed, the discontinuously stratified atmosphere over the Sierra Nevada and coastal mountains in Northern California provided a favorable environment for mountain wave amplification. Intensifying leeside sinking motion coupled with wave steepening resulted in strong downslope winds in Northern California. Upward propagating mountain waves are present coinciding with the steepening of the isentropic surfaces consistent with the resonant interaction of nonlinear gravity waves. The model also simulated the development of a hydraulic jump in the lower troposphere on the lee side of the mountain range during Diablo Wind development. The simulation and observations indicate that the favorable environment for Diablo Winds resulted from the baroclinic jet-front system propagating over the

55 Sierra Nevada when it produced a highly discontinuously stratified atmosphere favorable for
56 nonlinear mountain wave amplification. However, the main surge of momentum down the leeside
57 is only indirectly coupled with the jet streak's exit region, being the result of cold frontogenesis,
58 which allows for vertically differential cold air advection and its attendant discontinuously
59 stratified vertical atmospheric structure.

60

1. Introduction

The Tubbs Fire, which began on October 8, 2017, at 9:45 pm local time, proved to have a precursor environment conducive to wildfire formation. Due in part to the excessively dry conditions at the surface, the Tubbs Fire grew uncontrollably and consumed over 36,000 acres and 5,636 structures in Napa and Sonoma Counties, California (CA) before being extinguished on October 31, 2017 (Martinez et al., 2017; Mohler, 2018). Economic losses from the Tubbs Fire approached $1.3 billion, as well as killing 22. Upon investigation, it was found that the Tubbs Fire began from privately owned electrical equipment which failed. However, because of the placement of the Tubbs Fire in the above-mentioned counties, as well as the environmental conditions in place, complex terrain interactions exist. Because of environmental conditions sustaining the wildfire, the complex terrain allowed for rapid growth and intensification which leads us to the primary scientific problem in this study, to examine the impacts of the complex terrain surrounding the above-mentioned counties.

(a) Orographic Effects

California provides an abundance of changing orographic elevations ranging from the coasts bordering the Pacific Ocean to the Sierra Nevada Mountain Range along its eastern border with Nevada. Because of this vast difference in elevation, California proves to have a very complex topographic landscape. Figure 1 depicts the key geographical features for this study. The Sierra Nevada Mountain Range is located to the east of Sacramento near the Nevada border, while the Coastal Mountain Range is just inland from the Pacific Ocean where the Tubbs Fire began. In between is the Central Valley extending along a north-northwest to east-southeast axis separating the two terrain features. Because of the vast change of landscape in California, there exists three damaging windstorms which prove to be conducive to wildfire formation. These

84 windstorms are named the Santa Ana, Sundowner, and Diablo winds. The Santa Ana winds
85 (SAW) can be found in Southern California, which can reach wind gusts as high as 27 ms^{-1} (~60
86 mph). In addition, SAW events occur from mid to late morning and peak during the months of
87 November to February respectively (Smith et al., 2018). For Sundowner winds which are unique
88 to the Santa Barbara region in Central California, they initiate in late afternoon/early evening and
89 have northerly winds exiting from the Santa Ynez mountains to the coast which always has the
90 coastal jet present (Hatchett et al., 2018). Finally, the Northern California wind event that affected
91 the Tubbs Fire is known as the Diablo winds (DW) (e.g., Mass and Ovens, 2019) and occurs in
92 the early morning hours during the fall, winter, and spring months with a peak intensity in
93 October. DWs exhibit characteristics of excessively hot, dry, gusty winds and are defined as 1)
94 wind speeds greater than or equal to 11.17 ms^{-1} (~25 mph), 2) wind between 45 and 22.5 degrees
95 (NE-NNE direction), 3) relative humidity (RH) less than 30%, and 4) at least a three-hour duration
96 (Smith et al., 2018). These characteristics represent air parcels undergoing adiabatic compression
97 as the flow resonates over the lee slopes of mountain ranges. In addition, Smith et al. (2018)
98 performed a climatological study for DWs employing data from January 1, 1999, through January
99 1, 2018. This data focused on the Northern California region from several remote automated
100 weather stations (RAWS). The location for the RAWS network for this study is presented in
101 Figure 2. During their study, two DW events were separated and examined due to the intensity
102 and later significance of the events. The necessary conditions and characteristics of the DWs were
103 met and the events occurred in November 2013 and October 2017 respectively. Results of this
104 study are presented in Figure 3 with the following color code for panels (a), (b), and (c), (d). In
105 the (a) and (b) panels, the North Bay wind velocity is represented by the red contours while the
106 wind velocity gusts are green. Additionally, the wind velocity in the Sierra Nevada area is given

in the dark blue lines, while the wind velocity gusts are represented by the light blue lines. For panels (c) and (d), RH is denoted as red for the North Bay region and blue for the Sierra Nevada region. In the case of November 2013, there was a rapid increase of wind velocity and drop of RH which exceeded the DW criteria (see panels a and c). Furthermore, the RH values began falling at the onset of the DW event as seen in Figure 3. On the 21st 00 UTC, RH values were observed to be near 100%, then by the 22nd 00 UTC, RH values were below the threshold of 30% and remained there through the 24th 00 UTC. For plots (b) and (d), which represent the Tubbs Fire event of October 2017, the DW event was short-lived, but met the DW criteria. On October 8th between 12 UTC and October 9th 00 UTC, there was a rapid increase in wind velocity which far exceeded the minimum DW criteria. Also, the RH values met the minimum requirement of less than 30%. However, there was not a sharp drop in RH at the onset of this DW event due to the environment being preconditioned with little to no moisture. As this event ended on October 9th at 12 UTC, the wind values returned below the minimum velocity threshold of 11.17 ms^{-1} (Smith et al., 2018; Plymouth State University (PSU), 2022). Therefore, as discussed above, DWs can ultimately impact the precursor environment to wildfire events and highly influence their behavior.

(b) Key Windstorm Theories and Mesoscale Dynamics

Clark and Peltier (1984), describe nonlinear effects associated with mountain waves to explain how drastic increases in wind speeds form on the lee slopes of mountain ranges known as downslope windstorms. In their nonlinear numerical experiments, a wave-breaking region aloft was identified, otherwise known as a self-induced wave critical level. In this wave-breaking region, a wind reversal occurs, and the critical level will act as an internal boundary reflecting the propagating mountain waves from the surface upwards back towards the surface, which will

produce a type of severe wind state through partial resonance with the upward propagating mountain waves (Clark and Peltier, 1984). Clark and Peltier found three distinct stages for the development of severe downslope winds, later to be known as the Resonant Amplification Theory. The first of which is a local static (buoyancy) instability. From the static instability, a well-mixed region of air aloft will appear. Second, from this static instability, a well-defined stationary disturbance, which is large in amplitude will be generated over the lee slopes of the mountain. Third, this region of enhanced wind on the lee slopes of the mountain will eventually expand and progress downstream from the initial flow. Therefore, what once was static instability now evolves into Kelvin-Helmholtz instability. This new instability will dominate the mature form of the severe wind state and as mentioned in Lane et al. (2009), below the self-induced wave critical level, conditions become favorable for turbulent flow. This newly formed turbulent flow is due in part to wave instability and wave breaking as nonlinearity of the waves maximize. A complete summary of the Resonant Amplification Theory can be found in Lin (2007).

Smith (1985) proposed the Hydraulic Jump Theory regarding the generation of a severe downslope wind event (see Lin (2007) for a brief summary) that may be considered as the mature form of the Resonant Amplification Theory. The research attributed a high-drag (severe-wind) state to the interaction between a smoothly stratified flow and a turbulent "dead" region known as well-mixed air aloft. In this region of well-mixed air, density becomes constant throughout the layer and when a high-drag state develops, a dividing streamline surrounds the well-mixed air region at a certain level. According to Smith (1985), below this dividing streamline, the flow is considered to be smooth, steady, nondissipative, hydrostatic, and Boussinesq. This would be the analog to the self-induced wave critical level. It was determined from numerical modeling that the descent of the lower dividing streamline would begin over the mountain's base. Considering

153 the basic wind flow, one assumes that it becomes subcritical, meaning the flow velocity would be
154 less than the wave velocity itself, as it ascends to the mountain peak. When this basic wind flow
155 achieves the peak of the mountain, the flow transitions into a supercritical flow and the slope of
156 the dividing streamline increases. Therefore, it is often seen that the supercritical flow is greatest
157 near the surface, as wind speeds increase drastically. Then, this high-drag state is confined to a
158 relatively short distance away from the leeward side of the mountain before being corrected back
159 to the initial streamline height (hydraulic jump). Once the severe wind state on the lee side of the
160 mountain ends, the dividing streamline becomes ambiguous, or poorly defined, signaling an end
161 to the uniform density. Thus, the dividing streamline completely encompasses the region of well-
162 mixed air of uniform density and gives a good representation of a mature downslope windstorm
163 (Smith, 1985). We will compare both windstorm theories to the evolution of DWs prior to the
164 Tubbs Fire. Note that these mechanisms could be strongly influenced by synoptic patterns (Shin
165 et al., 2022).

166 ***(c) Polar Jet Influence on Severe Downslope Windstorms***

167 Another issue we examined is the relationship between jet forcing and severe downslope
168 wind formation, as proposed in Huang et al. (2009). In this study, we will focus on a comparison
169 to the published Huang, Lin, Kaplan, and Charney (HLKC) theory. HLKC found that the polar
170 jet would play a significant role in severe-downslope windstorm development in the case of the
171 Cedar Fire (2003). The HLKC theory can be understood through their conceptual model, as
172 illustrated in Figure 4. For extended details, the readers are referred to Huang et al. (2009) and
173 Karim et al. (2022). We will present a brief review of the HLKC theory below.

174 In this conceptual model, there were three specific stages of evolution in the polar jet.
175 Stage I, (Fig. 4a) shows the polar jet is initially positioned over the mountainous terrain with

176 strongest wind speeds on the 300 hPa isobaric surface and a well-defined jet streak with a four-
177 cell pattern indicating the entrance and exit regions' transverse ageostrophic secondary
178 circulations accompanying rising and sinking cells as defined in Uccellini and Johnson (1979).
179 In terms of low-level wind adjustments, the entrance region is critical under which thermal
180 advection occurs when considerably cold air is poleward of the jet. In this progression of the cold
181 front in Fig. 4a, the air mass behind the front is affected by isallobaric ageostrophic adjustments
182 intensifying the downstream-directed pressure gradient force in time, under the entrance region
183 creating a low-level jet return branch in the same direction as the movement of the dry cold front.
184 From this adjustment, low-level moisture divergence and cold air advection will occur over the
185 mountain tops enhancing the static stability directly above the cold air advection in the mid-
186 troposphere. During Stage II (Fig. 4b), the cold frontal system propagates downstream, and the
187 jet streak aloft begins to be positively tilted as deep cold air advection ensues suppressing rising
188 motion enhancing the descent of air parcels, upper-level air will descend through the mid to lower
189 troposphere reaching the mountain summits. Finally, in Stage III (Fig. 4c), the jet streak curvature
190 aloft reaches a maximum, which couples to, and modifies, the transverse circulation of the
191 ageostrophic winds resulting in a dominant along-jet sinking motion from the jet exit region
192 towards the surface. Near the mountain top, mesoscale subsidence will occur resulting in the
193 redirection of the wind flow towards the leeward slope. Once this descending air mass reaches
194 the farthest leeward slope of the mountain range, a severe downslope wind event occurs and
195 creates a hydraulic jump. Therefore, this polar jet and its embedded jet streak would play a
196 significant role in severe downslope windstorm development, given that the jet is positioned close
197 enough above the high wind state at the surface.

198 *In this study we will try to apply this paradigm to the structure and evolution of the*
199 *environment leading up to the DW event prior to the Tubbs Fire.*

200 ***(d) Bore Genesis Influence on Severe Downslope Windstorms***

201 Finally, as will be shown in the results of the manuscript, DWs can spawn additional
202 propagating wave phenomena such as bores that may affect the wildfire environment. In
203 Karyampudi et al. (1994), a schematic representation of a quasi-stationary hydraulic jump and
204 bore genesis was presented focusing on the severe weather outbreak of April 13-14, 1986. The
205 most notable feature about the bore is that it will propagate against the background wind flow.
206 The original air mass of the bore at the surface will be displaced aloft and attain buoyancy for a
207 short time before descending back to the surface. Therefore, the bore would likely enhance the
208 movements of the air mass at the surface as it progresses away from the hydraulic jump. This
209 would cause a region of secondary momentum flux as well as cooling/warming and likely be
210 attributed to higher windspeeds due to constriction of the air column at the surface (Karyampudi
211 et al., 1994). These effects of bore genesis will be further explored in the case of the Tubbs Fire.

212 In section 2, we will describe the analysis, datasets, and numerical experiments. We will then
213 describe analyses of the observed and simulated synoptic environment in section 3 and mesoscale
214 numerical simulations of the Tubbs Fire environment focusing on how that environment generates
215 mountain wave-induced downslope winds in section 4. Additional discussion of the simulated
216 fields and their significance for the Tubbs Fire environment will be included in section 4. A
217 discussion and conclusions will be given in section 5.

2. Numerical Model Description and Experimental Design

2.1 Domain Configurations

The Weather Research and Forecasting model's (WRF) Advanced Research WRF (WRF-ARW) version 4.0 was employed for numerical simulations. The domain configuration for this study is shown in Figure 5. The synoptic-scale domain (D01) covers the central and western United States along with the southern areas of Canada. Also, the nested domains, domain 2 (D02) and 3 (D03), allow for refined analysis on the mesoscale. D02 covers the western U.S. and gives way to transition to D03 which resolves the mesoscale features of the environment leading to the formation of the wildfire. From this configuration, the multi-scale dynamics of the environment conducive to the Tubbs Fire (2017) formation will be studied. In Table 1, the specific domain setups and configurations are listed in detail. Additionally, a time step of 60 seconds was used with a parent grid ratio of four for both D02 and D03 along with 50 vertical levels. Also, USGS terrain data was used to satisfy the static geographical data need. Lastly, the following parameterizations and schemes were used while running WRF-ARW simulations: Microphysics – Purdue-Lin; Longwave Radiation – RRTM longwave scheme; Shortwave Radiation – RRTMG shortwave scheme; Surface Layer Physics – Mellor-Yamada-Janjic (Eta) TKE; Land Surface Physics – Unified Noah Land Surface Model; Planetary Boundary Layer Physics – Mellor-Yamada-Janjic scheme; Cumulus Physics (D01 only) – Kain-Fritsch (new Eta) scheme. For detailed descriptions of each scheme used and their references, refer to ARW user manual (Skamarock et al., 2019).

2.2 ECMWF ERA5 Dataset and Graphical Analysis Software

In addition to the domain configuration above, forcing data is needed to initialize the WRF-ARW model. The European Centre for Medium Range Weather Forecasts (ECMWF) ERA5 dataset was employed. ERA5 offers 137 hybrid sigma/pressure levels with the top level reaching

241 0.01 hPa along with 37 interpolated pressure levels, 16 potential temperature levels and one
242 vorticity level. In terms of resolution, ERA5 has a parent resolution of 31km (0.28125 degrees).
243 With this high resolution, interpolation down to 16 km for D01, all the way down to 1 km
244 resolution for D03, as was done for this study, provides substantial accuracy in defining the initial
245 state. Both atmospheric surface and pressure level data can be downloaded from the NCAR UCAR
246 Research Data Archive website (ECMWF, 2019).

247 Finally, to generate graphical output of the WRF-ARW simulations, third party software, such
248 as the NCAR Command Language (NCL) was used, which is specifically for processing,
249 manipulating, reading, writing, and visualizing atmospheric modeling data. More information can
250 be found at ncl.ucar.edu (Mass and Ovens, 2019).

251 **3. Observational and Multi-scale Analyses Results**

252 The observational analysis will be based on the NOAA Storm Prediction Center (SPC) RUC
253 analyses datasets (NOAA, 2022). Also, observed vertical profiles of the atmosphere will be shown
254 from the University of Wyoming sounding archive (Oolman, 2022). Subsequently, WRF-ARW
255 simulated results will be presented to better understand the multi-scale environment leading up to
256 the wildfire event.

257 ***3.1 NOAA SPC Analysis***

258 In Figure 6(a), the NOAA SPC analysis on October 9th, at 03 UTC shows a well-defined upper-
259 level trough and its associated cold front over Western California as inferred from the temperature
260 gradient in the red and blue dashed contours. In addition, the geopotential height contours in black
261 indicate low heights in the areas surrounding the upper-level trough with the lowest height being
262 in the vicinity of the highest mean RH through the 700-500 hPa layer (fill). Also, in Northern
263 California, there is a very strong temperature gradient along the spine of the Sierra Nevada

consistent with heights that support a south-westward-directed pressure gradient conducive to increasing the south-westward directed wind velocity. The conditions listed above indicate a cold frontal passage sweeping through the western U.S. with the poleward component of the front impinging on north-eastern California. Accompanying this frontal motion, Northern California's wind velocity increases along with the wind direction shifting to the northeast. The cold air advection provides enhanced downward motion consistent with quasi-geostrophic theory. This downward motion will result in adiabatic compression of air parcels, strengthening the stable stratification, and enhancing the near surface wind speed as high momentum aloft sinks surfacewards.

There is a strong northeast-southwest temperature gradient (warm air in red dashed contours) in both Figure 6a and 6b over Northern California. This is consistent with horizontal frontogenesis that occurred by October 9th at 03 UTC. From the dew point temperature in Figure 6b (fill), it can be concluded that over Northern California, trivial moisture exists in the lower troposphere. Consistent with this dry air, one could infer a thermally indirect secondary circulation established by the jet's right exit region with sinking motion in the warm air accompanying mass convergence aloft and mean sea level pressure rises. Further support for a thermally indirect jet secondary circulation is found in Figure 7. As shown, much of Utah, Nevada, and California experience sinking motion due to integrated mass convergence accompanying the thermally indirect jet secondary circulation. In addition, Figure 8 indicates rightward directed ageostrophic vectors in the vicinity of Northern California and an overall mid-tropospheric descent of relatively high potential temperature air strengthening the front in phase with this ageostrophy. These adjustments are consistent with semi-geostrophic mass convergence aloft in the right exit region extending from Central Nevada through Central California, shown in Figure 8b. Therefore, the isentropes are

directly forced downward over the mountains. Then, to the northeast of the Sierra Nevada the strengthening southwest-directed low-level pressure gradient is enhancing the flow that transports colder air southwest towards the Sierra Nevada in the layer from 700-850 hPa. An upstream jet entrance region thermally direct secondary circulation exists as determined from Figure 8a and is consistent with this low-level cold advection (Figs. 8b and 9b) from Utah into Nevada. The thermal gradients intensify over the mountains while the effects of the warm advection and sinking in the mid-upper troposphere in the exit region overruns the cold air advection in the lower troposphere from the entrance region. This will cause increasing static stability above the mountains.

Figure 9 depicts the vertical differential lapse rate change for the 700-500 hPa layer over the six-hour time frame valid from October 8th, 23 UTC – October 9th, 05 UTC. The most important features on this chart are in Nevada and Eastern California. During the previous six hours, the lapse rate has significantly decreased signaling an increase in static stability near and just above 700 hPa as relative cooling occurs at that level in phase with the reduction in moisture content and jet descent and warming above that level. This is on the western side of the upper-level trough which produces downward, converging motion aloft and diverging low-level motion. This descending motion is reinforced by the progression and passage of the cold front, jet right exit region and their attendant subsiding airflow. Therefore, the decrease in moisture content is in the region where the wildfire event took place.

In Figure 10(a), the surface analysis chart indicates that over the central and western U.S., there is a weak, but extensive frontal system. The western segment of the frontal system extends into Northern California. Prior to the onset of the Tubbs Fire (2017), which occurred at approximately 04:45 UTC on October 9th, an inverted surface trough forms near this western segment of the frontal system. A strengthening surface high pressure system forms near the coastline of the north-

western U.S. The accompanying ridge's clockwise circulation propagates south-westward into Northern California.

At 00 UTC October 9th, the surface trough is well defined over Northern California, shown in Figure 10(b). Along the northern Pacific Coast and Rockies, the high-pressure center has moved onshore and intensified to 1024 hPa. With this intensifying south-westward-directed surface pressure gradient, winds increase over Northern California. Due to the circulation around the high, colder air is advected towards the central and western U.S. As this air progresses and flows over mountainous terrain at and below 700 hPa, the air parcels undergo adiabatic compression consistent with the air mass stabilization in Figure 9. This may result in buoyancy oscillations in the form of mountain waves that can transfer momentum from aloft as the airflow progresses towards the Californian coastline.

Figure 10(c) depicts the surface analysis chart for October 9th, 12 UTC. The surface high-pressure region in the Pacific northwest has further intensified to 1031 hPa. Resulting from this intensification, the south-westward-directed pressure gradient along Northern California increases. As shown in Northern California, the northeasterly wind weakens which would provide a less favorable environment for erratic wildfire behavior which follows the DW criteria. With time, the surface front has propagated into Southern California. From this frontal propagation, the area of cold air advection is no longer as intense in Northern California but would be more significant around the frontal boundary. This would result in less cold air advection in Northern California and more cold air advection in Southern California.

3.2 Observed Soundings

In Figure 11, three observed soundings at Reno, NV are displayed valid on October 8th at 12 UTC (a) and October 9th at 00 UTC (b), and 12 UTC (c). This sounding station was chosen due to

the location being far upstream of the wildfire location to determine the synoptic precursor environment. These soundings begin at 850 hPa, which is due to the station's elevation above sea-level. In panel (a), which is approximately 17 hours before the Tubbs Fire initiation, it can be observed that there are very low dew point temperatures, thus dry air at the 700 hPa level and extending up to approximately 600 hPa. At the surface, there is a weak north-northeasterly wind component which is confined to low levels. In time this will shift to a stronger northeasterly wind at the surface and extend deeper in the atmosphere.

In panel (b), on October 9th, 00 UTC, the transformation to a stronger northeasterly wind at the surface is evident. The northeasterly wind now extends to near 700 hPa. The stronger wind speeds are found near the surface and are decreasing with height. Furthermore, at approximately 700 hPa, the wind velocity is nearly zero which indicates a potential stationary mountain wave in association with a self-induced wave critical level. Also, at this 700 hPa layer, the decrease in dew point temperature intensifies at the same time cooling occurs of nearly 5°C. The dew point decreases from near -15°C to approximately -55°C at 600 hPa. A strong potential temperature inversion exists between the 700-500 hPa levels because the temperature of -5°C remains nearly constant with height until it decreases at 500 hPa. Note the increase in wind speed from 600 hPa through the tropopause (near 200 hPa). This indicates the arrival of the jet exit region as the jet streak passes near Reno, NV. This panel indicates the observed environment closest in time to the initiation of the Tubbs Fire (2017). It is consistent with NASA CALIPSO A-TRAIN and TOMS ozone data satellite data that signal tropopause folding in this region at this time (not shown).

In panel (c), on October 9th, 12 UTC the wind field transitions to an easterly flow at the surface and a southeasterly flow near 700 hPa. The dew point temperature increases, indicating moisture content is growing slightly, signaling that the most favorable environment for DW is diminishing.

There is still a strong presence of an inversion through the 700-500 hPa layer, but the wind velocities are increasing with height indicating that the self-induced wave critical layer may not be as strong or even present.

3.3 Simulated Synoptic Environment Conducive to the Tubbs Fire Formation

3.3.1 MSLP and Geopotential Height

Figure 12 depicts WRF-ARW simulated mean sea level pressure and 500 hPa geopotential height from domain D01. Panel (a) represents October 8th, 21 UTC and panel (g) October 9th, 03 UTC. Notice in panel (a) the structure of the MSLP field in Northern California, which is approximately seven hours and 45 minutes before the Tubbs Fire (2017) initiation. It is evident that there is a well-defined inverted surface trough (low pressure system) with a minimum pressure of 1010 hPa. In addition, there is a developing surface high-pressure center poleward of California in Oregon and Washington resulting in counterclockwise wind flow into Northern California. In Oregon and Washington, cold air is being transported from Canada towards California. Therefore, the relatively colder, denser air would provide enhanced downward motion on the leeside of the mountains. There is also a well-defined 500 hPa trough approaching northeastern California. This upper-level trough provides the confluent flow and cold advection foundation for low-level frontogenesis. With the geopotential thickness decreasing over eastern California and Nevada and wind backing with height, vertically varying geostrophic cold air advection sustains a strong vertical potential temperature gradient between warm air in the mid-upper troposphere and cold air in the lower troposphere.

With time, the 500 hPa height, in panels (b-c), continues to lower, progressing farther into Nevada. There is a progression poleward of the surface inverted trough which confines the surface low to Northern California. In panel (d), the geopotential height in the trough begins to rise over

Nevada. This is due to this trough exiting California and progressing farther eastward into the contiguous U.S. In panels (e) and (f), the inverted surface trough is becoming better organized and the isobaric gradient changes indicating a stronger surface wind field. In panel (g), the once tight gradient of geopotential height in the vicinity of Northern California has now weakened, and the tightest gradient has now reformed in Southern Nevada. With this quasi-geostrophic height change, the frontogenetical structure would become less significant in Northern California. However, behind the cold front, backing wind with height continues to bring geostrophic cold air advection in the lower troposphere into Northern California, indicating a region of air undergoing downward motion.

3.3.2 Upstream Sounding Validation

Soundings were extracted from the WRF-ARW D02 simulation at Reno, NV. Figure 13(a) depicts the sounding for October 8th, 12 UTC. At the surface, there are weak northwesterly winds. However, the northwesterly winds do not extend deep into the atmosphere before turning westerly. Furthermore, the boundary layer exhibits a slight temperature inversion (in black) right above 850 hPa. There is a significant drop in moisture content beginning around 750hPa which extends to 600 hPa. This indicates that the lower to mid-troposphere is drying. However, approximately 17 hours before the wildfire event, the dew point temperature is relatively close to the ambient temperature at the surface. These RH components will change and become indicative of an environment favorable for DW.

In Figure 13(b), on October 9th, 00 UTC, the surface wind direction has changed to northeasterly. The maximum northeasterly wind is found near the surface before decreasing with height. At approximately 700 hPa, the wind is calm. With 0 ms^{-1} winds, critical level formation conducive to mountain waves is likely. This includes a wind reversal with height above that level.

In addition, between approximately 600 hPa and 500 hPa, there is a temperature inversion. With this inversion, significant gravity wave energy will be reflected downwards towards the surface instead of propagating into the upper troposphere consistent with the Wave Resonance Theory of downslope windstorms referenced earlier (e.g., Clark and Peltier, 1983 & Smith, 1985). Additionally at this level, there is an enhancement of dry air compared to panel (a). With this mid-tropospheric dry air coupled with the capping of the boundary layer, the air parcels accompanying the gravity wave reflected energy will be transported to the surface with virtually no moisture. Thus, these conditions indicate that five hours prior to the wildfire initiation, the environment became favorable for the erratic fire behavior.

In Figure 13(c), approximately seven hours past the initiation of the wildfire, a transition from northeasterly winds to southeasterly winds took place far upstream at Reno, NV. The overall wind velocity increased in the lower troposphere when this wind direction transition took place. Also, a more noticeable temperature inversion in the 725-600 hPa layer is in place with the top of the inversion still being the critical level with zero wind. This warming of the lower troposphere maintains adequate conditions for the transfer of upper-level energy back towards the surface. The magnitude of the dew point temperature has increased from near -50°C to -40°C indicating that the upper-level support of surface severe downslope winds is diminishing.

3.3.3 Jet Stream Simulation Analysis

In Figure 14(a-g), the simulated wind velocity at 300 hPa is presented in sequence from October 8th, 21 UTC through October 9th, 03 UTC. In panel (a), there is a jet streak bifurcated by the massive upper-level trough. Within this streak, there is a core wind speed of 65 ms^{-1}. Concurrently, the entire jet stream is propagating further equatorwards towards Nevada. The highest velocity of the jet will stay well to the east of Northern California. In panel (b) and (c),

425 there is little movement in the position of the jet. Even though there is little movement in the west
426 to east direction, it is evident that the jet stream is weakening. Another notable feature in panel (c)
427 is that the jet streak remains intact. In panel (d) and (e) this jet streak begins propagating further
428 equatorward, but the jet streak begins weakening in the trough. From this positioning of the jet
429 streak, the jet streak will likely have a secondary circulation beneath the 300 hPa level in the
430 entrance and exit regions in proximity to the Sierra Nevada as depicted in Figure 6(b). The jet
431 streak entrance region reaches the Reno, NV currently. From this exit region's thermally indirect
432 transverse ageostrophic secondary circulation one would expect sinking motion on the right side,
433 near Northern California as shown in Figure 8. This is consistent with the convergence observed
434 in Figure 7(b). From this sinking motion air parcels would undergo adiabatic compression which
435 would inevitably help warm the air column in the mid-troposphere. This warming of the air column
436 then produces the temperature inversion within the mid-troposphere when coupled with the low-
437 level return branch of cold air advection under the entrance region of the jet. Specifically, in panels
438 (f) and (g), the jet stream begins exhibiting a positively tilted structure which indicates the shift in
439 the exit region towards Northern California.

440 *3.3.4 Vertically Differential Temperature Advection*

441 Figure 15 depicts the simulated difference in horizontal temperature advection through the
442 500-700 hPa layer in time increments of one hour from October 8th, 21 UTC to October 9th, 03
443 UTC. In panel (a), the vertical difference in temperature advection is consistent with significant
444 cold temperature advection in the lower troposphere across Northern California. From this, one
445 infers an implied difference in layer thermal changes, i.e., sinking air above low-level cold air
446 advection, thus the cold air advection is focused within Northern California. To the northeast in
447 Nevada and Oregon, the upper-level sinking, and warm air advection is dominant. In panels (b)

and (c), the temperature advection values begin to increase in magnitude, whether that be positive or negative. This increase in magnitude of advection is consistent with the strengthening of the upper-level trough. In addition, the cold air advection begins moving further equatorward. In panel (d), the cold air advection within the 500-700 hPa layers propagates over the Sierra Nevada Mountain Range, while the warm air advection remains in the far northern part of California and well into Nevada above 500 hPa. In panel (e), the magnitude of cold air advection and warm air advection continue to increase as the upper-level trough continues to move equatorward into Central Nevada and Central California. However, the areas where cold air advection increases the most indicates the periphery of the frontal system. Finally, in panels (f) and (g), the most significant feature is the intense upper-level warm air advection over the Sierra Nevada Mountains. Due in part to this warm air advection, the static stability on the windward slopes of the Sierra Nevada Mountains increase. From this static stability parameter, one can infer that there will be advection of potentially warm air on the right side of the jet streak exit region from the north and northwest, which when it comes into proximity of the cold air advection beneath it, acts to stabilize the boundary layer structure confining the turbulent mixing processes to very low levels. This differential advection of air masses help describe the capping of the boundary layer near 700 hPa within which the critical layer of the mountain wave resides.

3.3.5 Analysis of Simulated Cross Section

For the first vertical cross-sectional analysis, a cross section from D01 will be utilized, as shown in Figure 16. This cross section covers [125.06°W, 37.88°N] x [115.35°W, 40.63°N] and was used to determine the effects of the jet from far upstream along with showing the vertical structure of the mountains.

(a) Total Wind, Wind Vectors, and Potential temperature (Theta)

Figure 17 depicts a vertical cross section of potential temperature, wind vectors and wind velocity from D01. The orange star indicates the approximate location of the Tubbs Fire (2017). In panel (a), on October 8th, 21 UTC, the upper-level jet intersects this cross section and has a core value of greater than 40 ms^{-1}. This core descends from ~200-400 hPa. Shown within panel (a), there is a transitional area in the mid-troposphere where the wind reverses direction. In the upper atmosphere, the wind vector is shown to be directed from approximately left to right, while in the lower troposphere, it is directed from right to left. As time progresses towards the initiation of the wildfire, noticeable differences in the lower and upper troposphere take place. Shown in panel (b), the upper tropospheric wind velocity decreases with time. This decrease in wind velocity indicates that the jet is propagating outside of the cross section. Also, notice the relatively weak wind velocity near the location where the Tubbs Fire will form. Wind velocities vary between 4-8 ms^{-1} in this location. In panel (c), the upper-level jet continues to recede and decrease in wind velocity over the area. In addition, between the 500-700 hPa levels, the isentropes begin to increase which signifies a tightening vertical potential temperature gradient. Notice the vertical tilt of the isentropic surfaces near the Sierra Nevada Mountains. Because of this tilt, and the critical level forming, downward motion ensues and envelops the leeside of the mountains. In panel (d), the first severe downslope wind event begins forming on the leeside of the Sierra Nevada Mountains. However, this event was significantly far from the Tubbs Fire location, therefore not directly impacting the Tubbs Fire. The second severe downslope wind event near the orange star location forms and begins to become apparent. Currently, on October 9th, 00 UTC, the wind velocity begins to increase from 4 to nearly 8 ms^{-1}. In panel (e), the severe downslope wind event at the Tubbs Fire location steadily increases in intensity.

From the low-level isentropic analysis, there are two distinct hydraulic jumps. The first being on the lee slopes of the Sierra Nevada Mountains and the second being directly above the Tubbs Fire location. Similarly, in panel (f), both severe-downslope wind events intensify and the wind velocities at the surface continue to increase. Note the winds aloft in the 350-500 hPa layer peak at 16 ms^{-1}. Based on this low wind velocity, the jet is no longer in the region of either downslope wind event. Finally, in panel (g), which is on October 9th, 03 UTC, the hydraulic jumps become well defined, and the severe downslope windstorms are reaching their maximum intensity. Looking closely at the Tubbs Fire location, there is a localized area directly above the surface where wind velocities are exceeding 20 ms^{-1}. However, aloft, there is a discontinuously stratified atmosphere where the upper-level momentum does not reach the surface.

(b) Vertical Wind Circulation, Wind Vectors, and Potential temperature (Theta)

Figure 18 depicts the vertical wind component in color instead of showing total speed in color. Also, in the figure, the horizontal wind vectors and theta contours remain the same. For the initial time of October 8th, 21 UTC, it is notable to see that the Sierra Nevada Mountain Range leeside slope is experiencing upward motion with a magnitude of 0.1 ms^{-1}. Similarly, the leeside slope of the Northern Coastal Mountain Range, where the Tubbs Fire will be located, is experiencing upward motion, as well. In the beginning, the isentropes are shown with few perturbations through the boundary layer and above. In panel (b), the Northern Coastal Mountain Range has upward motion on the lee slope. However, this upward motion intensifies from the surface through the mid-troposphere. In addition, this continued upward motion begins affecting the theta surfaces. From panels (b) and (c), the developing hydraulic jump takes place over the Northern Coastal Mountain Range. With this hydraulic jump, momentum is again lifted from the surface upwards. As this hydraulic jump develops, the downward motion begins to increase over the Northern

Coastal Mountain Range. However, a similar downslope wind event over the Sierra Nevada Mountains has yet to intensify. In panel (d), the theta contours continue to organize a well-defined hydraulic jump on the leeside of the Sierra Nevada Mountains. From this jump, a well-mixed "dead" region of uniform density occurs between the theta contours consistent with the Hydraulic Theory of Downslope Windstorms (Smith, 1985). This is deduced by the spacing of the contours around the hydraulic jump, meaning this well-mixed air achieves constant density through turbulent mixing. In panel (e), the downward motion begins extending through a deep layer near 750 hPa with an approximate velocity of -0.3 ms^{-1}. Another notable feature is an upward propagating mountain wave, which develops on the windward side of the Northern Coastal Mountain Range and progresses with considerable amplitude all the way through 300 hPa. In panel (f), the downward velocity exceeds -0.4 ms^{-1}. Above the planetary boundary layer, located directly above the Northern Coastal Mountain Range, significant upward motion takes place, followed by significant downward motion from 450-200 hPa. Also, the mountain wave continues to amplify likely due to the wave resonance within the discontinuously stratified atmosphere. This is inferred from the steepening of the isentropic surfaces.

4. Simulated Mesoscale Environment Instrumental in Erratic Fire Behavior

In this section, results will be presented for D03 of the numerical simulation. Depicted are four sets of figures. The first of which is simulated soundings taken at the Tubbs Fire initiation location. Second, a cross section showing total wind, wind vectors and potential temperature. The results will show the localized mountain structure of the Northern Coastal Mountain Range along with providing a way to describe the mesoscale dynamics of the severe-downslope winds. In Figure 19, the specific cross section is shown. Also, the star indicates the location of the Tubbs Fire. The specific latitude and longitude coordinates for this cross section is [123.20°W, 38.22°N] x

539 [121.93°W, 39.07°N]. Third, a Hovmöller diagram taken from the cross section shows bore
540 genesis. Fourth, a cross section showing vertical wind, wind vectors, and potential temperature is
541 presented.

542 *4.4.1 WRF-ARW Simulated Soundings for Self-Induced Wave Critical Level Analysis*

543 In Figure 20, soundings were taken from the numerical simulation using the latitude and
544 longitudes of the approximate fire initialization location over the Northern Coastal Mountain
545 Range. In panel (a) taken at 00 UTC on October 9th, the surface winds have increased over the
546 previous hour directed from the northeast to the southwest. While there is significant momentum
547 at the surface, between the layers of 850 and 700 hPa there is a drastic decrease in wind velocity
548 compared to the surface. In panel (b) taken at 01 UTC on October 9th, the velocity at the surface
549 has increased to a very large magnitude sustained at > 25 kt from the same direction while it has
550 decreased to near zero kt in the 850 to 700 hPa layer. This region of near zero wind above the
551 surface is significant as it indicates a reduction in velocity consistent with the development of a
552 self-induced wave critical level during non-linear mountain wave amplification. This can be
553 attributed to the increasing wave-induced deceleration and the development of a well-mixed
554 "dead" region where density is approximately constant resulting from the maximization of
555 turbulent mixing. This is representative of a self-induced wave critical level where wave energy
556 is amplified by over-reflection when the wave causes a change (reversal) in the along-stream
557 pressure gradient force acting to slow the flow aloft (e.g., Peltier and Clark, 1983). This allows
558 for the reversal of the wind direction, rapid deceleration, and a developing stationary mountain
559 wave to exist where the phase velocity is approximately equal to the base state wind.
560 Nonlinearity in this process becomes dominant, which would inherently reduce the flow even
561 further. Momentum is then transported to the surface by the breaking wave.

562 *4.4.2 Total Wind, Wind Vectors, and Potential Temperature (Theta)*

563 In Figure 21, a cross section is depicted analogous to the one in D01, but for D03. From panel
564 (a), the Northern Coastal Mountain Range is seen. The orange star within the figure remains
565 representative of the Tubbs Fire location. On the leeside of the Tubbs Fire location, slow wind
566 velocities of ~4 ms^{-1} are present, valid for October 8th, 21 UTC. On the windward side of the Tubbs
567 Fire location, compressed isentropic surfaces are shown near the mountain tops. In addition, the
568 curvature of the isentropic surface in the region of 900-700 hPa is indicative of gravity waves
569 resulting from the resonance within the vertical profile of stability over the Northern Coastal
570 Mountain Range. Also, on the windward side of the Tubbs Fire location, from 850-300 hPa, there
571 is a well-defined upward propagating mountain wave. At 21 UTC, there is already a noticeable
572 compression of the isentropic surface accompanying wave resonance on the leeside of the Northern
573 Coastal Mountain Range. Although there lacks a significant downslope wind, a well-defined
574 hydraulic jump has already formed. In addition, the wind vectors indicate that there is a region
575 aloft of a wind reversal near the 700 hPa region. In panels (b) and (c), a steepening of the isentropic
576 surface on the leeside of the mountains is present. With this steepening, the air parcels passing
577 over the Northern Coastal Mountain Range descend dry adiabatically, which aids in increasing
578 surface wind velocity as they descend. Accompanying this increase in wind velocity at the surface,
579 the severe downslope winds begin to organize with time. In panel (d), valid on October 9th, 00
580 UTC, the surface wind velocities of ~8 ms^{-1}, begin to merge with the upstream wind flow extending
581 into the Northern Coastal Mountain Range. Notice on the leeward side of the Tubbs Fire location,
582 the isentropic gradient is increasing at the surface which foreshadows the coupling of the upstream
583 background flow, seen in panel (e). With this coupling of the background flow and the well-defined
584 compression of the isentropic surfaces, the severe-downslope wind event begins. In addition, there

585 is a second well-defined mountain wave forming through the depth of the troposphere resulting in
586 the downward flux in momentum on the leeside of the Northern Coastal Mountain Range. In panel
587 (f), the severe-downslope winds continue to intensify along with the steepening of the isentropic
588 surface. Furthermore, this sustained in-flow of upstream wind, progresses down the slopes and
589 into the Pacific as seen to the lower left of panel (f). This shows the intensity and longevity of the
590 changing background flow. In the last panel, (g), the intensifying downslope winds reach a
591 maximum of ~20 ms^{-1} (~45 mph) over the leeside of the Northern Coastal Mountain Range.

592 Within this high-drag, severe wind state, to the west of the Tubbs Fire, (near the beginning of
593 the cross section), a family of bore-like structures begin to form as shown in Figure 22(a). Bores
594 are low-level wave perturbations that propagate on the leeside stable layer after it has been
595 perturbed by the hydraulic jump-induced downslope flow (Karyampudi et al., 1995). With time,
596 as shown in panel (b), the bore intensifies, as seen by the undulation of the isentropic surface,
597 Furthermore, the wind vector orientation at the surface through 950 hPa shows a reversal with
598 winds propagating ~5 ms^{-1} towards the Tubbs Fire location. In Figure 20(c), the bore begins to
599 weaken and becomes stationary. However, due to this, a second hydraulic jump forms near the
600 coastline. With the presence of the second hydraulic jump, air mass displacement occurs forcing
601 upstream air masses to fill the void near the coastline. This amplifies the near surface wind
602 velocities prior to the coupling of background upstream air flow.

603 In time, shown in panel (d), the second hydraulic jump is enhanced and widens towards the
604 coastline and the bore-like presence begins again with support from the onshore winds defined by
605 the wind vectors at 950 hPa. Onshore flow into the bore motion and enhanced static stability help
606 sustain the bore through ducting as described in Karyampudi et al., 1995. In panel (e), due to the
607 coupling of upstream winds which intensified the severe-downslope winds at the Tubbs Fire

location, the onshore wind speed aloft is overtaken and a wind reversal showing offshore flow at the 950 hPa level occurs. Note the near surface wind direction off the Pacific coast. This wind direction still maintains offshore flow even without upper air support. Regarding the hydraulic jump near the coastline, it intensifies with the increase in surface wind speed and allows for more propagation and displacement of air parcels near the Tubbs Fire location. In panel (f) and (g), the bore propagation stops and diminishes while the second hydraulic jump reaches maximum intensification thus far.

4.4.3 Vertical Wind Circulation, Wind Vectors and Potential Temperature (Theta)

In Figure 23, vertical motion (fill) along with wind vectors and potential temperature (in contours) are presented from D03. Along the lee slope of the Northern Coastal Mountain Range, there is strong downward motion with a velocity of ~2 ms^{-1}, as shown in panel (a). Also, note the well-defined hydraulic jump on the lee slope of the Northern Coastal Mountain Range, as described in the previous section. Immediately downstream of the lee slope of the Northern Coastal Mountain Range, there is strong upward motion with velocities of ~1.2 ms^{-1}. This strong contrast of downward and upward motion is due to the hydraulic jump. Furthermore, note the bore making its way onshore. At the leading edge of the bore, convergence takes place near the surface which forces upward motion. This is indicative of the near 1 ms^{-1} vertical wind velocity along the bore edge. With time, as seen in panel (b), the bore rapidly intensifies and provides vertical motion that penetrates past 850 hPa. However, as seen in panel (c), the bore's strength is short lived as the second hydraulic jump forms and quickly expands the region of upward propagating wind further northeast towards the Tubbs Fire location. Concerning the downslope winds on the leeside of the Northern Coastal Mountain Range, the strength of the downward motion has remained intact through time with sustained winds of ~2 ms^{-1}, along with a long-lived hydraulic jump. Comparing

631 panel (d) and (e) reveals that the severe downslope winds continue to form with time. Furthermore,
632 the downward motion of the air extends from 850 to 750 hPa, signaling a rapid intensification of
633 downward momentum transport which provides an enhanced environment for the propagation of
634 the upstream flow in the direction of the coast. In panel (f) and (g) a discontinuously stratified
635 atmosphere begins to show as non-homogenous air flow occurs from 950 to near 500 hPa. Rapid
636 and drastic changes of upward and downward motion take place over very short distances
637 horizontally which can be explained by nonlinear mountain wave activity on the windward slopes
638 of the Northern Coastal Mountain Range. Finally, the well-defined severe-downslope winds near
639 the Tubbs Fire location accompany significant downward motion on the slopes along with a rapid
640 change to nearby upward motion which displaces the air parcel from 975 hPa to at least 850 hPa
641 vertically. Due to this circulation within the lower to mid-troposphere, the local environment
642 changed rapidly resulting in an atmosphere conducive to erratic wildfire behavior by virtue of
643 strengthening winds and drier air.

644 **5. Discussion and Conclusions**

645 On the day of the Tubbs Fire (2017), there was a well-developed trough aloft which advected
646 air with a large along-stream temperature gradient equatorward into Northern California, as shown
647 in Figure 6(a). The mean RH through the 700-500 hPa layer decreased below 70% towards the
648 West Coast of the U.S. As depicted in Figure 6(a), the 850 hPa height contours on October 9th, 03
649 UTC, show a strengthening of the southwest-northeast gradient over the Midwest U.S. Comparing
650 this feature to Figure 6(b) indicates that the upper-level trough contained cold air which was
651 advected equatorwards and westwards on its eastern side which lowers the geopotential heights
652 consistent with quasi-geostrophic theory. Accompanying this lowering of heights and its attendant
653 differential cold air advection, cold frontogenesis forms and extends towards the surface. The six-

654 hour lapse rate change in the 700-500 hPa layer becomes increasingly negative over Nevada into
655 Northern California indicating net cooling below and warming aloft. This is shown in Figure 9 and
656 evident from the subsequent 00 UTC observed and simulated soundings. The significance of the
657 negative change in lapse rates aloft over Nevada is that Nevada is upstream of the wildfire location
658 where static stability is increasing aloft not too far above the major mountain ranges. As the DW
659 occurs, which has a northeast wind direction, much drier air is transported from Nevada towards
660 Northern California. From Figure 10, the synoptic (MSLP) analysis shows the frontal boundary
661 extending over most of the western and central U.S. However, there will be very little, if any,
662 precipitation in the western U.S. due to the decreasing dew point temperatures caused by the deep
663 tropospheric horizontal advection and sinking of dry air. However, there will be vertically
664 differential thermal advection dominating the western U.S. due to the cold frontal system.
665 The WRF-ARW simulated MSLP and 500 hPa geopotential heights, shown in Figure 12,
666 indicate that the simulation proves to adequately replicate the observed upper-level and inverted
667 surface troughs shown in the observed charts. The progression of this frontal system, shown in
668 panels (a) through (g), indicates that the front will propagate eastward away from California as
669 time gets closer to the initiation of the wildfire event. From Figure 15, which shows the simulated
670 vertically differential temperature advection from the 700-500 hPa, there will be an abundance of
671 cold air advection from the northeast towards the California border with Nevada located under the
672 sinking of the jet exit region. This is shown in panels (a) through (g). Over the western flank of
673 the upper-level trough, enhanced negative vorticity advection in combination with this lower
674 tropospheric Laplacian of cold air advection signals downward quasi-geostrophic vertical motion.
675 From the analysis of the eastern side of the upper-level trough, the cold air advection is consistent
676 with the cold frontal passage at the surface, as seen again in Figure 10. The combination of Figures

677 12 and 15 provides ample evidence that WRF-ARW was able to adequately simulate the observed
678 synoptic and meso-α scale environment hours before the Tubbs Fire began.
679 To determine the vertical profile of the atmosphere, soundings were extracted from Reno, NV,
680 which is upstream of the wildfire location. This was done to determine the upstream air motion,
681 both at the surface and aloft, as shown in Figure 11. Considerable northeasterly winds extended
682 into California and Nevada. Comparing the observations to the simulated results, shown in Figure
683 13, WRF-ARW was able to adequately simulate the vertical profile of the atmosphere at Reno,
684 NV. Both simulated and observed soundings indicate a well-defined area in the troposphere,
685 between 700-500 hPa, where there is little moisture. This is seen in all three panels by the large
686 change in dew point temperatures. Another significant feature in both figures is an area aloft where
687 there is a wind reversal. Due to this wind reversal, there would be a layer where the wind velocity
688 is approximately zero. Within this layer, a critical level forms which indicates a favored location
689 for mountain wave formation and its attendant overturning surfaces of potential temperature. This
690 will cap the atmosphere and facilitate wave energy to be reflected towards the surface. This vertical
691 region of wind reversal is again seen in both observed and simulated figures. The physical
692 interpretation of why this level exists could be explained by the jet stream placement aloft in
693 conjunction with the cold frontal passage beneath.
694 The jet does play an important role in the upstream synoptic setup of the troposphere, as seen
695 in Figure 14. The evolution of the jet shows an important positively tilted trough as the jet
696 propagates further east, shown in panels (a) through (g), and a very persistent jet streak over
697 Nevada. However, the jet may be considered too far away from the wildfire location to have direct
698 impacts. To closely examine this, consider Figure 17. If the jet does have a direct impact, the
699 upper-level wind velocity would begin to show, in isotach color coding, the connection between

700 the upper troposphere and the lower troposphere. Instead, it is shown that the jet is lifting out of
701 Northeastern California and Northern Nevada. This is determined by the decrease in wind velocity
702 with time. In the last panel, (g), of Figure 17, when the severe-downslope wind event is already
703 taking place with considerable intensity, the upper-level jet has already decreased from 40 ms^{-1} to
704 ~12 ms^{-1}. This does suggest small direct impacts from the jet itself. In Figure 18, where only the
705 vertical wind component is plotted in color, various areas of upward and downward motion occur.
706 But, when considering the Tubbs wildfire location, indicated by the star, very strong upward
707 motion is detected aloft, rather than strong downward motion. This again indicates that the
708 strongest part of the jet is not conducive to connectivity from upper levels to lower levels. From
709 panel (g), an upward propagating mountain wave is shown with large amplitude. This upward
710 propagating mountain wave does make the connection from lower levels to upper levels of the
711 atmosphere, but the jet streak departed before this amplification of the mountain wave occurred.
712 This upward propagating mountain wave does help explain the intense vertical motion, but does
713 not show that the severe-downslope windstorm was caused by direct jet intervention.
714 Therefore, the jet stream influence paradigm, (Huang et al., 2009), would not apply directly to
715 the Tubbs Fire (2017). Since the jet streak placement is far away, on the order of 100s of
716 kilometers, the jet would not create a direct linkage between its upper-level exit region momentum
717 reaching the surface causing this specific severe-downslope wind event. This is not to say that the
718 jet has no impact on the erratic behavior of the Tubbs Fire. Mainly, the jet does set up the synoptic
719 environment for the frontal system to develop which has a major impact on the discontinuously
720 stratified atmosphere over the mountains. This discontinuity in the vertical does enable the self-
721 induced wave critical layer to form far upstream which reflects the gravity wave energy to the
722 surface. This reflection of energy traps the air mass in the lower troposphere, which forces the air

mass to diverge outward from the point of origin. In this case, causing the downslope wind event over the Sierra Nevada Mountain Range. Subsequently, this circulation does enable the compression and warming of the air mass adiabatically. In proximity to this circulation, the Tubbs Fire's severe-downslope wind event in the Northern Coastal Mountain Range increases, indicating the jet does have an indirect impact.

Regarding the results of the simulation of the mesoscale processes and mechanisms from D03, the mesoscale environment changes rapidly with time. Evidence suggests that two important areas of wave dynamics are present during the Tubbs Fire. First, the rapid setup and intensification of the hydraulic jump on the leeside of the Northern Coastal Mountain Range, seen in Figures 21 and 23. With this setup, the adiabatically compressed air from upstream flows rapidly down the lee slopes and is again rapidly displaced aloft due to the strong hydraulic jump. The adiabatically compressed air mass begins to mix vigorously within the 950-800 hPa region. With this turbulent air movement, a well-mixed "dead" region develops and becomes larger with time. In addition, the second hydraulic jump near the coastline provides another well-mixed "dead" region from 900-850 hPa. With this well-mixed region of near uniform density, the adiabatically compressed air parcels move underneath the "dead" region, which acts as a conduit for non-homogenous air densities. Second, a family of bores near the Pacific Ocean coastline propagates onshore towards the incident area, seen in Figure 22. With this bore propagation, it inherently intensifies the severe-downslope winds, whether at the location of the second hydraulic jump or towards the incident area of the Tubbs Fire. Therefore, initial analysis suggests that the bore structure plays an intricate role in the rapid intensification and development of the DW event by extending the strong momentum surge downstream.

745 In conclusion, the Tubbs Fire of 2017 impacted a vast portion of the Sonoma and Napa
746 Counties in Northern California. The simulations and supporting observations during the pre-DW
747 period help explain the synoptic-meso-α scale setup of the environment. With the strong
748 amplifying trough in the middle troposphere, accompanying the existing jet in the upper
749 troposphere, cold frontogenesis occurred over the Sierra Nevada. By the same token, the jet
750 streak's indirect exit region secondary circulation caused descending motion in conjunction with
751 and above the existing cold air advection resulting from the mid-upper tropospheric jet entrance
752 region low-level return branch circulation. From this southwestward-directed low-level jet under
753 the mid-upper tropospheric jet's entrance region, along with the downward momentum flux, these
754 adjustments enabled the organization of a deepening and ascending inversion over the Sierra
755 Nevada as well as a self-induced wave critical level between 700-500 hPa prior to DW formation.
756 As the organizing jet streak departed, the resulting discontinuously stratified atmosphere over the
757 Sierra Nevada Mountain Range along with the Northern Coastal Mountains allowed for a very
758 favorable environment conducive to wildfire formation. Without the influence of the jet resulting
759 in cold frontogenesis to the east of the Tubbs Fire location, the environment would likely not have
760 been primed for DW. Furthermore, upward propagating mountain waves are present coinciding
761 with the steepening of the isentropic surfaces consistent with the resonant interaction of nonlinear
762 gravity waves. Because of the environmental ingredients being in place, as discussed above, the
763 DW formed very quickly resulting in high momentum and dry air conducive to the spread of the
764 Tubbs Fire on the night of October 8th, 2017. These results help substantiate our hypothesis that
765 indirect effects of the polar jet streak, rather than direct effects, are critical to establishing the
766 environment conducive to the Tubbs Fire.
767

768 **Acknowledgments:** This research was funded by the National Science Foundation, Grants
769 1900621 and 2022961, and NCAR/CISL for support of computing time under Project No.
770 UNCT0005.

References

Chen, S.-H. and W.-Y. Sun, 2002: A one-dimensional time dependent cloud model. J. Meteor. Soc. Japan., 80(1), 99–118.

Clark, T. L., and W. R. Peltier, 1984: Critical level reflection and the resonant growth of nonlinear mountain waves. J. Atmos. Sci., 41, 3122–3134.

European Centre for Medium-Range Weather Forecasts. 2019, updated monthly. *ERA5 Reanalysis (0.25 Degree Latitude-Longitude Grid)*. Research Data Archive at the National Center for Atmospheric Research, Computational and Information Systems Laboratory.

Hatchett, B., Smith, C., Nauslar, N., & Kaplan, M, (2018): Brief Communication: Synoptic-scale differences between Sundowner and Santa Ana wind regimes in the Santa Ynez Mountains, California., Nat. Hazards Earth Syst. Sci., 18, 419-427

Huang, C., Y.-L. Lin, M. L. Kaplan, and J. Charney, 2009: Synoptic-scale and mesoscale environments conducive to forest fires during the October 2003 extreme fire event in Southern California. J. Appl. Meteor. And Climate, 48, 553-579.

Karim, M.S. S., Y.-L. Lin, and M. L. Kaplan, 2022: Formation Mechanisms of the Mesoscale Environment Conducive to a Downslope Windstorm over the Cuyamaca Mountains Associated with Santa Ana Wind during the Cedar Fire (2003). J. Appl. Meteor. & Clim.,

Karyampudi, V. M., Koch, S. E., Chen, C., Rottman, J. W., and M. L. Kaplan 1995: The Influence of the Rocky Mountains on the 13-14 April 1986 Severe Weather Outbreak. Part II: Evolution of a Prefrontal Bore and Its Role in Triggering a Squall Line Second Conf. on Fire and Forest Meteorology, Phoenix, AZ, Amer. Meteor. Soc., pp. 153–158

792 Krishnakumar P., Fox J., and Keller C. (2017, October 25). Here's where more than 7,500
793 buildings were destroyed and damaged in California's wine country fires. Retrieved from Los
794 Angeles Times
795 Lane, T. P., Doyle, J. D., Sharman, R. D., Shapiro, M. A., and Watson, C. D., 2009: Statistics and
796 Dynamics of Aircraft Encounters of Turbulence over Greenland. Mon. Wea. Rev., 137, 2867-
797 2702.
798 Lin, Y.-L., 2007: Mesoscale Dynamics, Cambridge University Press, 630pp
799 Martinez, J., Bergland, V., Franklin, M., Frits, M., Lohse, S., Roath, G., & Thompson, M. (2017,
800 October 8). CAL FIRE Investigation Report. St. Helena, CA, USA.
801 Mass, C. F., and D. Ovens, 2019: The northern California wildfires of October 8-9, 2017: the role
802 of a major downslope windstorm event. Bull. Amer. Met. Soc., 100, 235-256
803 Meier-Fleischer, K., Böttinger, M., & Haley, M. (2017). NCL User Guide. Boulder, CO, USA.
804 Mohler, M. (2018, June 8). CAL FIRE NEWS RELEASE. CAL FIRE Investigators Determine the
805 Cause of the Tubbs Fire. Retrieved from: California Department of Forestry and Fire
806 Protection.
807 NOAA. (2022, March 1). WPC Surface Analysis Archive. Retrieved from National Weather
808 Service Weather Prediction Center
809 NOAA SPC. (2022, Mar 01). Archive National Sector (s4) SPC Hourly Mesoscale Analysis
810 (HTML5 JavaScript Version). Retrieved from Storm Prediction Center NOAA / National
811 Weather Service
812 Oolman, L. (2022, Mar 01). Atmospheric Soundings. Retrieved from University of Wyoming
813 College of Engineering

814 PSU, 2022. Plymouth State Meteorology. Retrieved from Plymouth State Weather Center:
815 https://vortex.plymouth.edu/myowxp/upa/ctrmap-a.html
816 Shin, Y., J.-H. Kim*, H.-Y. Chun, W. Jang, and S.-W. Son, 2022: Classification of Synoptic
817 Patterns for Downslope Windstorms in Korea using the Self-Organizing Map. J. Geophys.
818 Res-Atmos., 127, e2021JD035867.
819 Skamarock, William C.; Klemp, Joseph B.; Dudhia, Jimy; Gill, David O.; Barker, Dale M.; Duda,
820 Michael G.; et al. (2019): A Description of the Advanced Research WRF Version 4. figshare.
821 Journal contribution. https://doi.org/10.6084/m9.figshare.7369994.v4
822 Smith, C., Hatchett, B., & Kaplan, M. (2018). A Surface Observation Based Climatology of
823 Diablo-Like Winds in California's Wine Country and Western Sierra Nevada. Fire, 1(2), 25.
824 MDPI AG.
825 Smith, R. (1985, December 01). On Severe Downslope Winds. *J. Atmos. Sci*. 42**,** 2597-2603
826 Uccellini, L. W., & Johnson, D. R. (1979, Jun 01). The Coupling of Upper and Lower Tropospheric
827 Jet Streaks and Implications for the Development of Severe Convective Storms. Monthly
828 Weather Review, 100, 682-703.
829 Wikipedia. (2021, April 10). Geography of California. Retrieved from Wikipedia: The Free
830 Encyclopedia.

831 **Table 1:** (Domain Specifics)

Domain	Grid points	Resolution (dx, dy)	Start	End
1	235 x 186	16km x 16km	October 8, 2017, 12 UTC	October 9, 2017, 12 UTC
2	505 x 369	4km x 4km	October 8, 2017, 15 UTC	October 9, 2017, 12 UTC
3	405 x 269	1km x 1km	October 8, 2017, 18 UTC	October 9, 2017, 12 UTC

832 **Table 1** WPS nested domain configuration

833 **Figure 1** (Terrain Map)

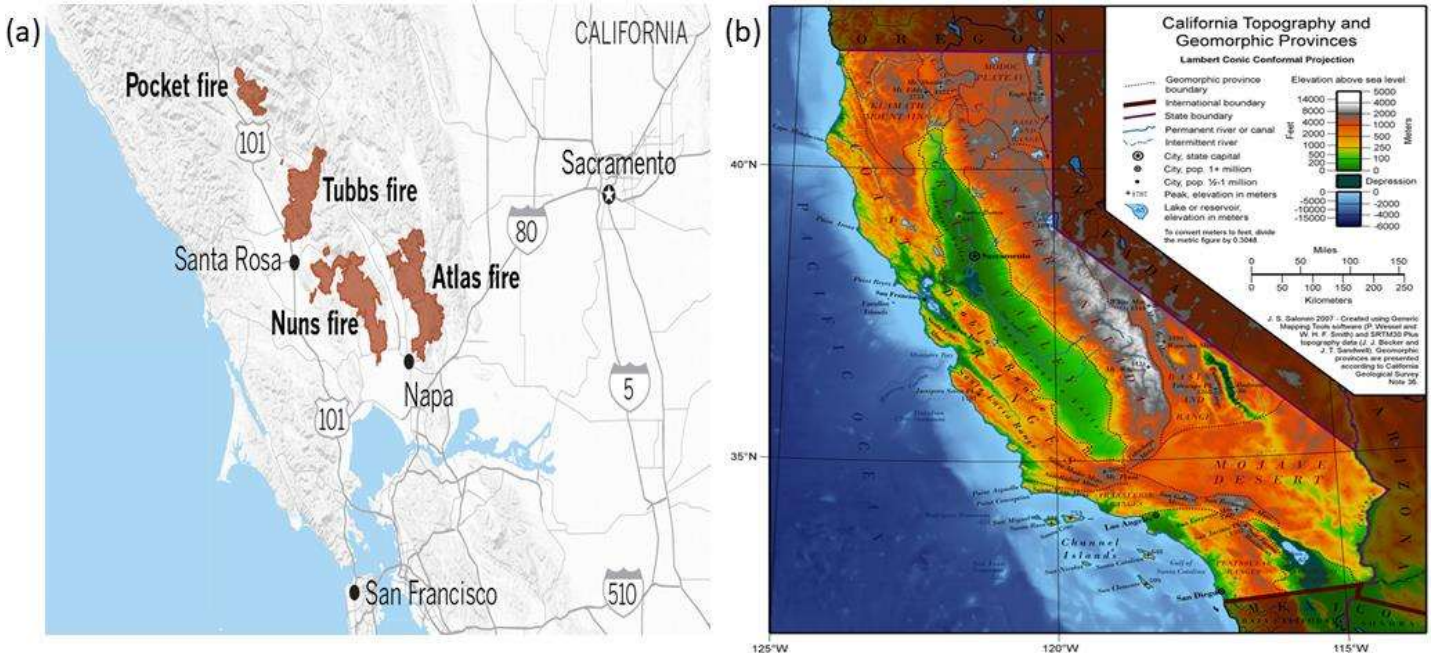

834

835 **Figure 1** a) Local map showing the Tubbs and other synchronous fires in the San Francisco Bay
836 region (Krishnakumar et al., 2017) and b) a terrain map of California (Wikipedia, 2021).

837 **Figure 2** (RAWS Network)

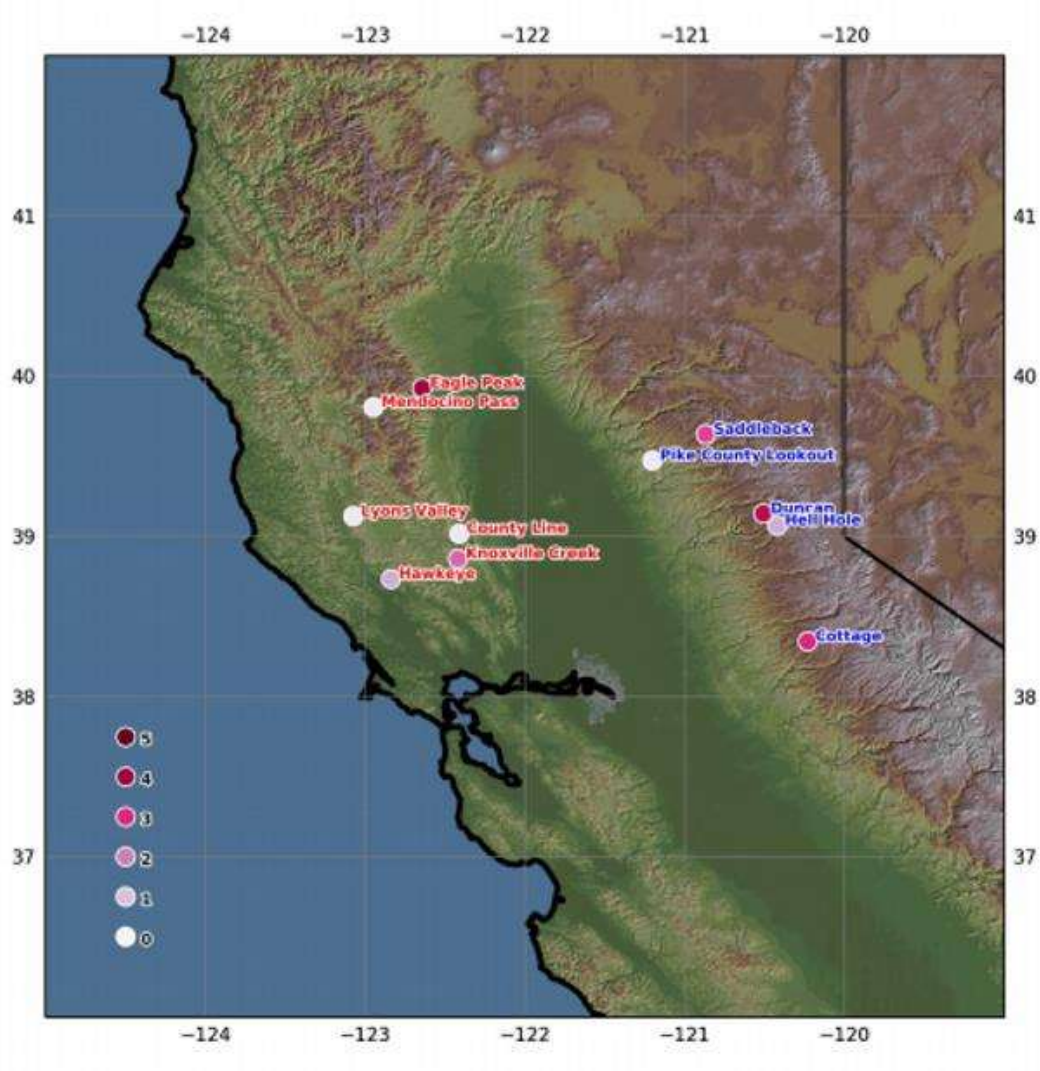

838

839 **Figure 2** RAWS network for climatological data (Smith et al., 2018)

840 **Figure 3** (Diablo Wind Events)

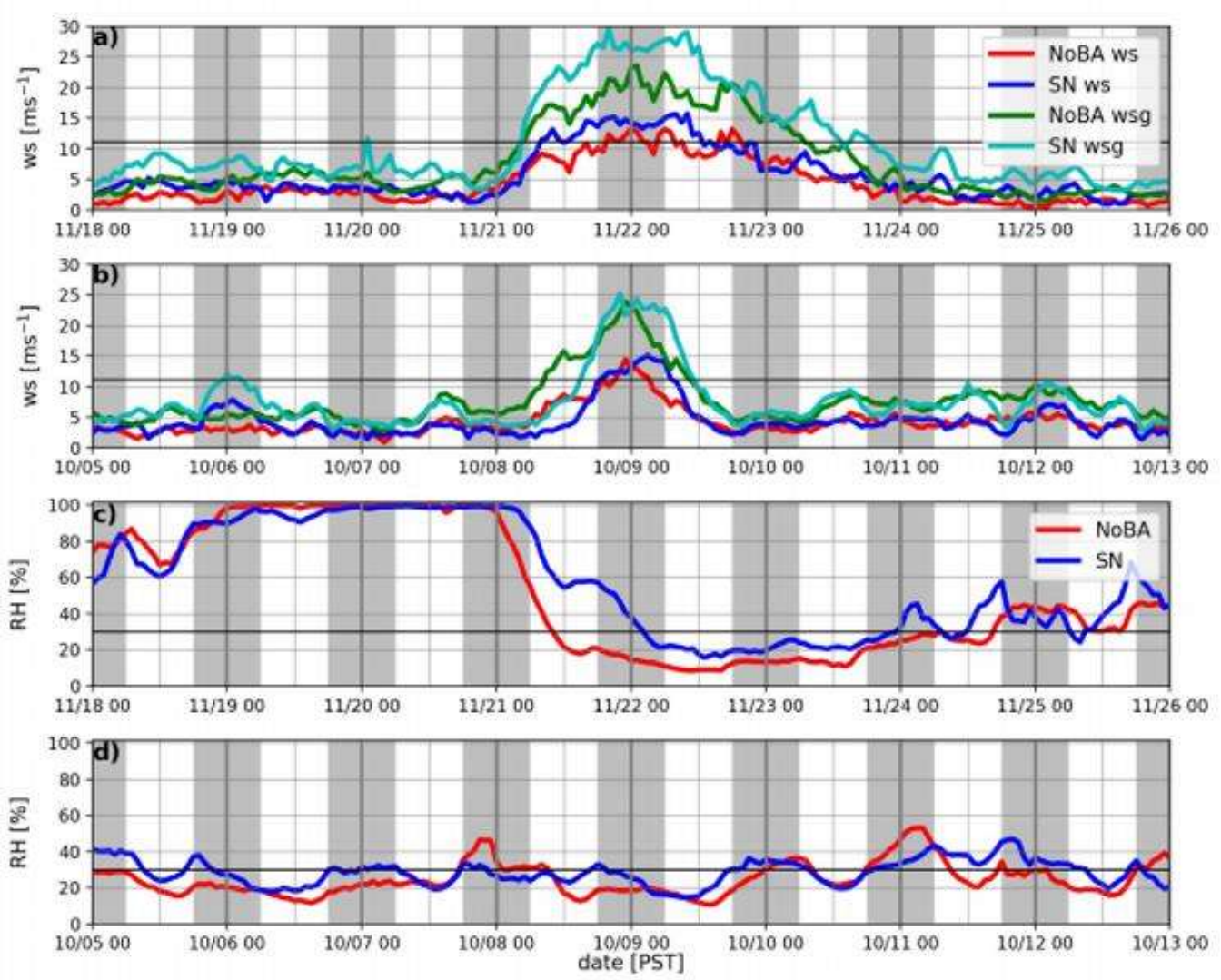

841

842 **Figure 3** November 2013 and October 2017 Diablo Wind Events (Smith et al., 2018). Color
843 coding differentiates the two events with blue = Sierra Nevada and red = North Bay RAWS and
844 green indicating differences in max gusts.

845

846 **Figure 4** (HLKC Theory)

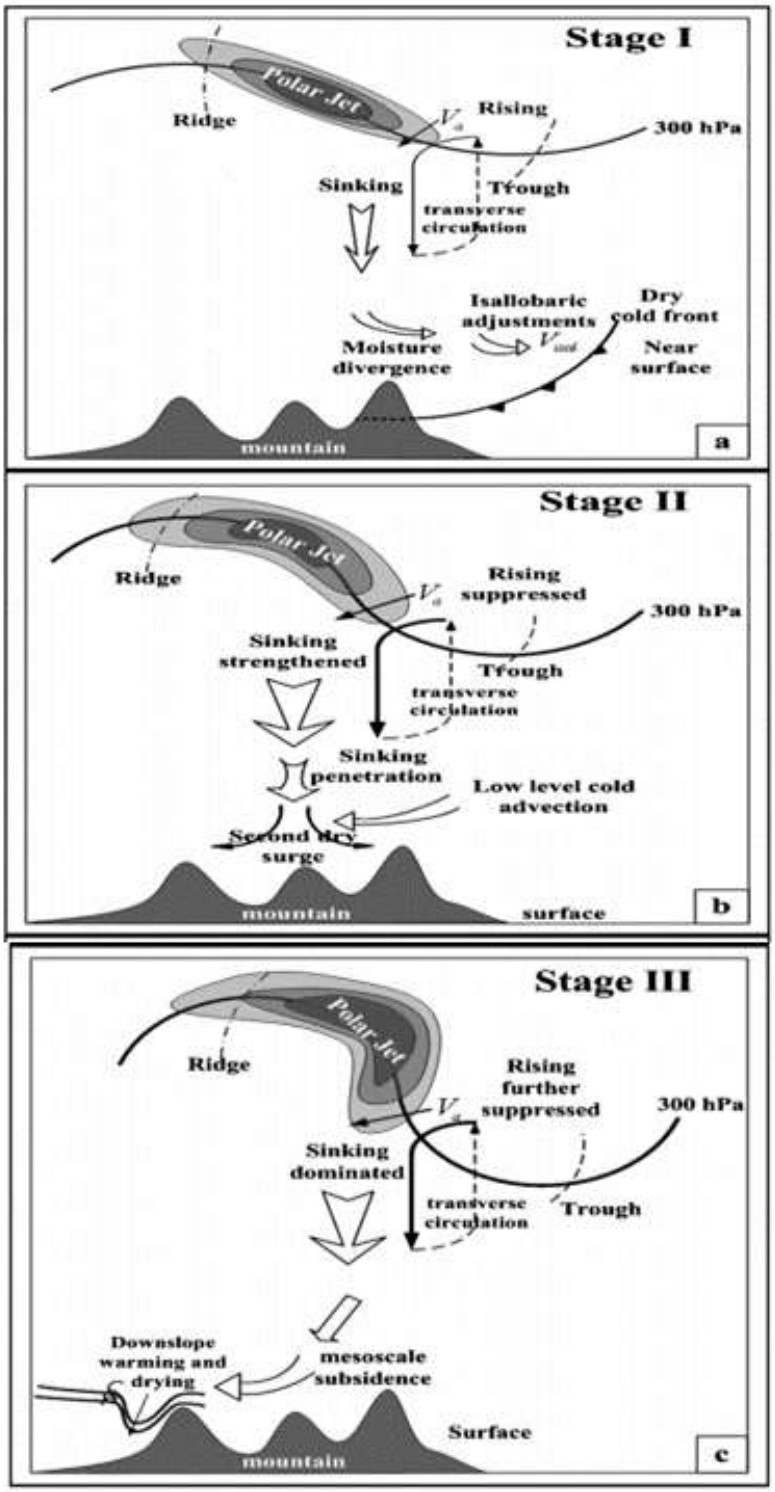

847

848 **Figure 4** The HLKC conceptual model proposed in HLKC theory (Huang et al., 2009) of polar
849 jet influence on severe-downslope wind events.

850 **Figure 5** (Domain Configuration)

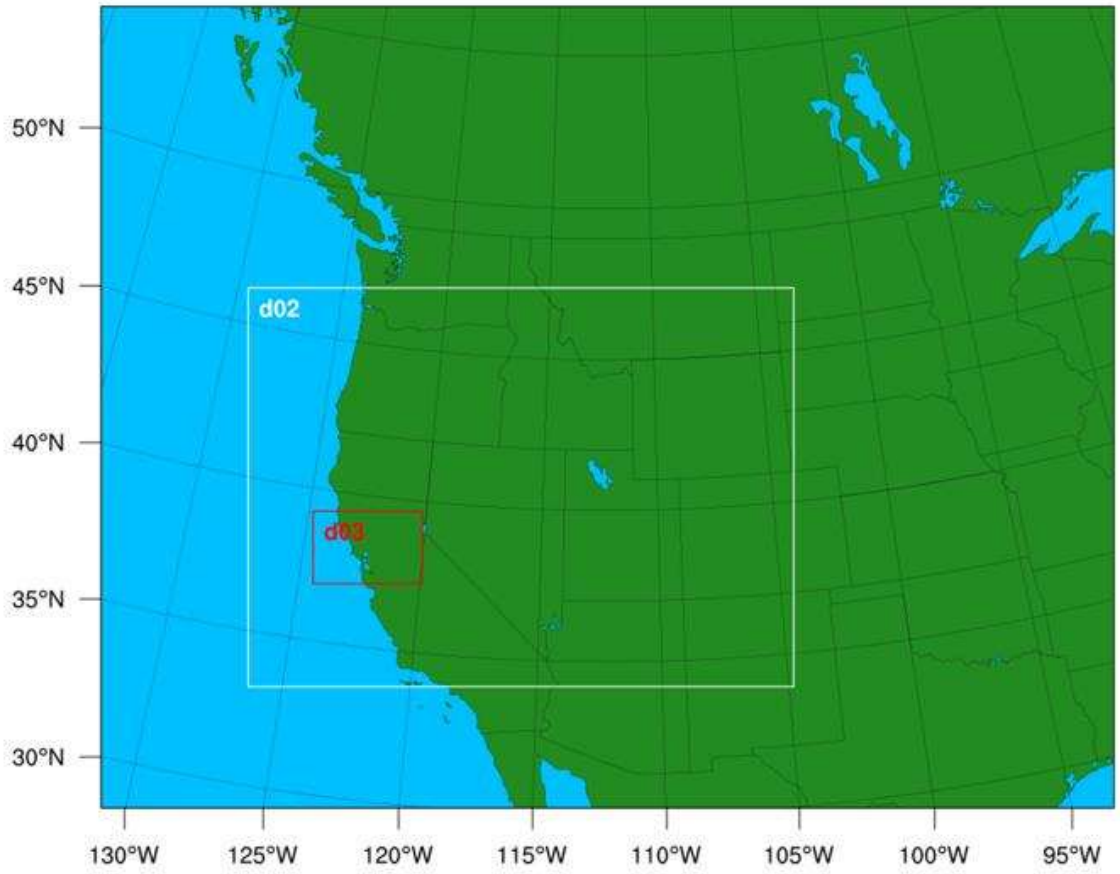

851

852 **Figure 5** WPS domain configuration for running WRF-ARW version 4.0.

853

Figure 6 (700 hPa and 850 hPa Analysis)

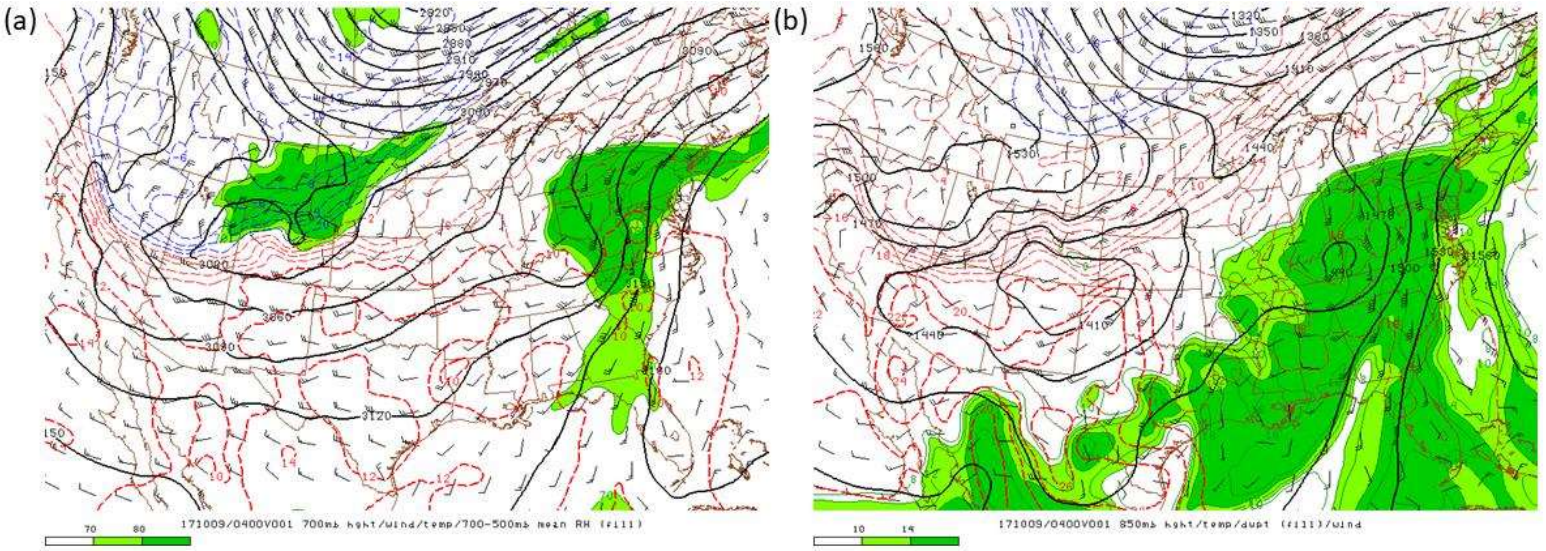

Figure 6 Observed 700 hPa height (solid in m), wind barbs (ms^{-1}), temperature (dashed in °C), and 700-500 hPa mean relative humidity (fill in %) and b) 850 hPa height (solid in m), wind barbs (ms^{-1}), temperature (dashed in °C), and dew point (fill in °C) valid October 9, 2017, at 03 UTC (NOAA SPC, 2022).

Figure 7 (300 hPa Wind Velocity and Convergence Analysis)

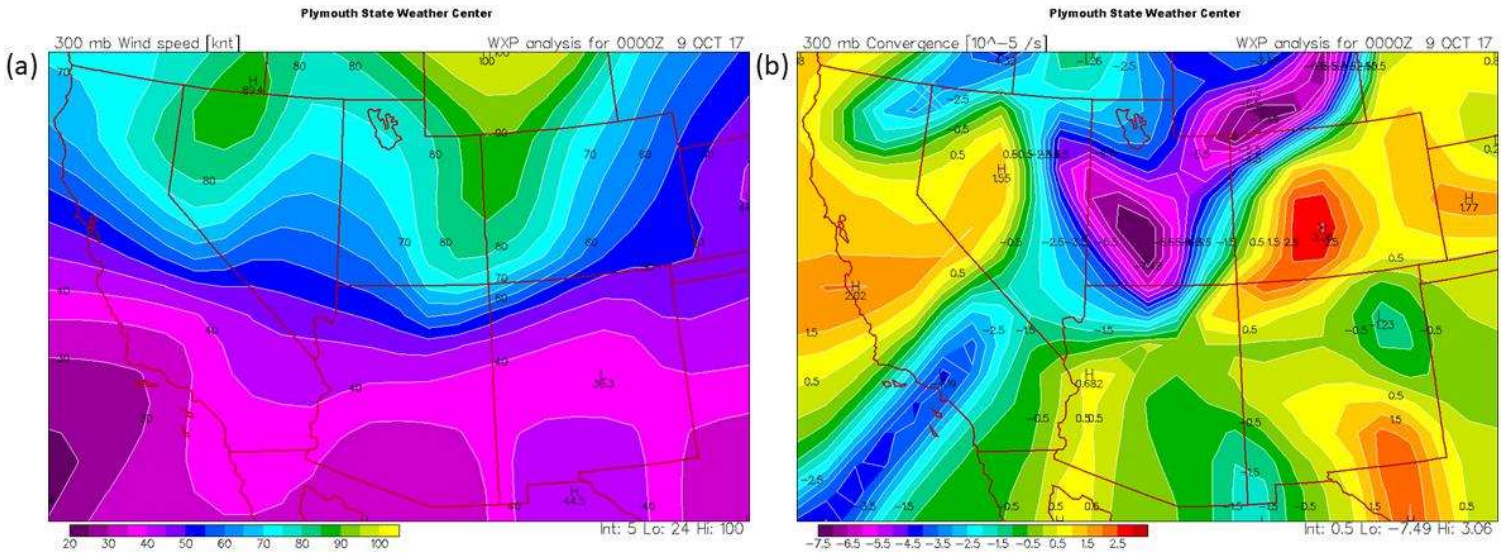

Figure 7 a) Observed 300 hPa wind velocity (fill in kt) and b) velocity convergence (warm colors – positive values, cold colors – negative values in 10^{-5} s^{-1}) valid October 9th at 00 UTC (PSU, 2022).

865 **Figure 8** (300 hPa Isotachs, Heights, Ageostrophic Winds and 700-500 hPa Layer Average

866 Omega)

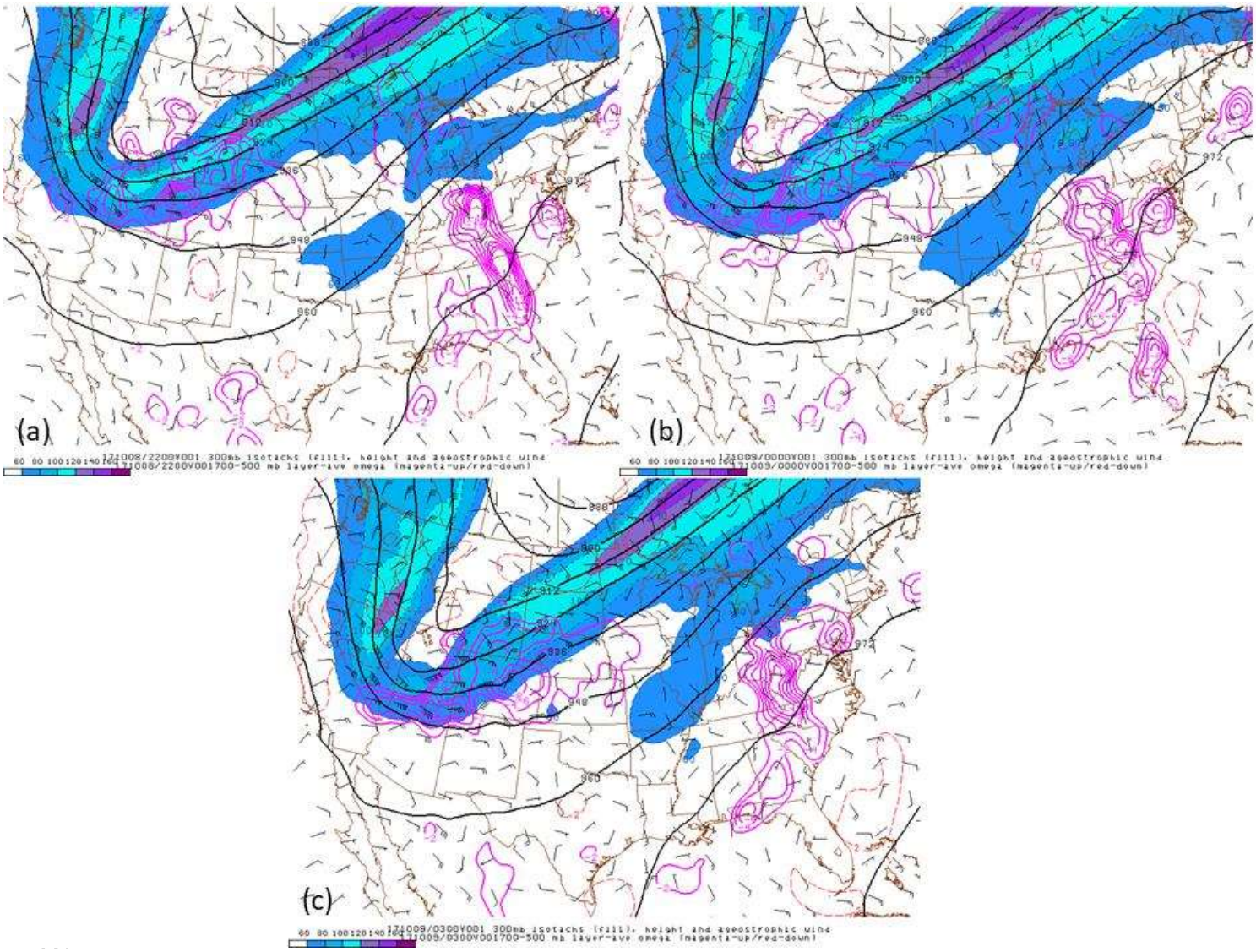

868 **Figure 8** Observed 300hPa isotachs (fill), heights and ageostrophic winds as well as the 700-500
869 hPa layer average of omega valid October 8, 2017, at 22 UTC (a), October 9th, 00 UTC (b) and
870 October 9th, 03 UTC (c) (NOAA SPC, 2022).

871

872 **Figure 9** (Vert. Diff. Lapse Rate)

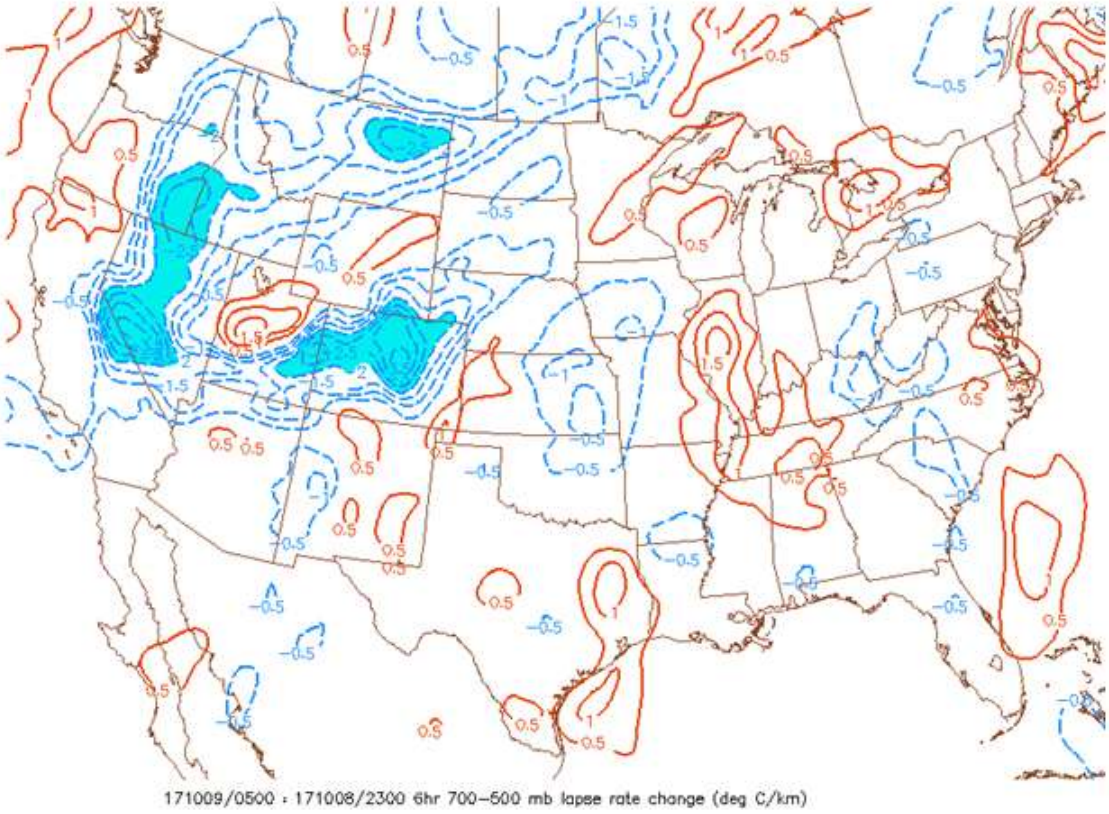

873

874 **Figure 9** Observed six-hour vertical differential lapse rate change from 700-500 hPa (negative
875 blue (stabilization) dashed in °C km^{-1}) valid from October 8th, 23 UTC – October 9th, 05 UTC
876 (NOAA SPC, 2022).

877 **Figure 10** (Surface Analysis Charts)

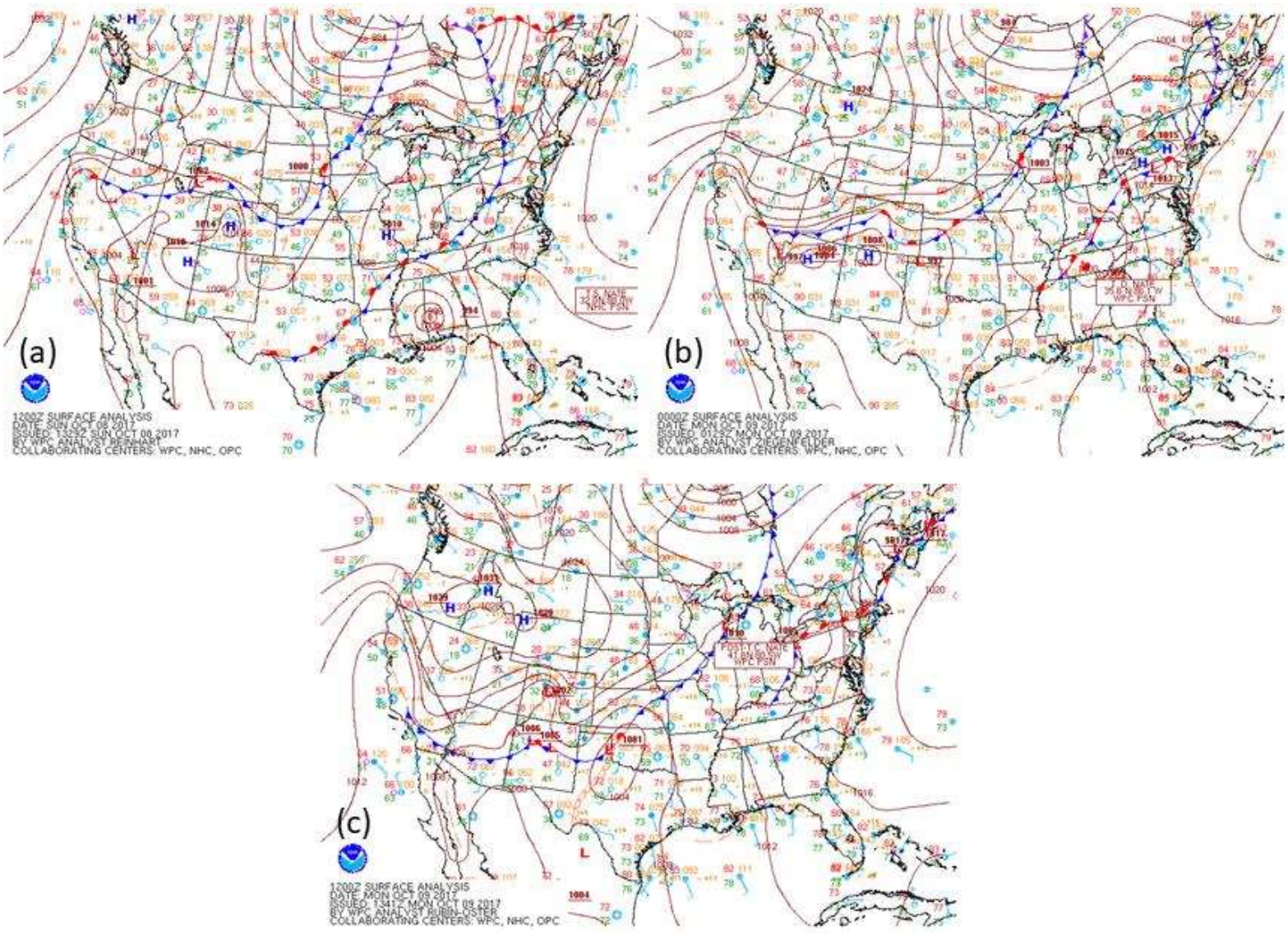

879 **Figure 10** Observed surface analysis chart for a) October 8th, 12 UTC, b) October 9th, 00 UTC
880 and c) October 9th, 12 UTC (NOAA, 2022).

881 **Figure 11** (Observed Soundings)

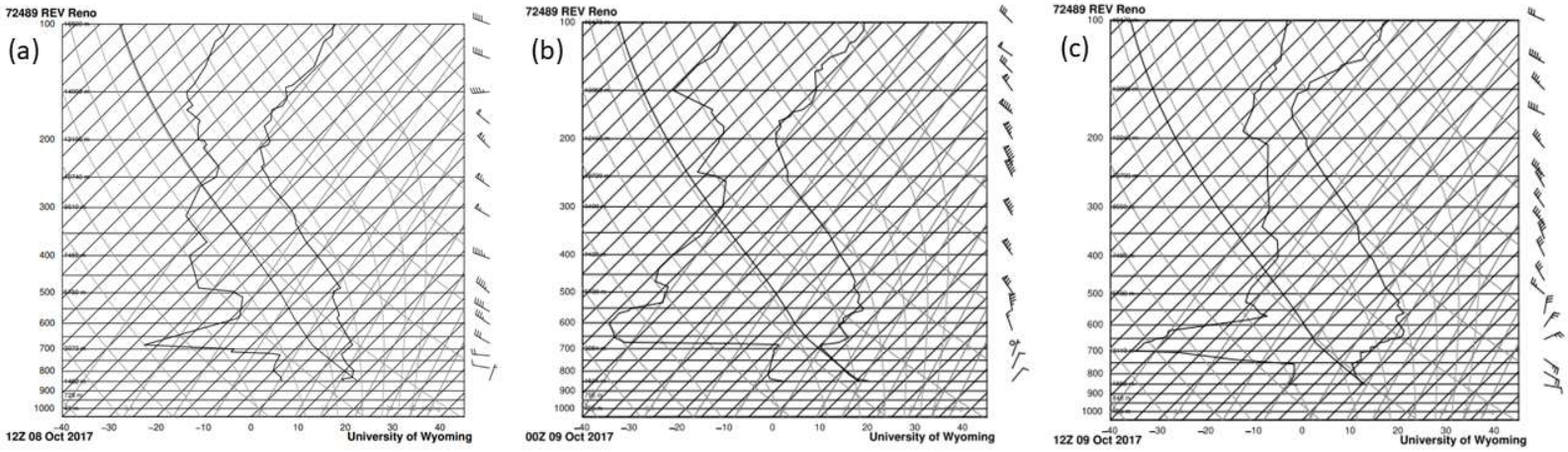

883 **Figure 11** Observed soundings from Reno, Nevada valid at October 8th at 12 UTC, October 9th at
884 00 UTC and October 9th at 12 UTC (Oolman, 2022).

885 **Figure 12** (SLP and 500 hPa Geop. Heights)

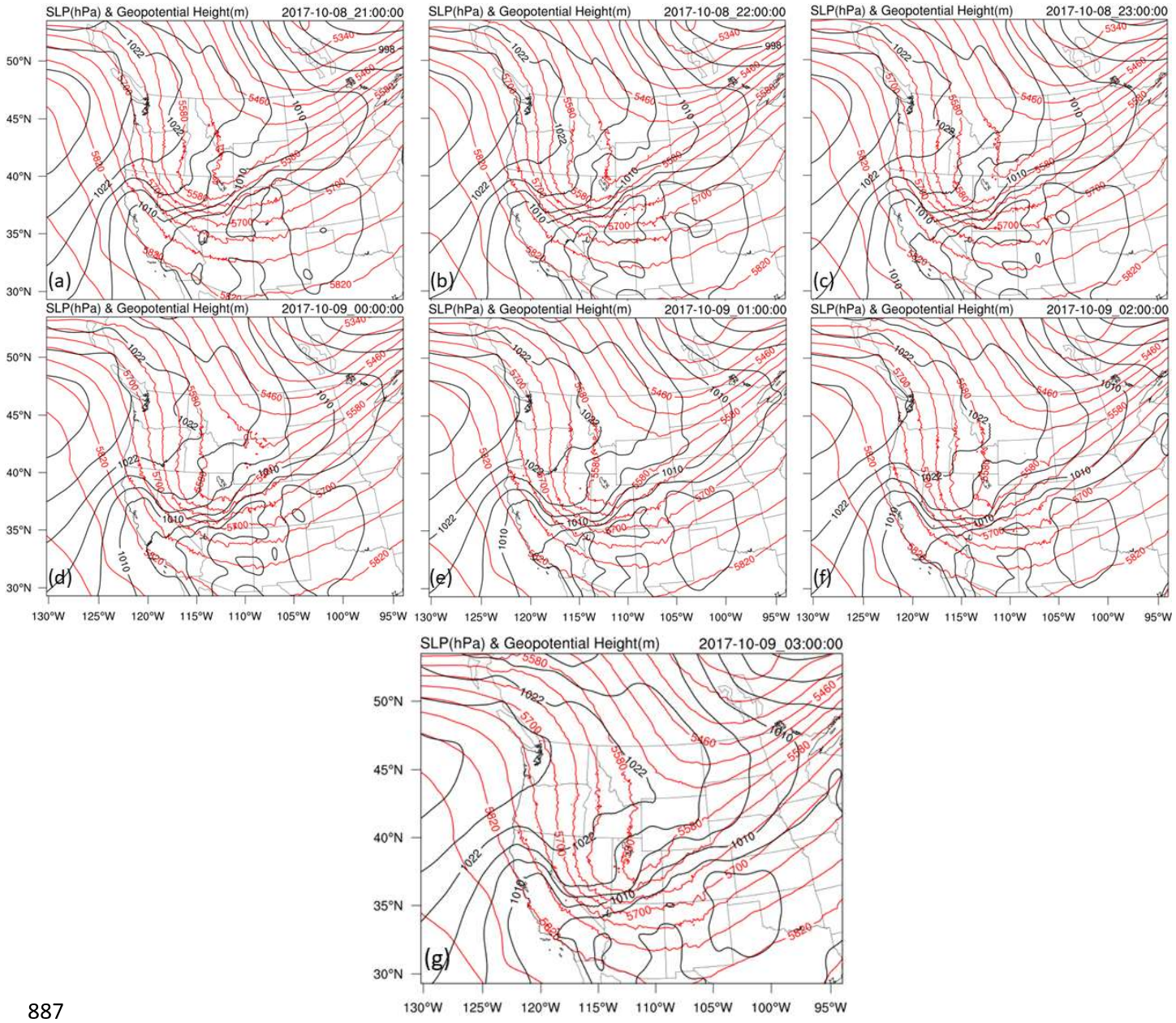

887

888 **Figure 12** Simulated MSLP (solid in black) and 500 hPa geopotential height (solid in red) valid
889 for October 8th, 21 UTC to October 9th, 03 UTC in increments of one hour (Domain 1).

890 **Figure 13** (WRF-ARW Simulated Soundings Upstream Verification)

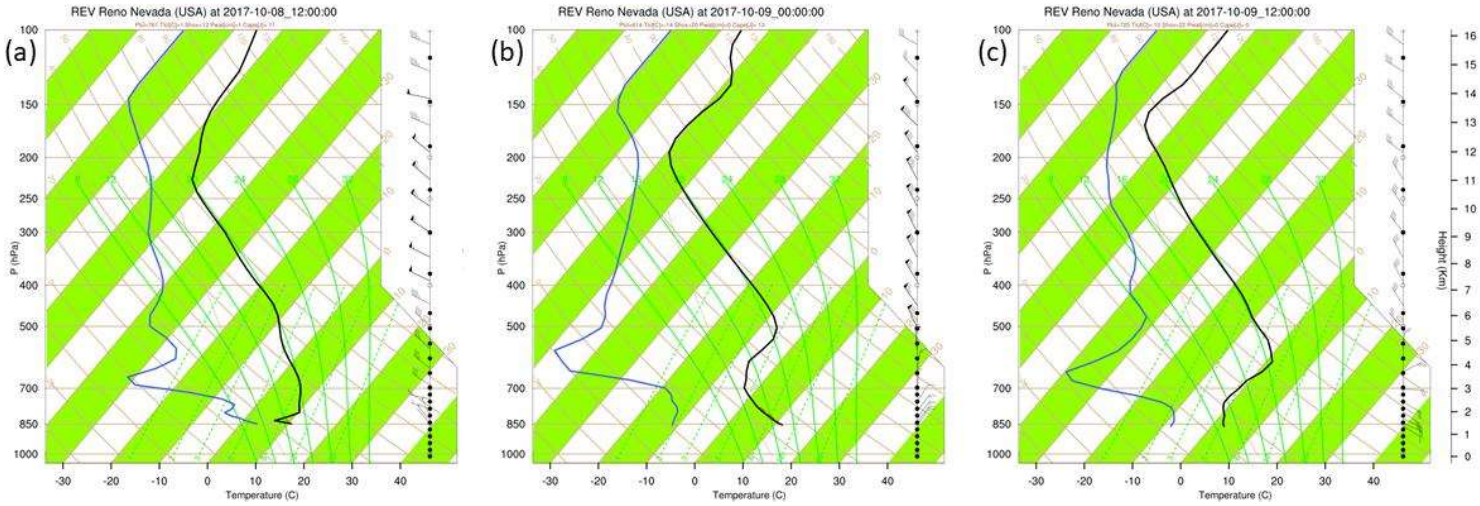

892 **Figure 13** WRF-ARW simulated soundings for Reno, Nevada (REV) valid (a) October 8th at 12
893 UTC, (b) October 9th at 00 UTC, and (c) October 9th at 12 UTC (Domain 2).

894 **Figure 14** (300 hPa Jet)

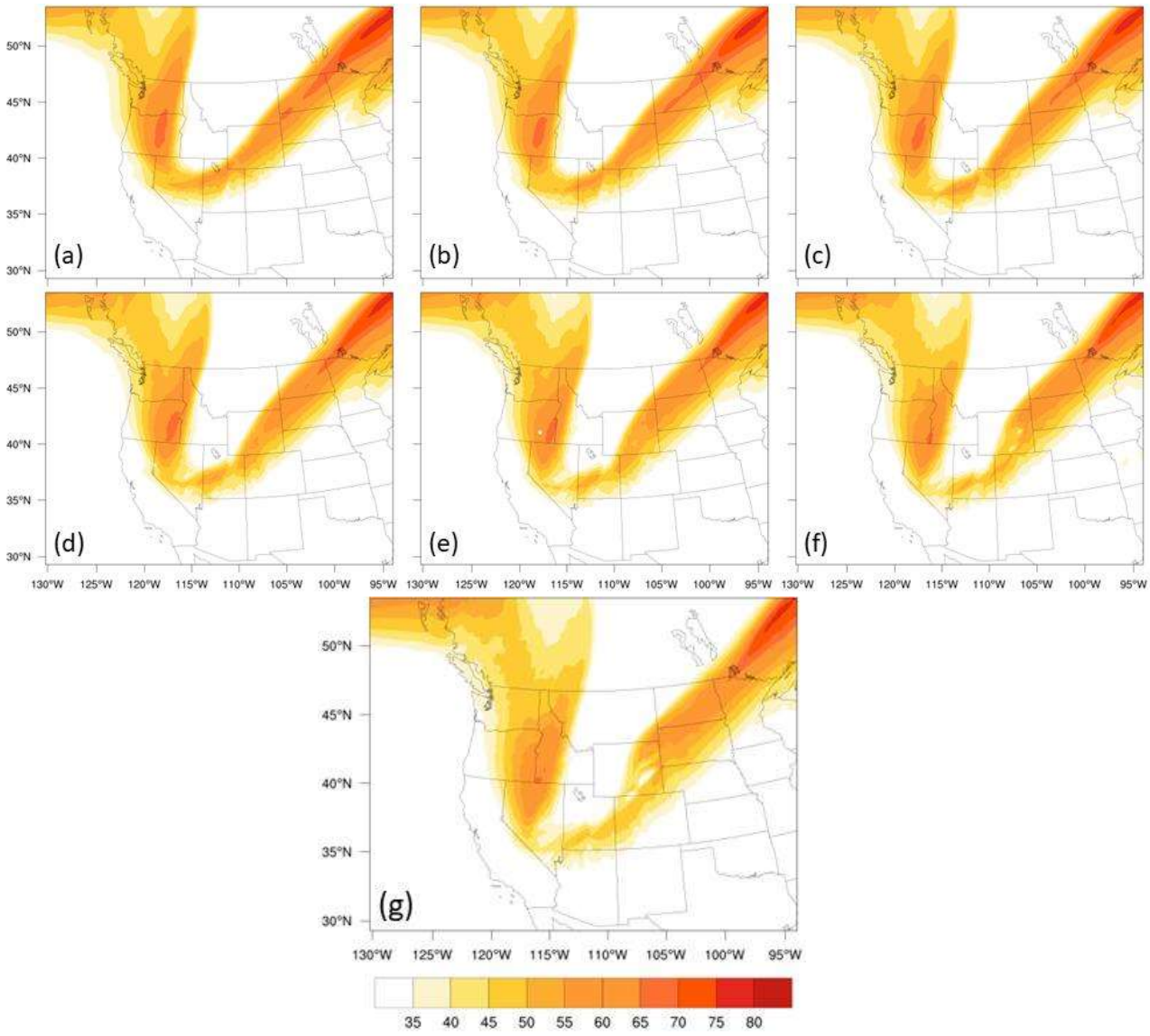

895

896

897 **Figure 14** WRF-ARW simulated jet stream isotachs at 300 hPa (fill in ms^{-1}) valid a-c) October
898 8th at 21-23 UTC, d-g) October 9th 00-03 UTC (Domain 1).

899 **Figure 15** (Temperature Advection)

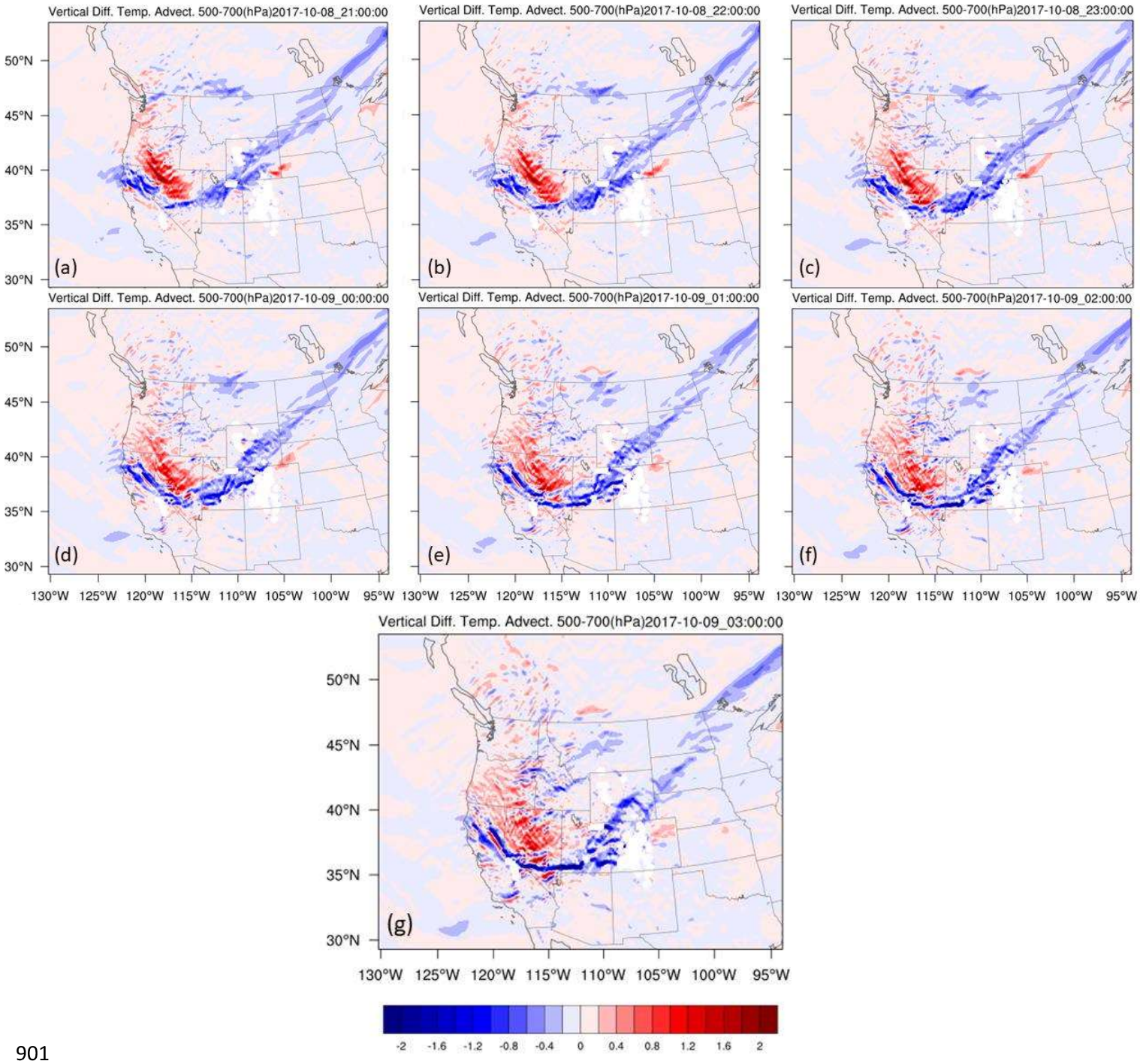

901

902 **Figure 15** Simulated vertical differential temperature advection between 500 hPa-700 hPa (Ts^{-1})
903 valid a-c) October 8th at 21-23 UTC, d-g) October 9th 00-03 UTC (Domain 1).

904 **Figure 16** (Domain 1 Cross Section)

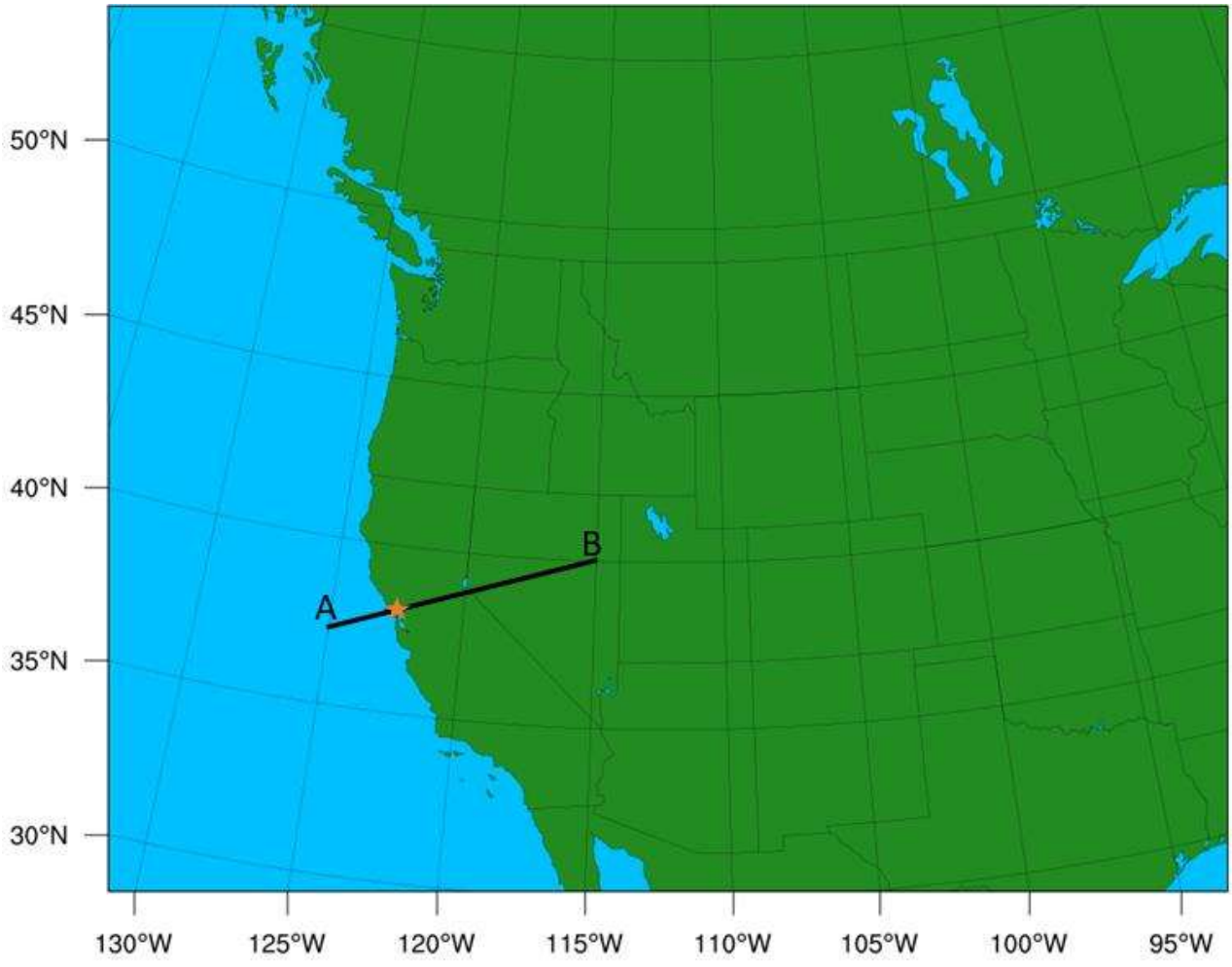

905

906 **Figure 16** Domain 1 cross section configuration. Star represents Tubbs Fire location.

907

908 **Figure 17** (Cross Section D01 Total Winds, Theta, Vectors)

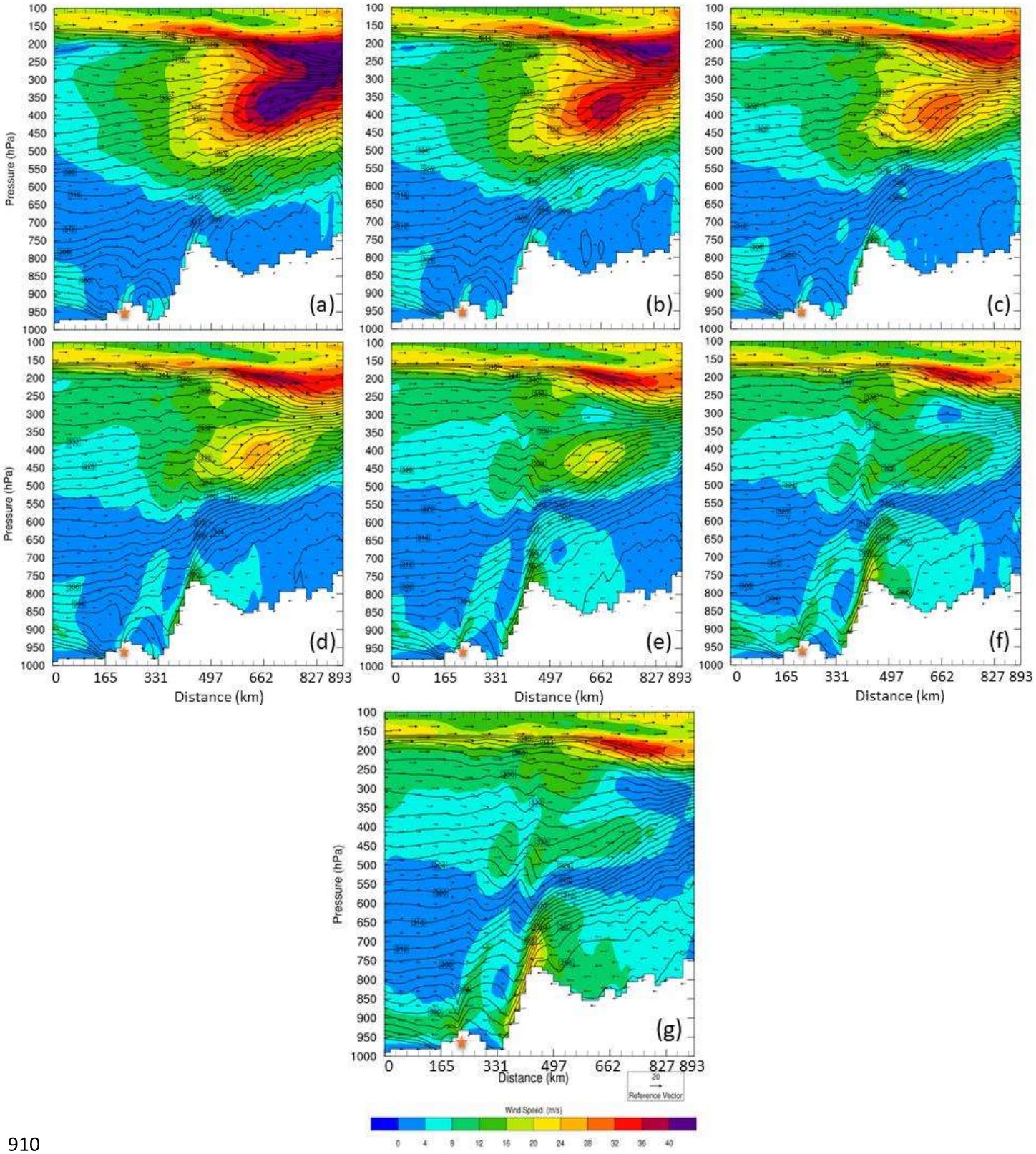

910

911 **Figure 17** Vertical cross section of simulated total wind isotachs (fill in ms^{-1}), theta (solid in K),
912 and wind vectors (ms^{-1}) valid a-c) October 8th at 21-23 UTC, d-g) October 9th 00-03 UTC
913 (Domain 1).

914 **Figure 18** (Cross Section D01 Z Wind, Theta, Vectors)

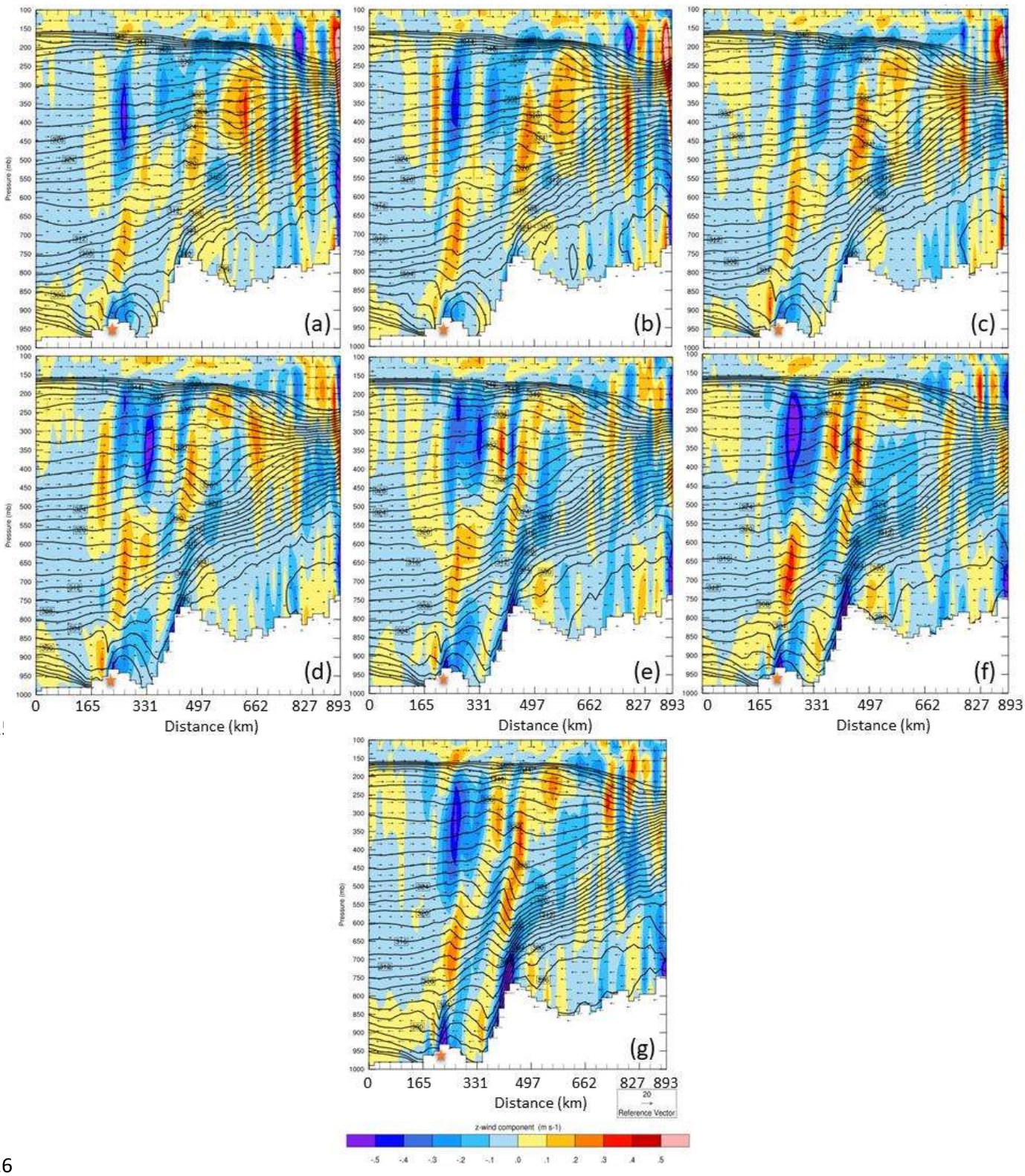

915

916

Figure 18 Vertical cross section of simulated vertical wind velocity component (fill in ms^{-1}), horizontal wind vectors (ms^{-1}) and theta (solid in K) valid a-c) October 8th at 21-23 UTC, d-g) October 9th 00-03 UTC (Domain 1).

Figure 19 (Domain 3 Cross Section)

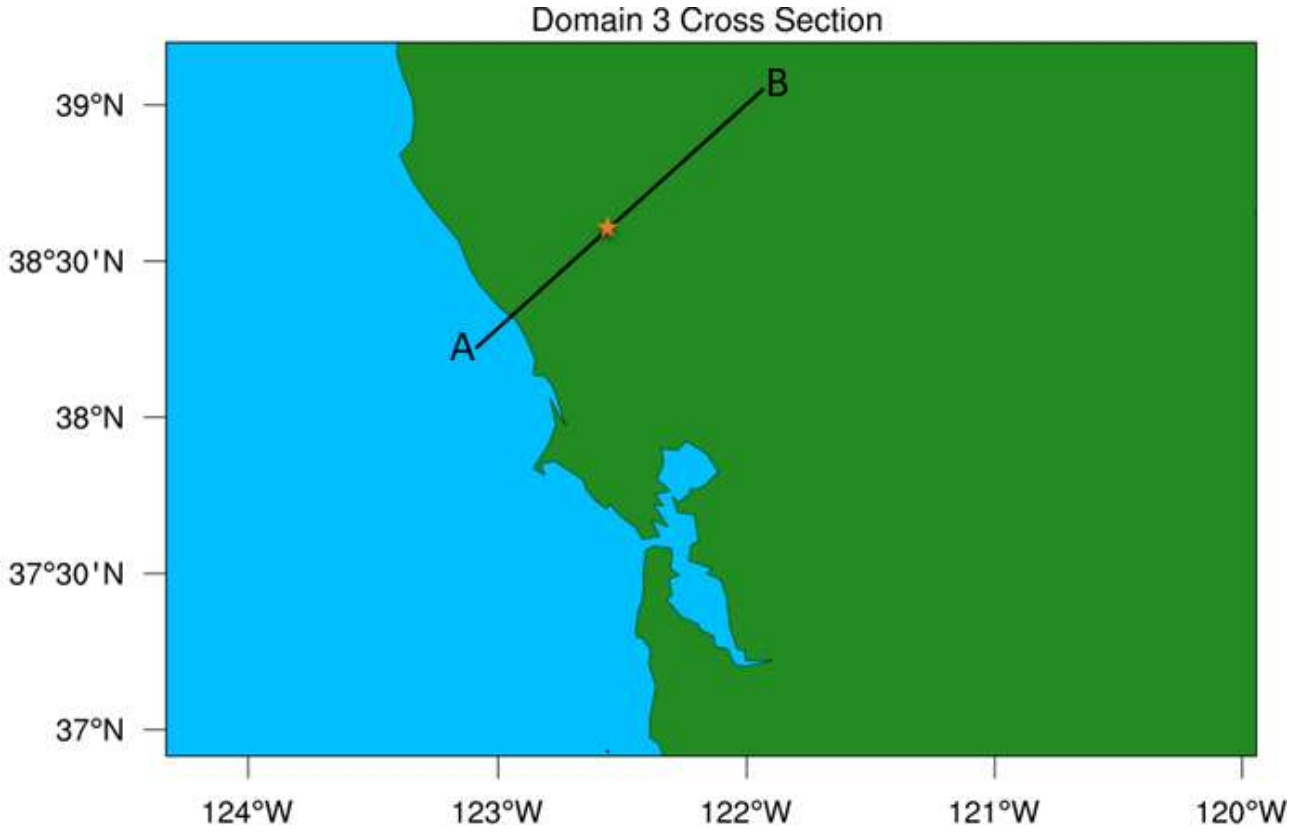

Figure 19 Domain 3 cross section configuration. Star represents Tubbs Fire location.

923 **Figure 20** (Simulated WRF-ARW Soundings for Tubbs Fire Location)

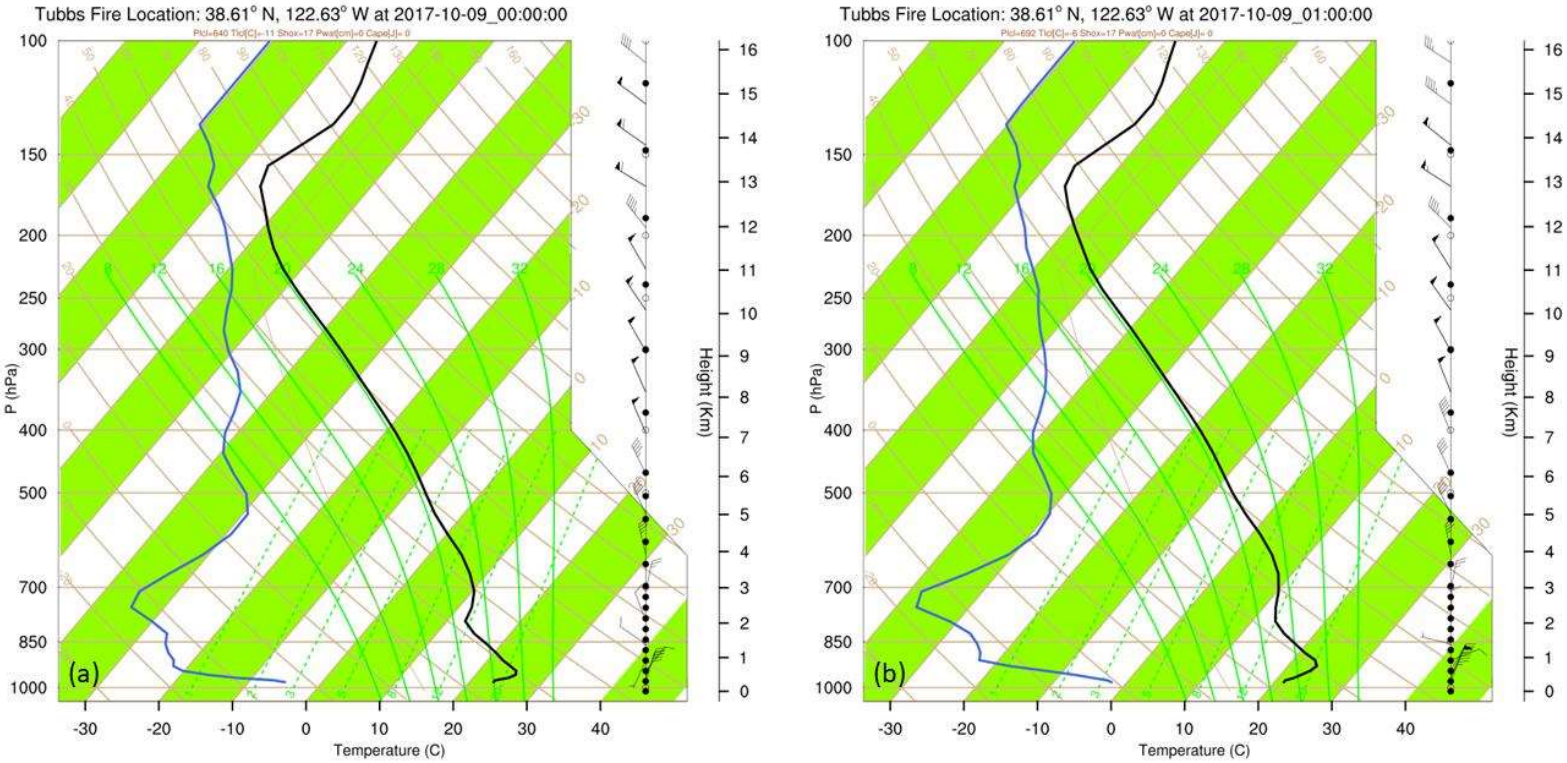

925 **Figure 20**: WRF-ARW simulated soundings for the Tubbs Fire (2017) initialization location,
926 California valid (a) October 9th at 00 UTC, and (b) October 9th at 01 UTC (Domain 3).

927 **Figure 21** (Cross Section D03 Total Winds, Theta, Vectors)

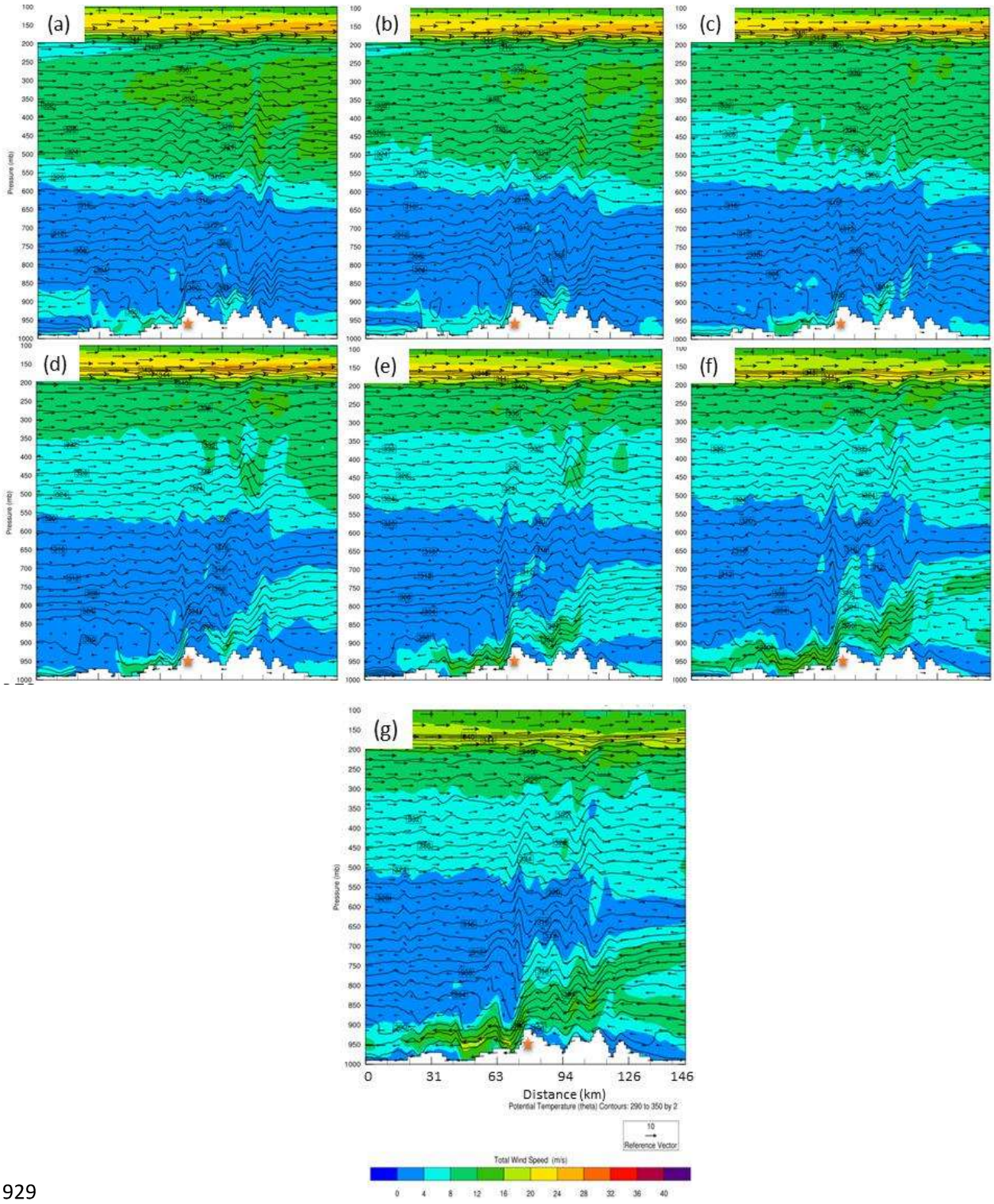

929

930 **Figure 21**: Domain 3 Vertical cross section of simulated total wind isotachs (fill ms^{-1}), theta
931 (solid in K), and wind vectors (ms^{-1}) valid a-c) October 8th at 21-23 UTC, d-g) October 9th 00-03
932 UTC (Domain 1).

933 **Figure 22** (Bore Hovmöller Diagram)

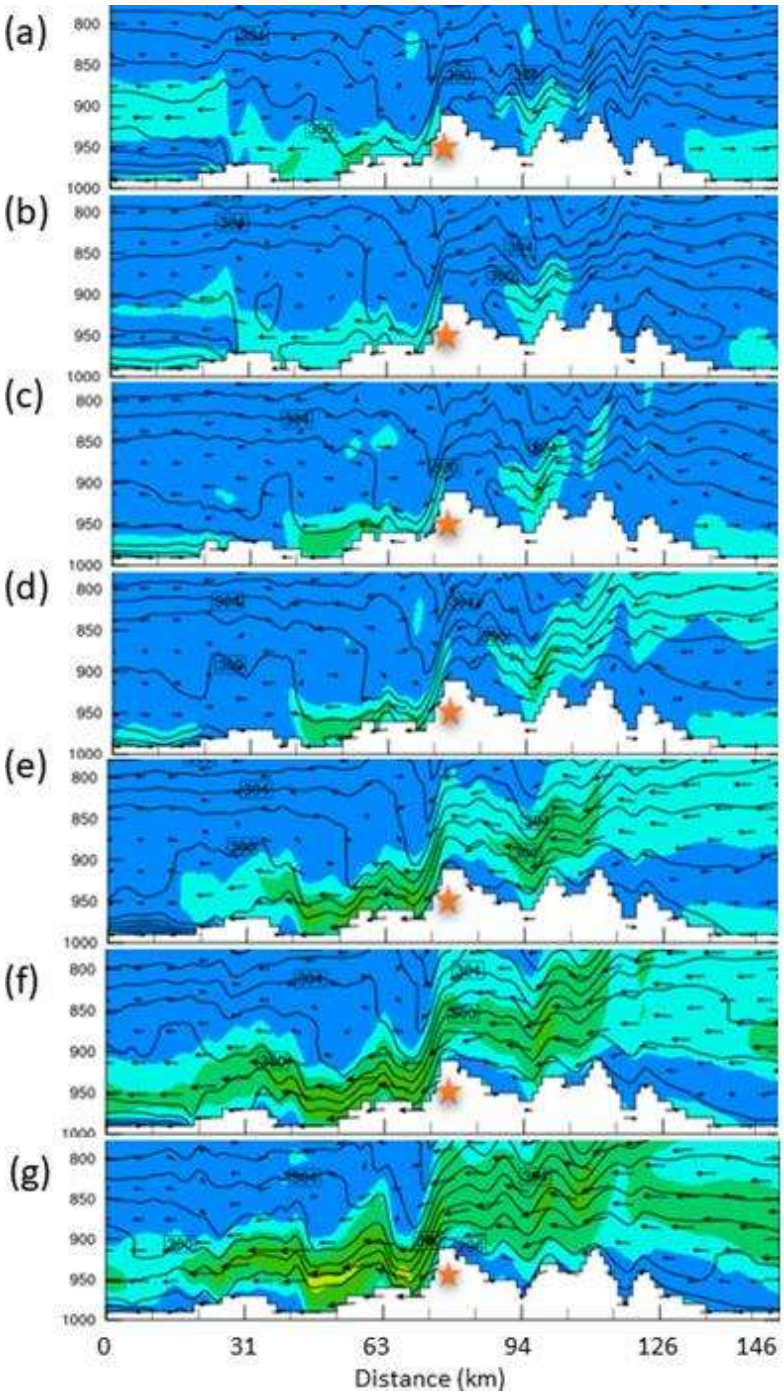

934

935 **Figure 22** Bore structure and propagation within simulated total wind isotachs (fill in ms^{-1}), theta
936 (solid in K), and wind vectors (ms^{-1}) valid a-g) October 8th at 21 UTC - October 9th at 03 UTC
937 (Domain 3).

938 **Figure 23** (Cross Section D03 Z Wind, Theta, Vectors)

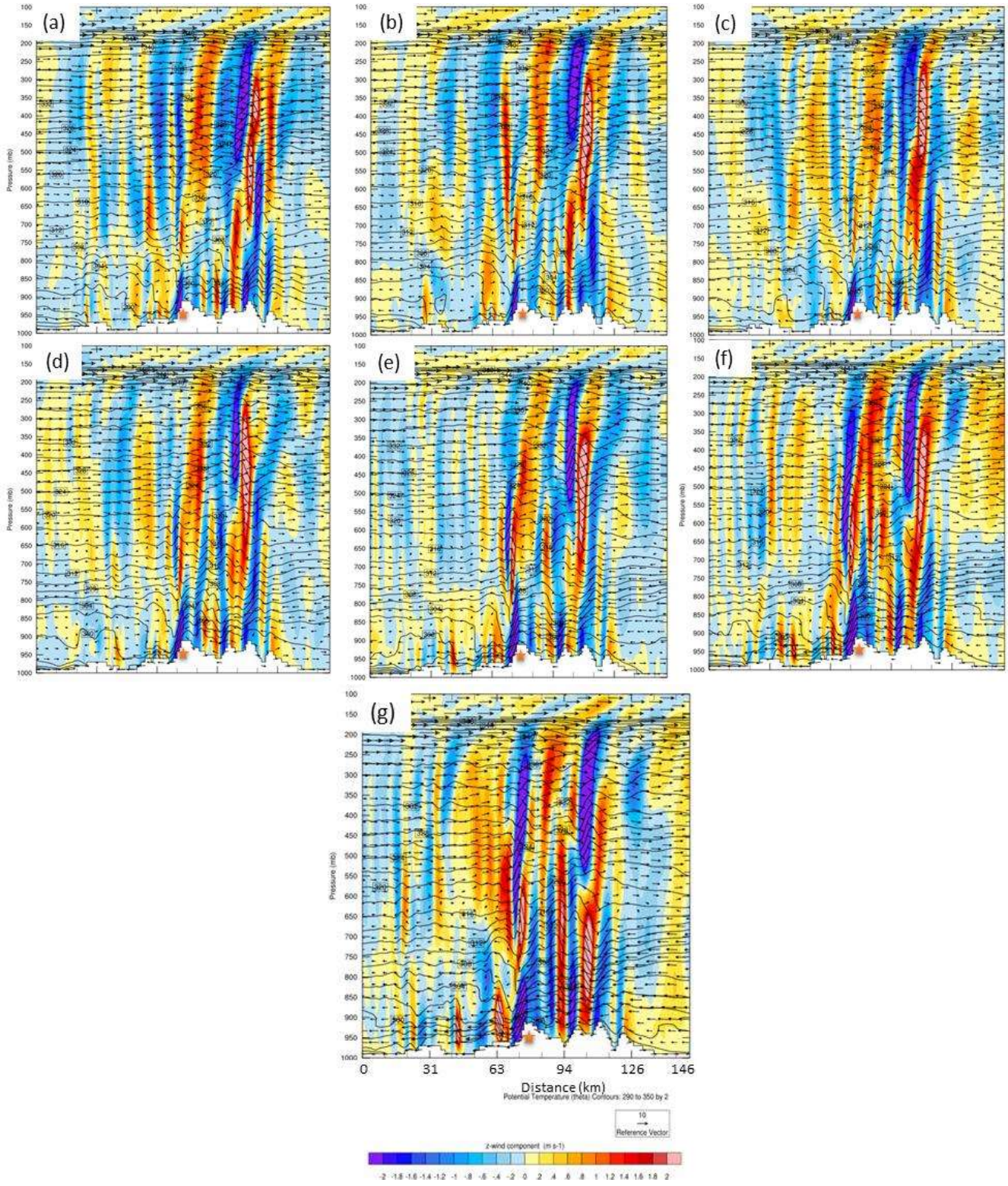

939

940

941 **Figure 23** Domain 3 vertical cross section of simulated vertical wind velocity component (fill in
942 ms^{-1}), horizontal wind vectors (ms^{-1}) and theta (solid in K) valid a-c) October 8th at 21-23 UTC,
943 d-g) October 9th 00-03 UTC (Domain 1).

Figure 1

Click here to access/download;Figure;Figure 1.PNG

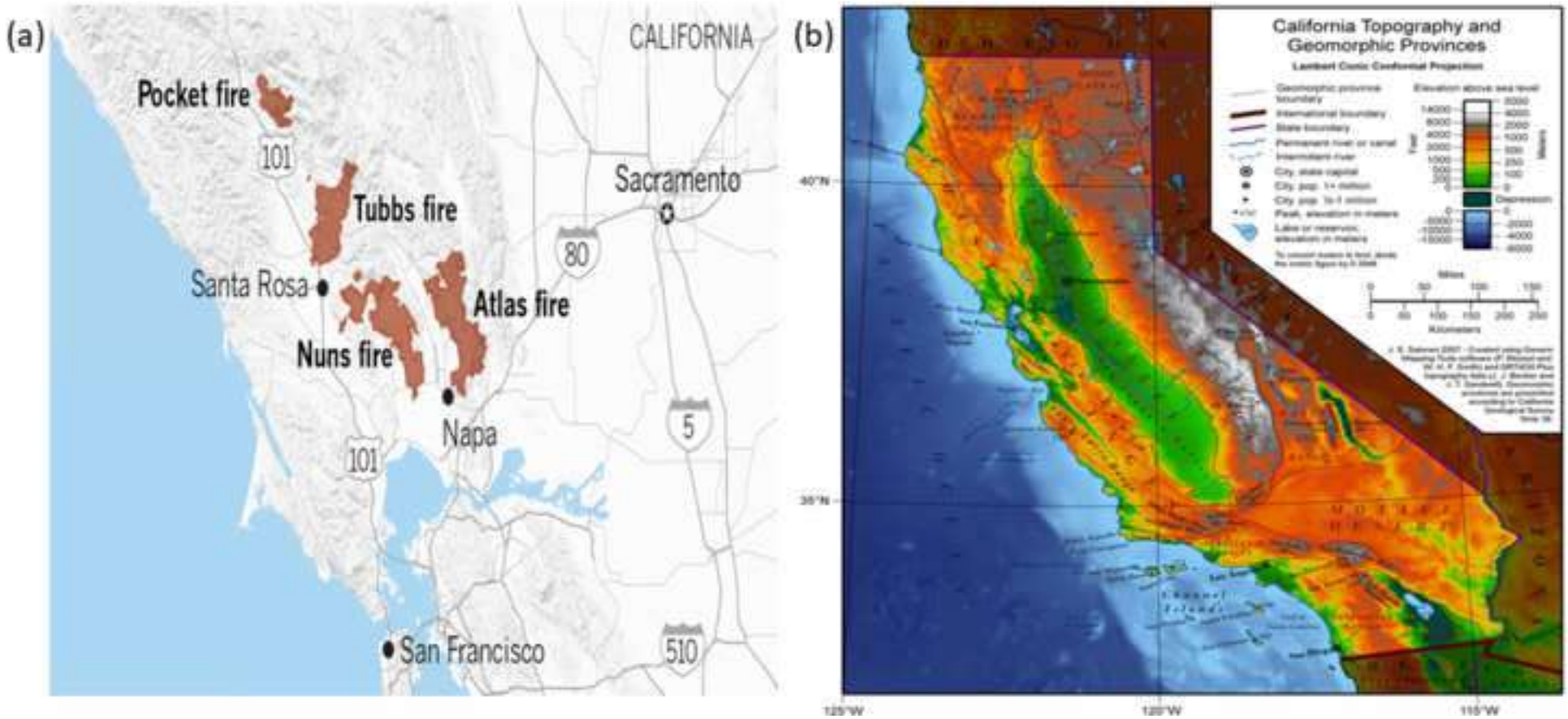

Figure 2

Click here to access/download;Figure;Figure 2.png

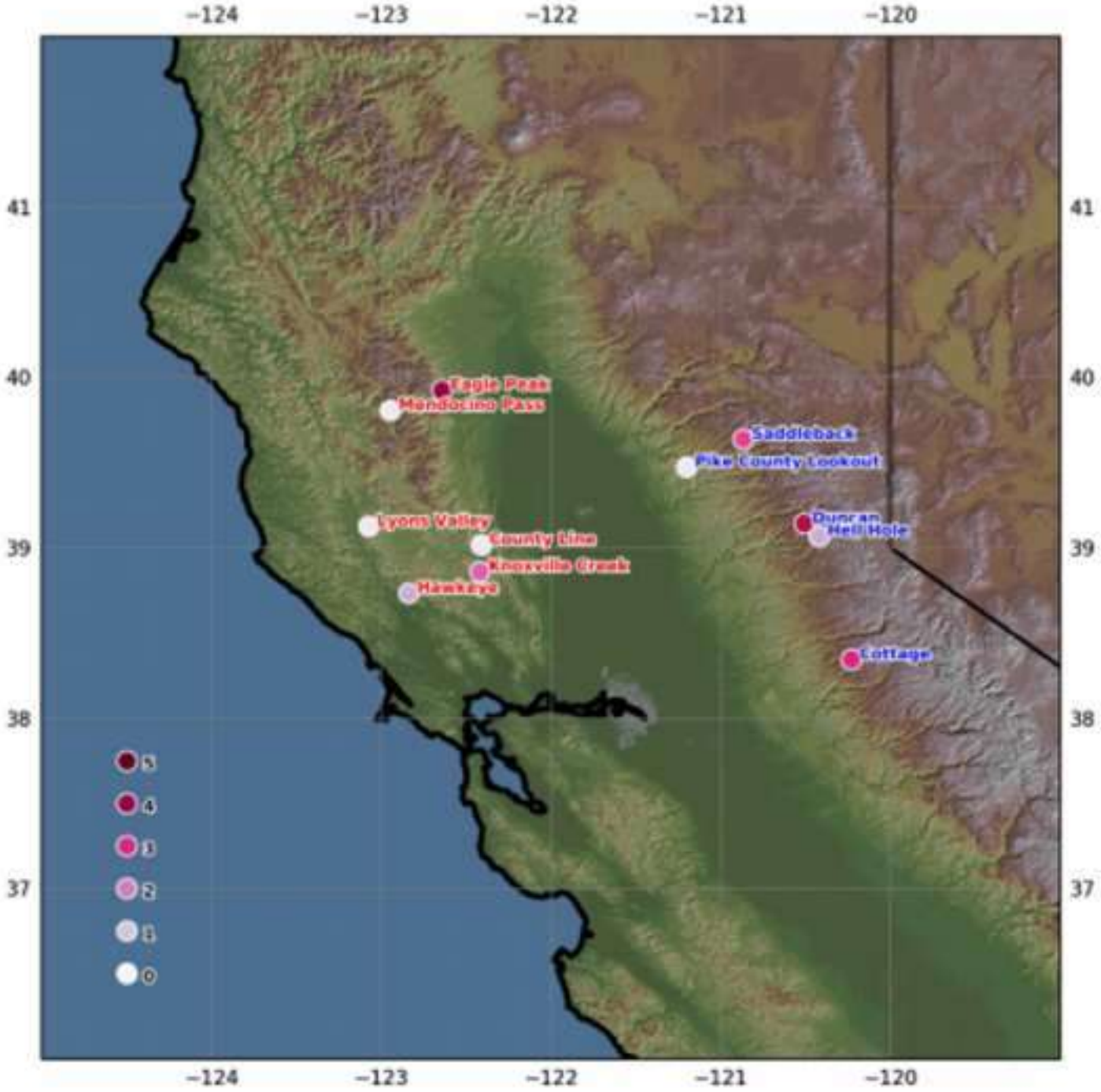

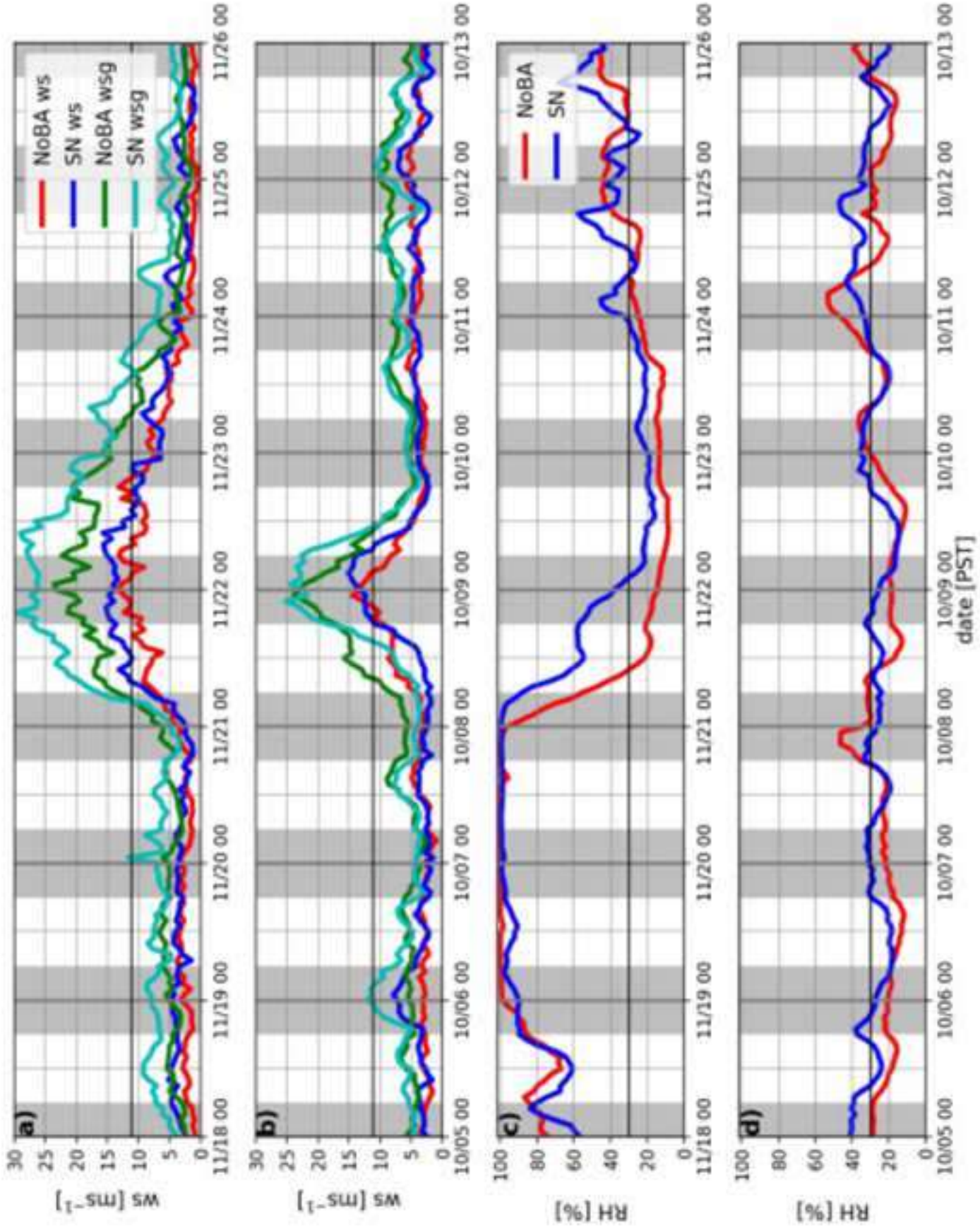

Figure 3

Figure 4

Click here to access/download;Figure;Figure 4.png

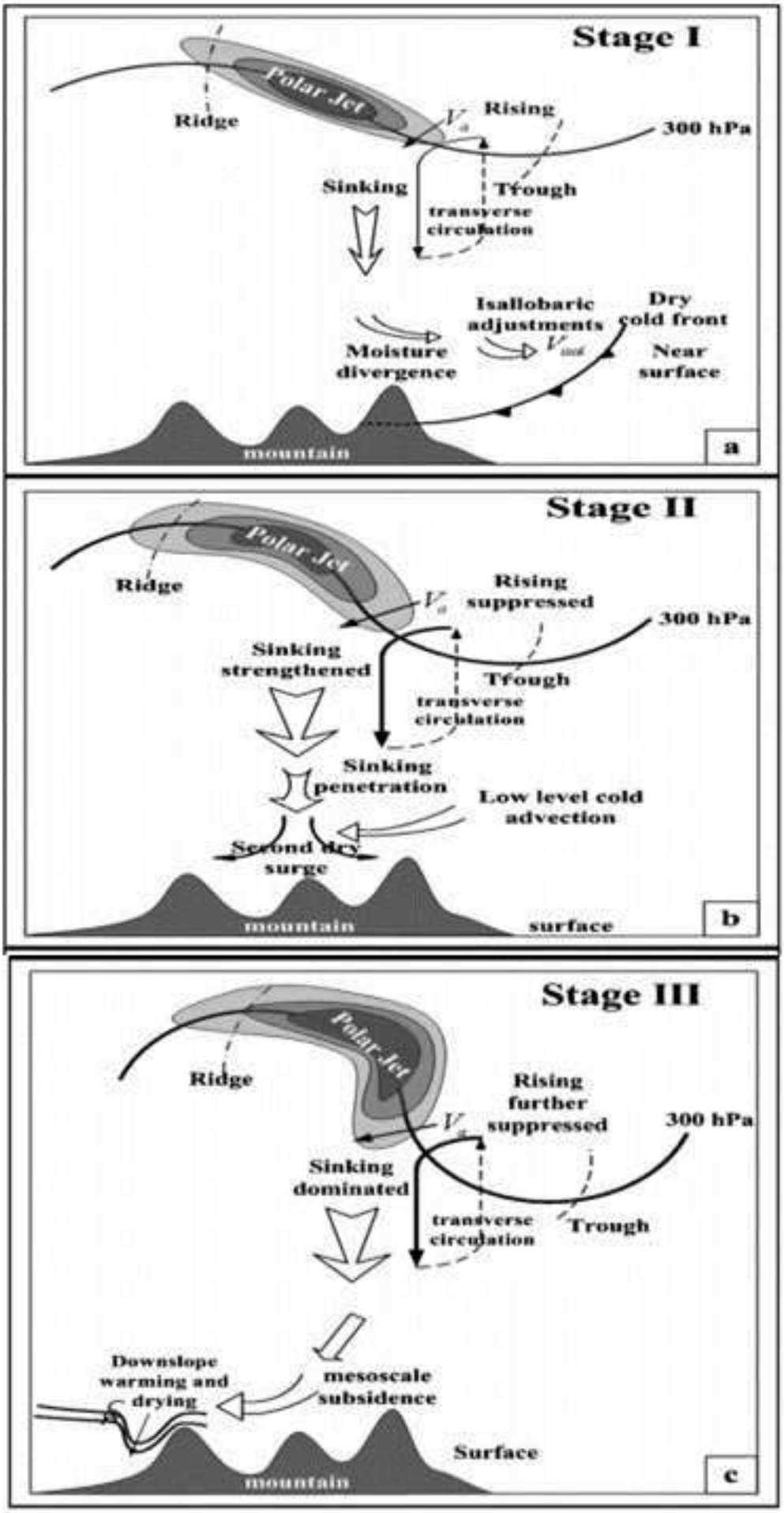

Figure 5

Click here to access/download;Figure;Figure 5.png

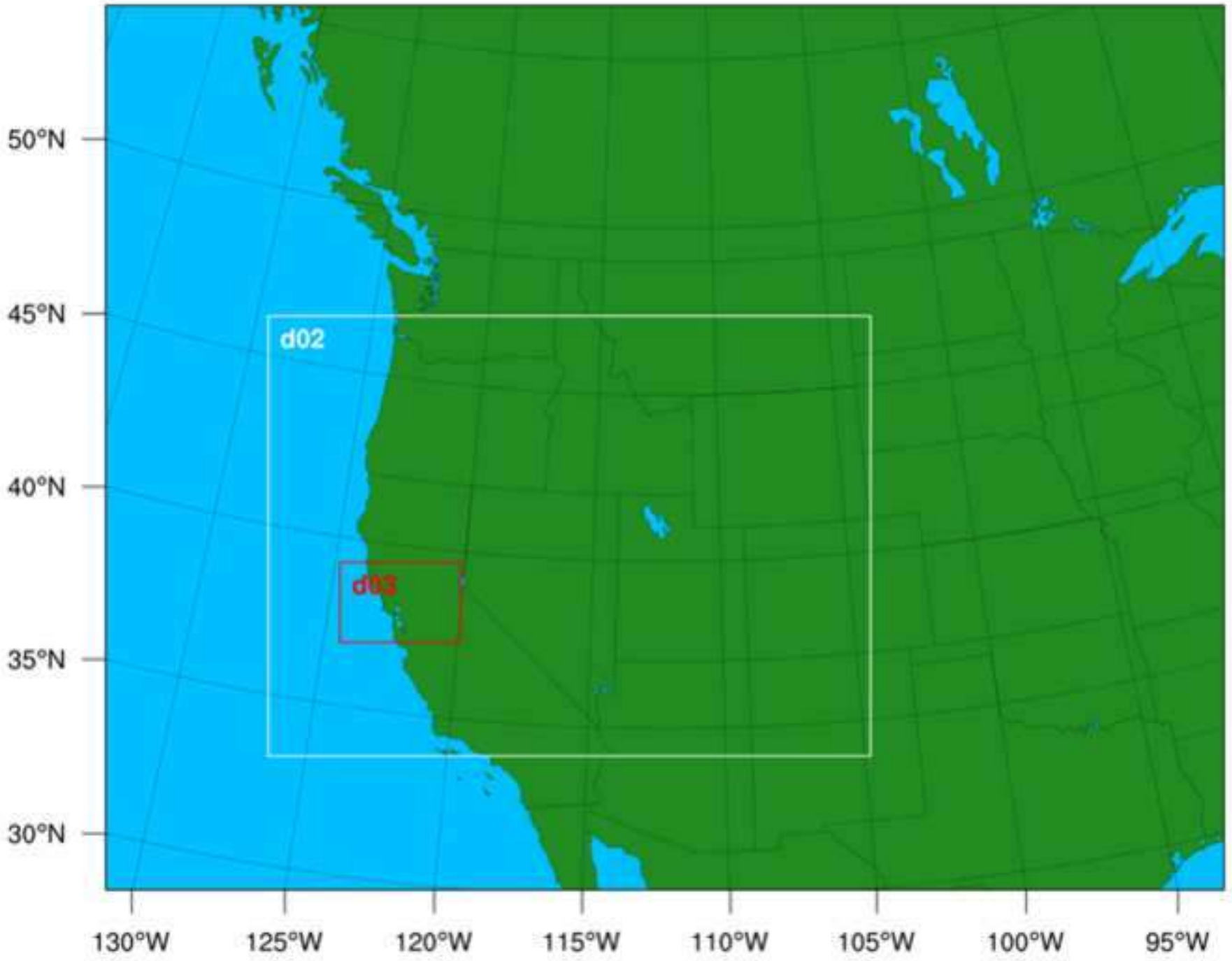

Figure 6

Click here to access/download;Figure;Figure 6.PNG

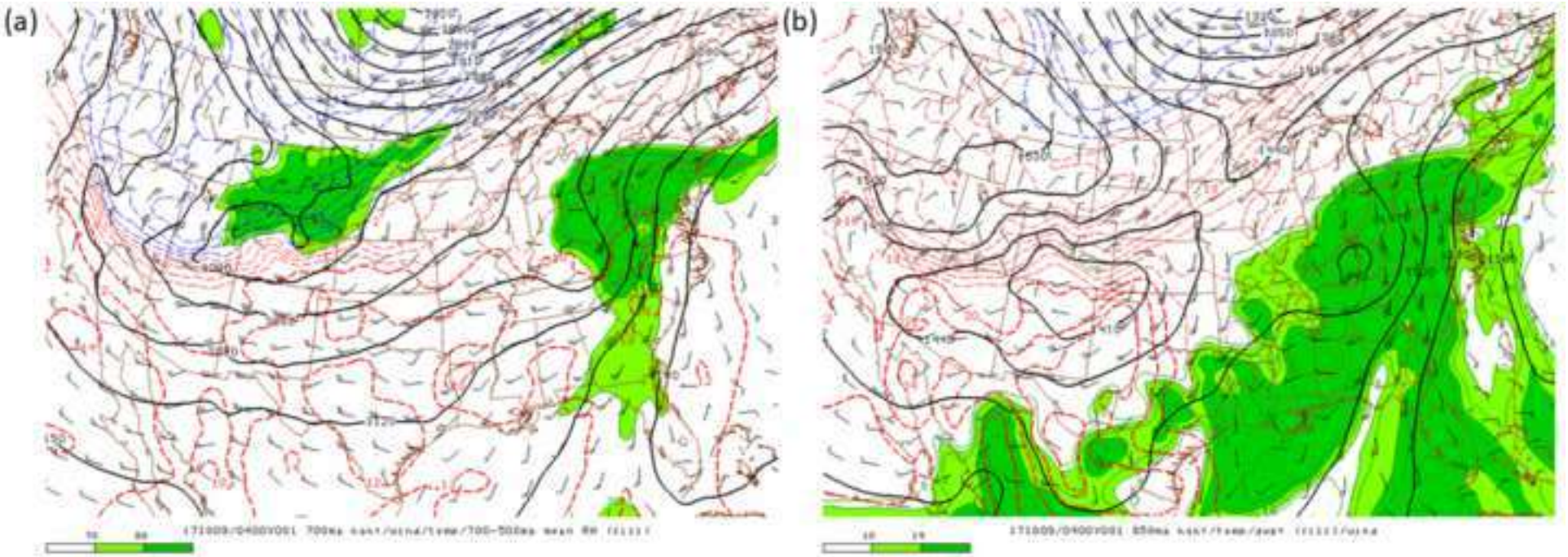

Figure 7

Click here to access/download;Figure;Figure 7.PNG

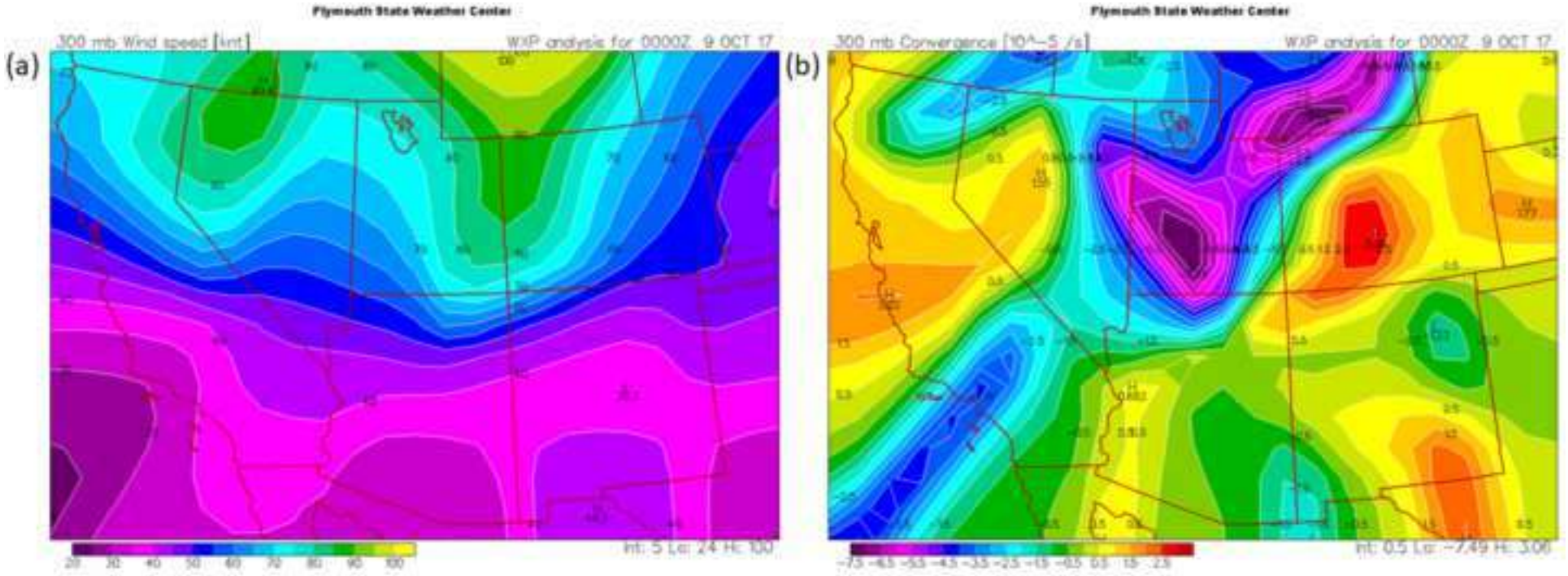

Figure 8

Click here to access/download;Figure;Figure 8.png

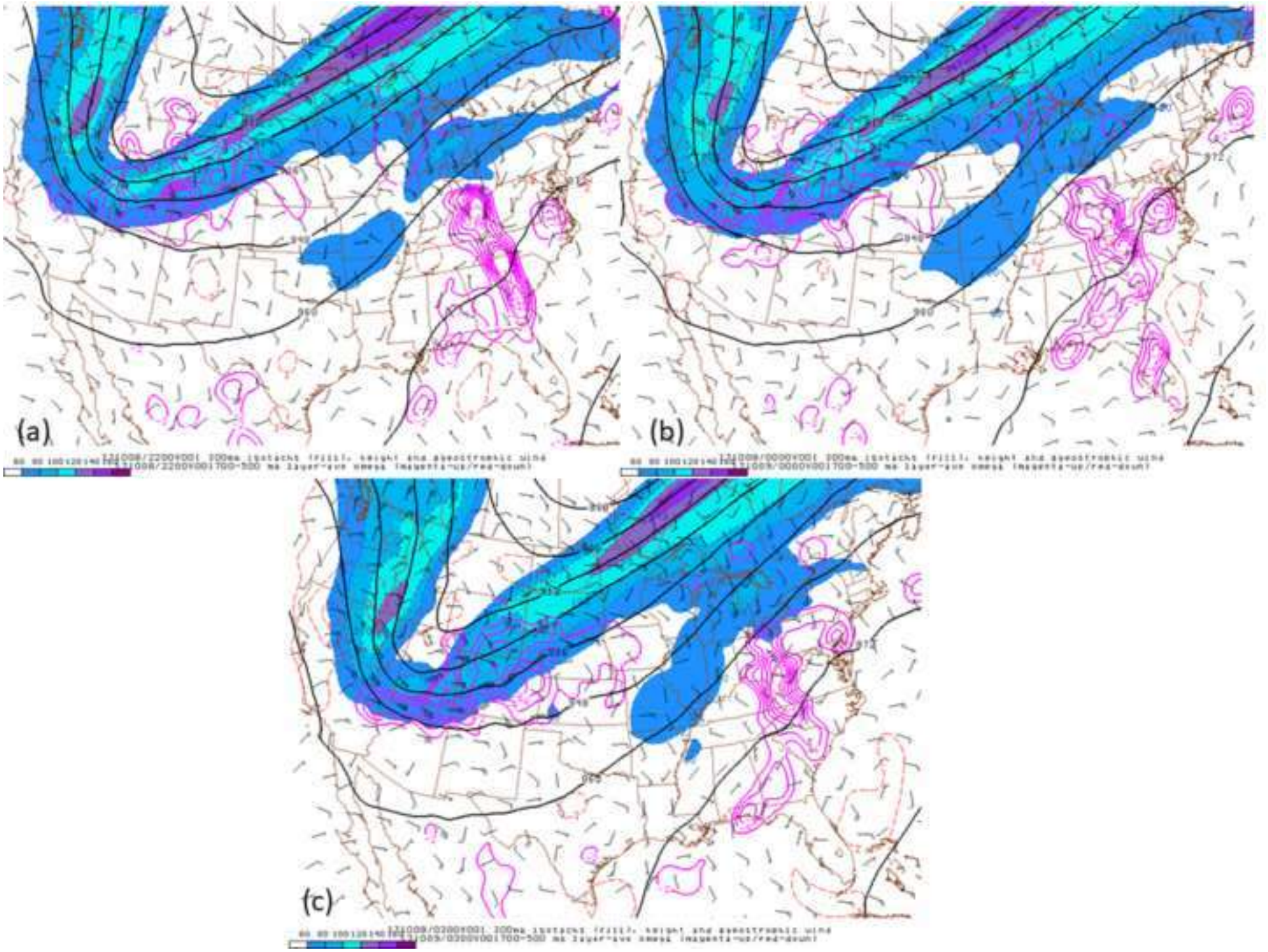

Figure 9

Click here to access/download;Figure;Figure 9.png

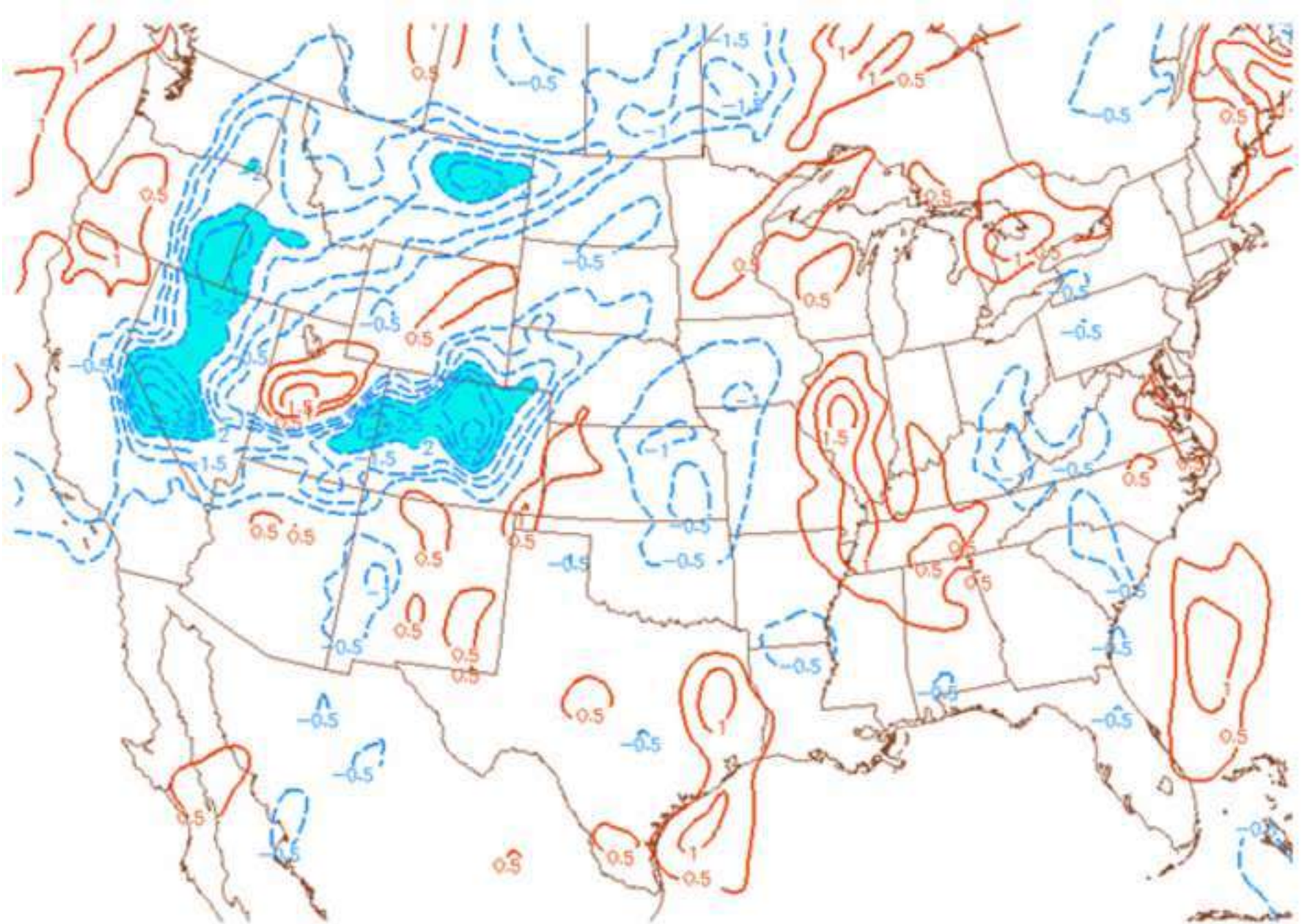

Figure 10

Click here to access/download;Figure;Figure 10.PNG

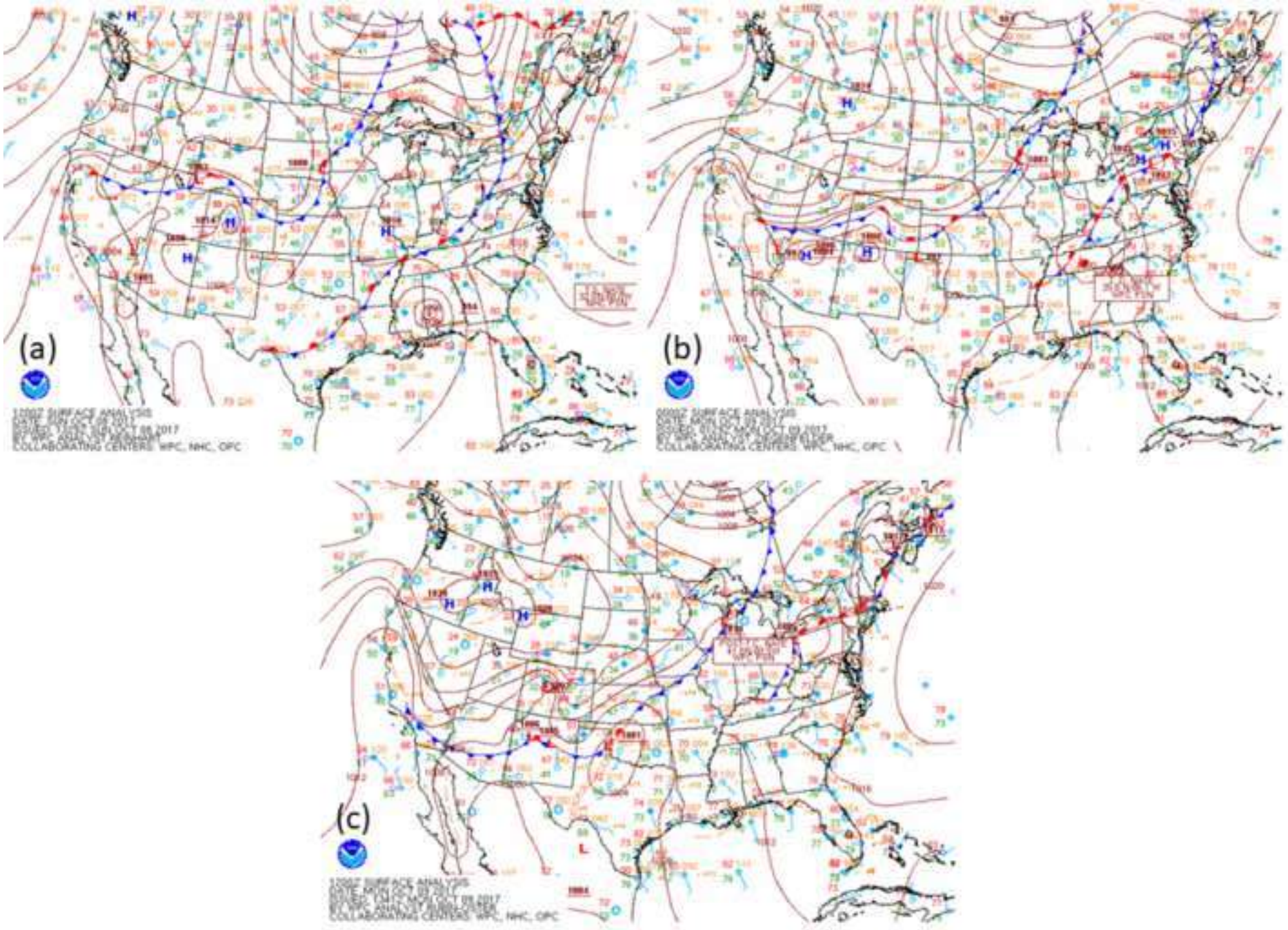

Figure 11

Click here to access/download;Figure;Figure 11.png

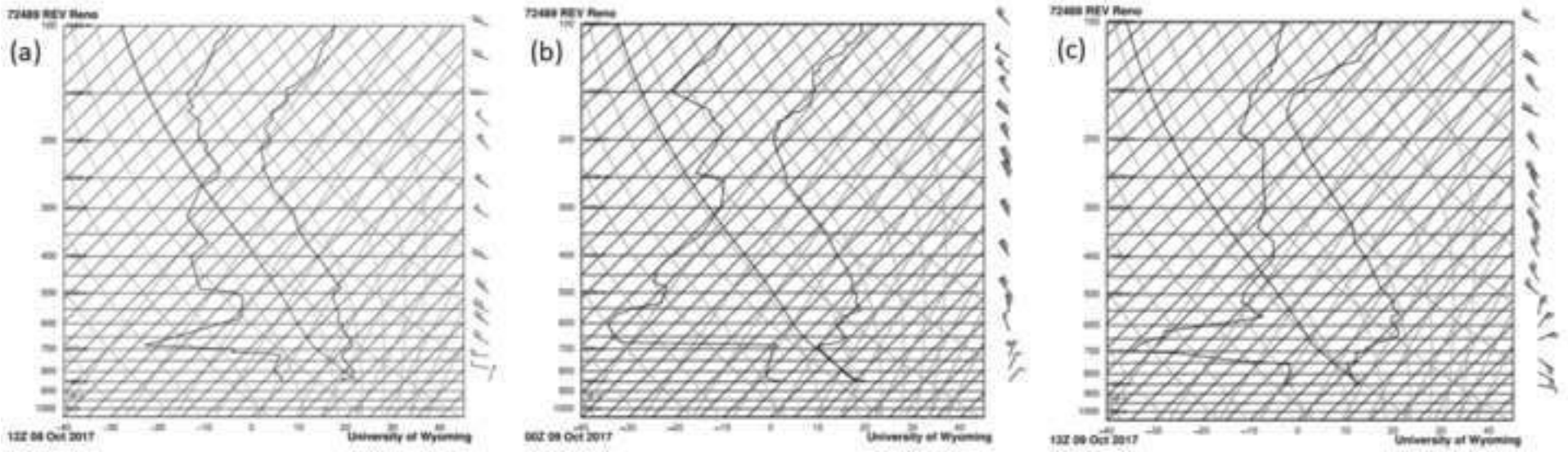

Figure 12a

Click here to access/download;Figure;Figure 12a.PNG

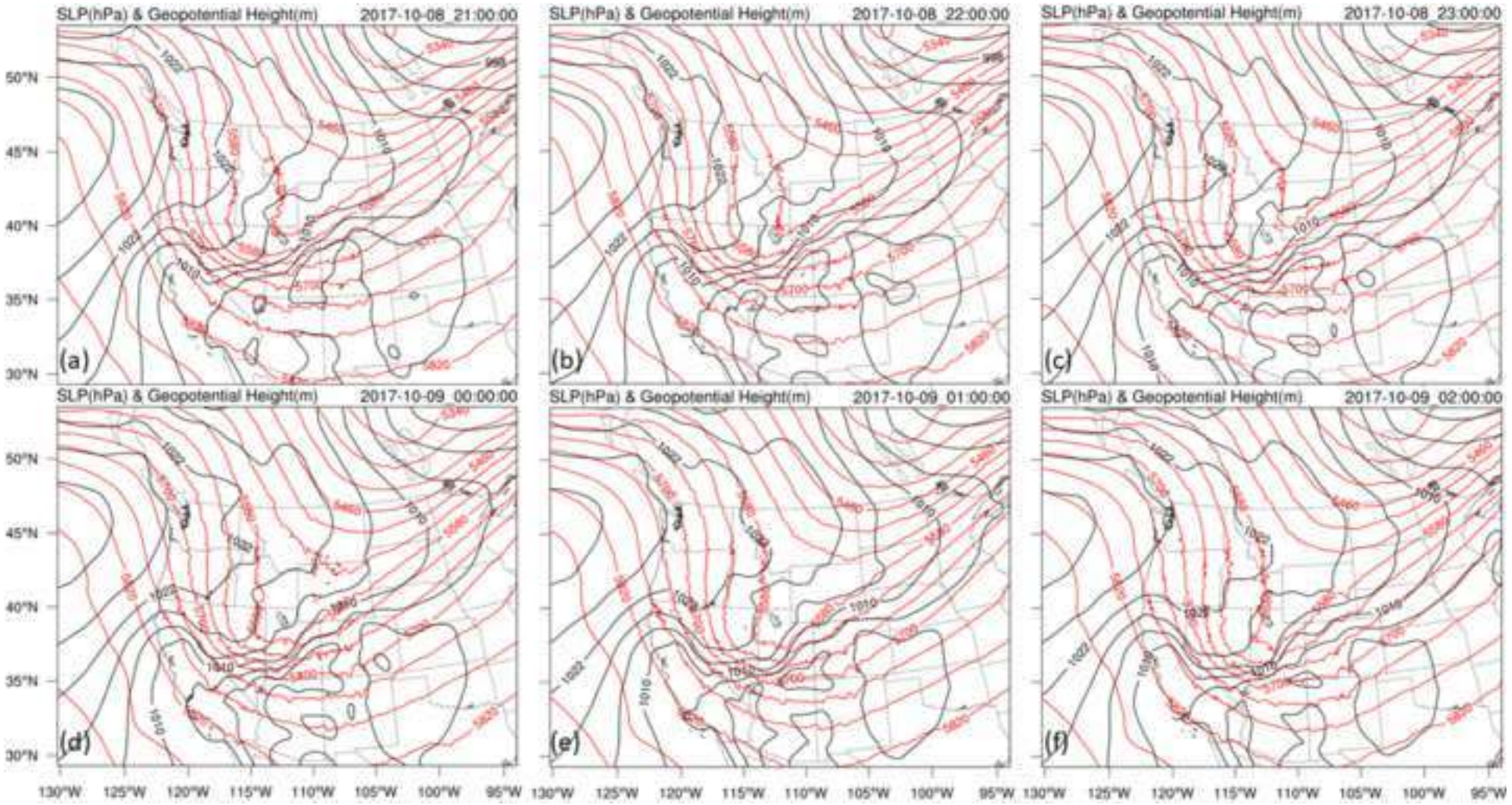

Figure 12b

Click here to access/download;Figure;Figure 12b.PNG

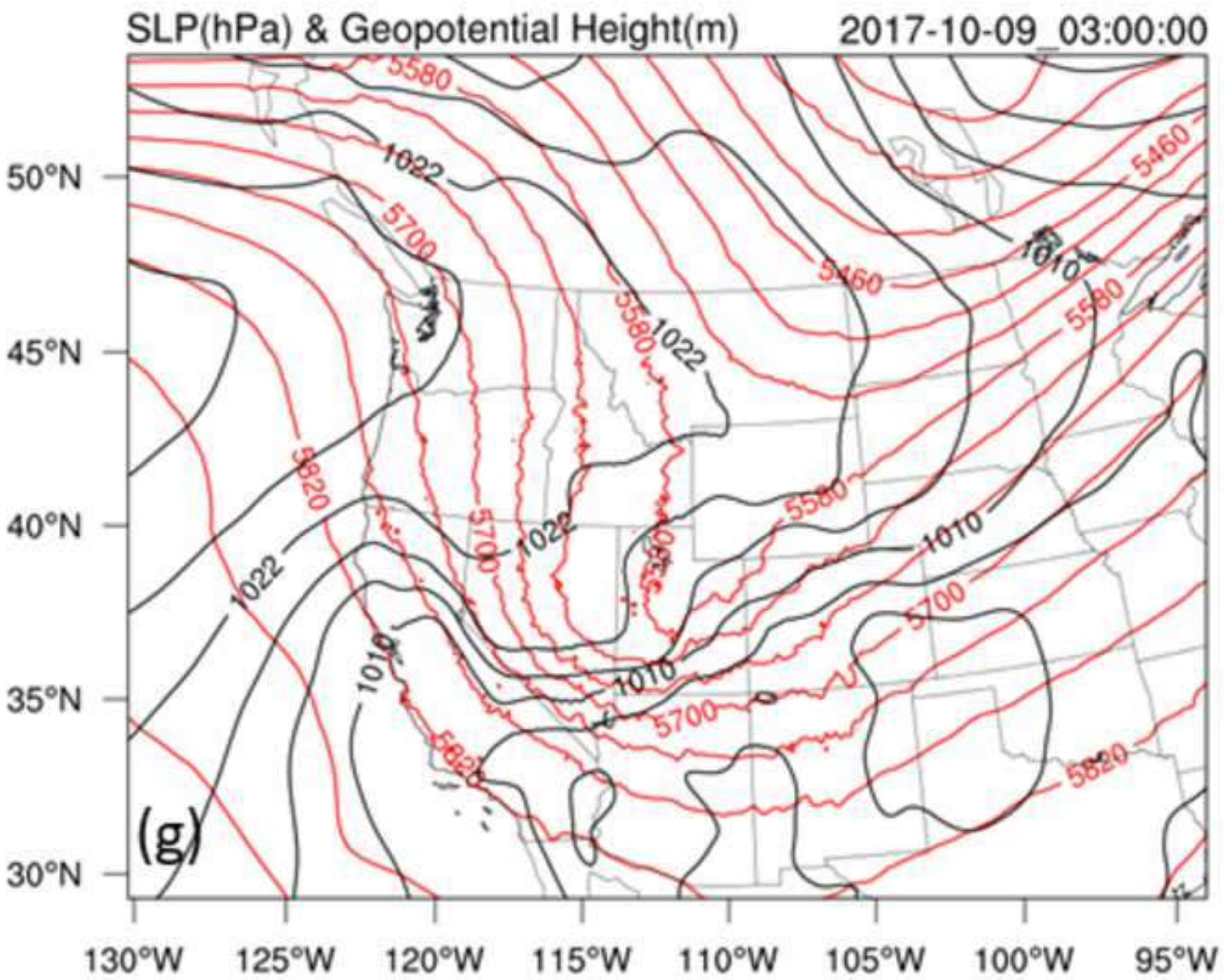

Figure 13

Click here to access/download;Figure;Figure 13.png

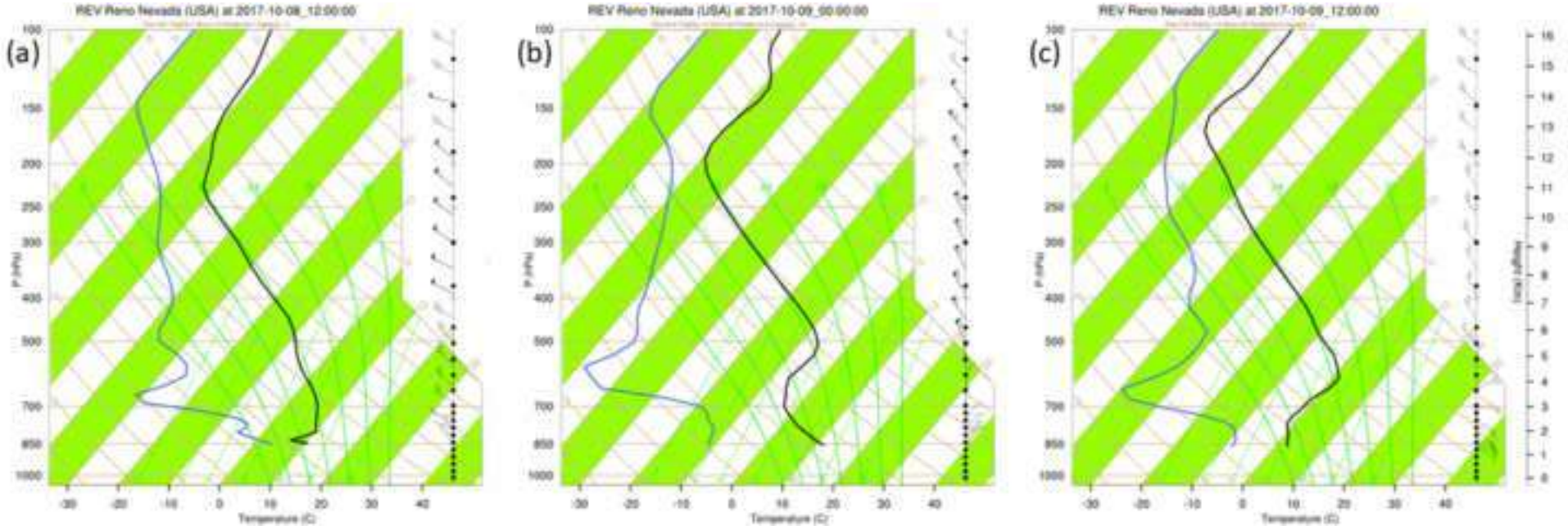

Figure 14a

Click here to access/download;Figure;Figure 14a.png

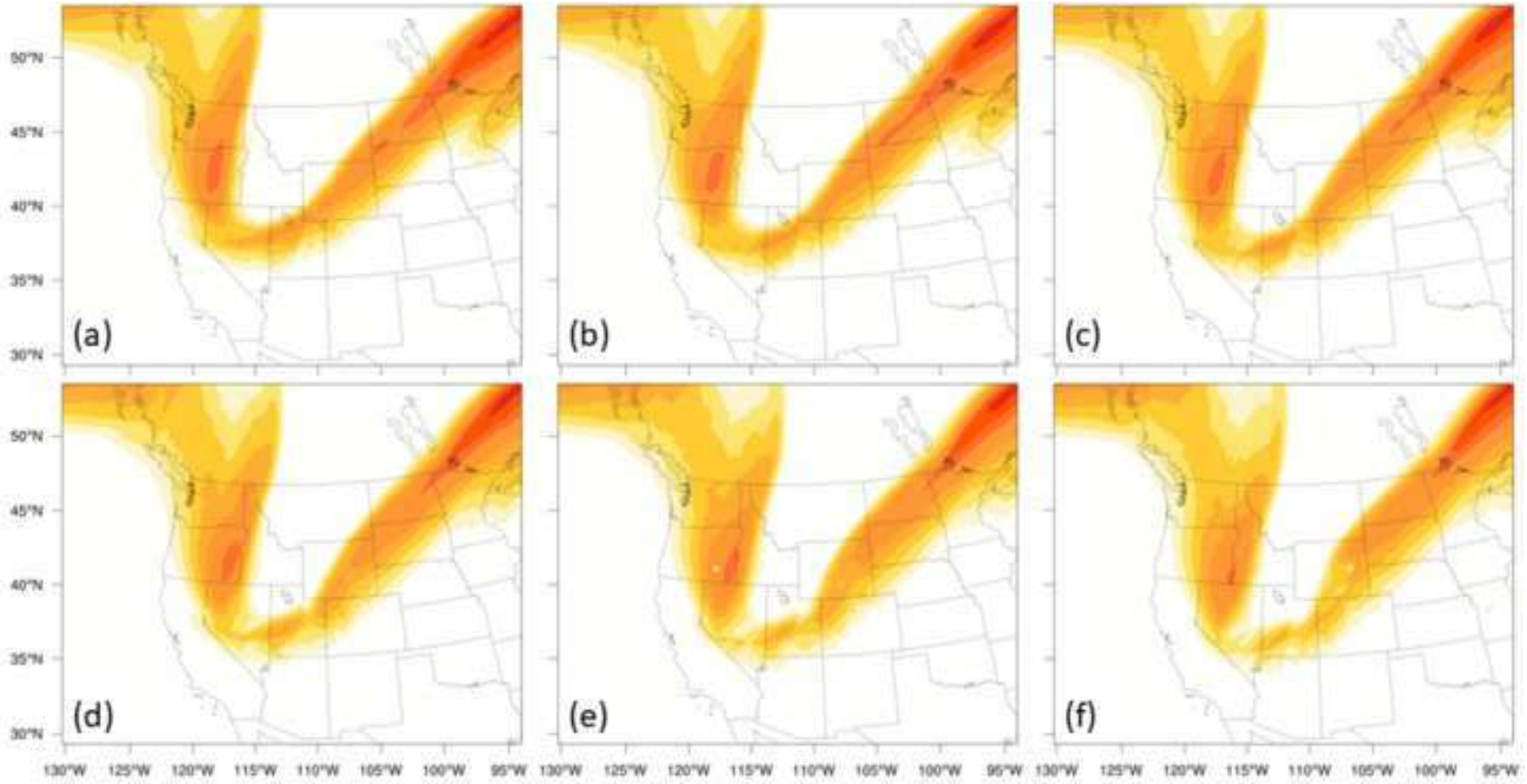

Figure 14b

Click here to access/download;Figure;Figure 14b.png

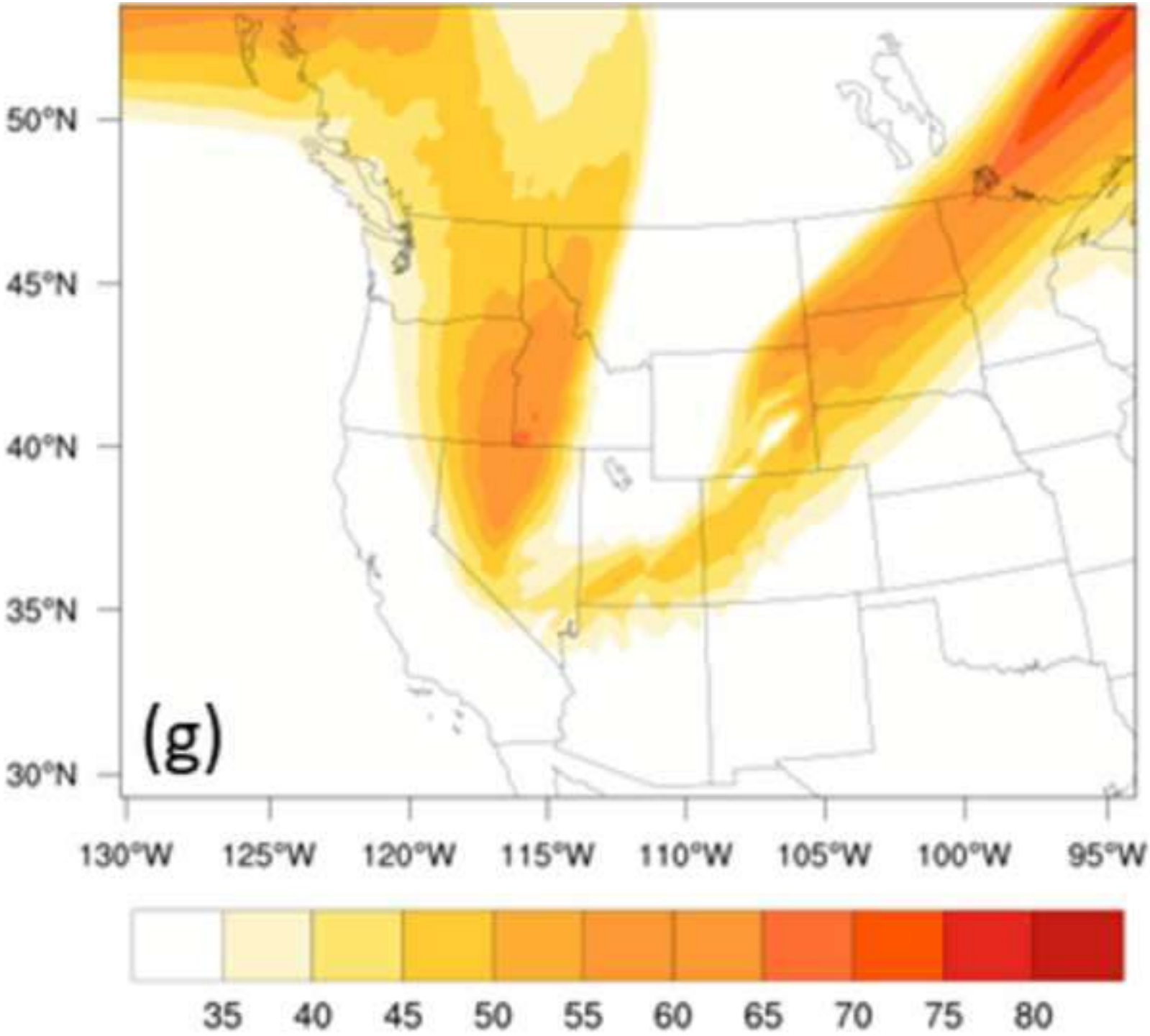

Figure 15a

Click here to access/download;Figure;Figure 15a.PNG

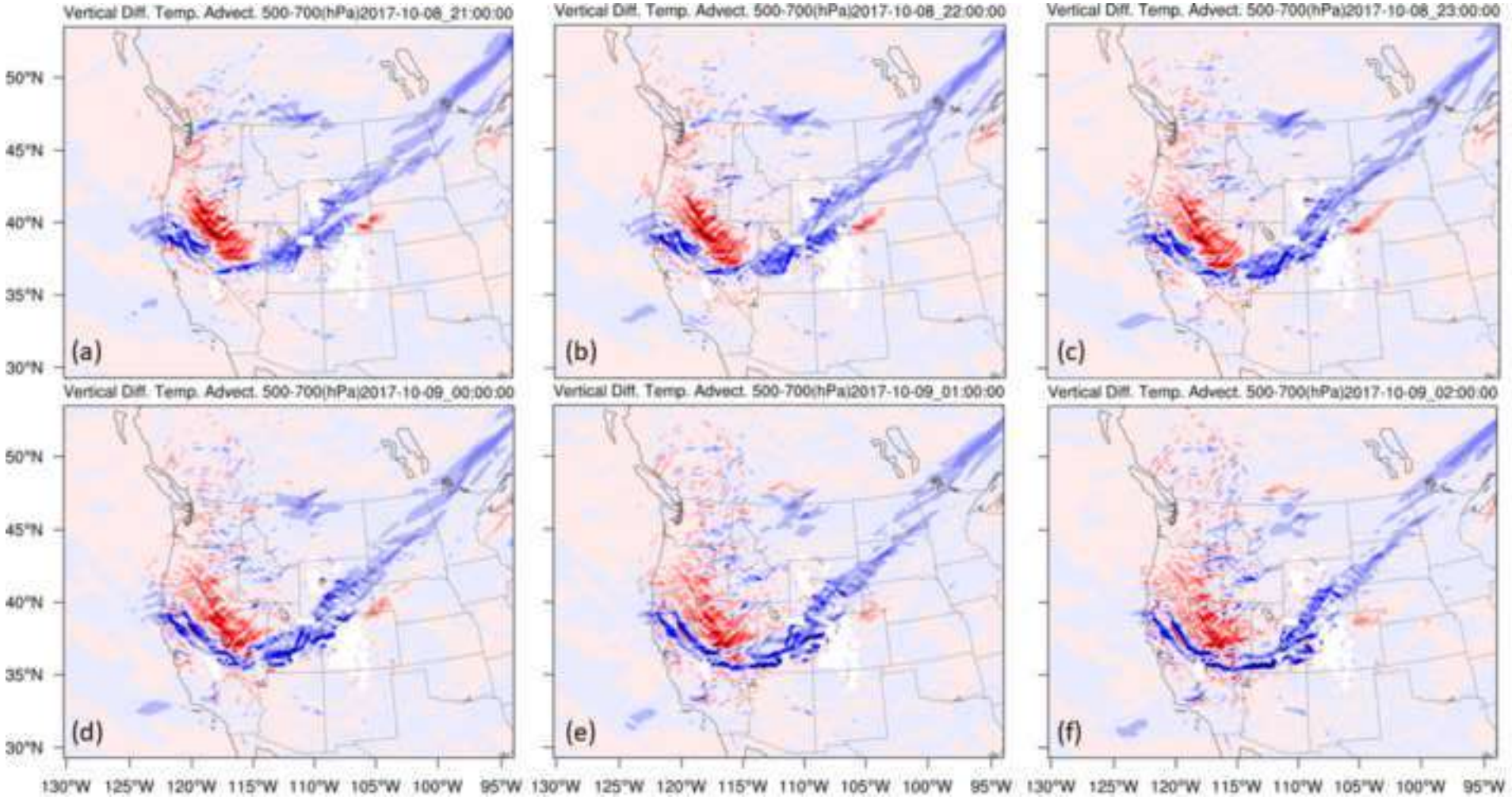

Figure 15b

Click here to access/download;Figure;Figure 15b.PNG

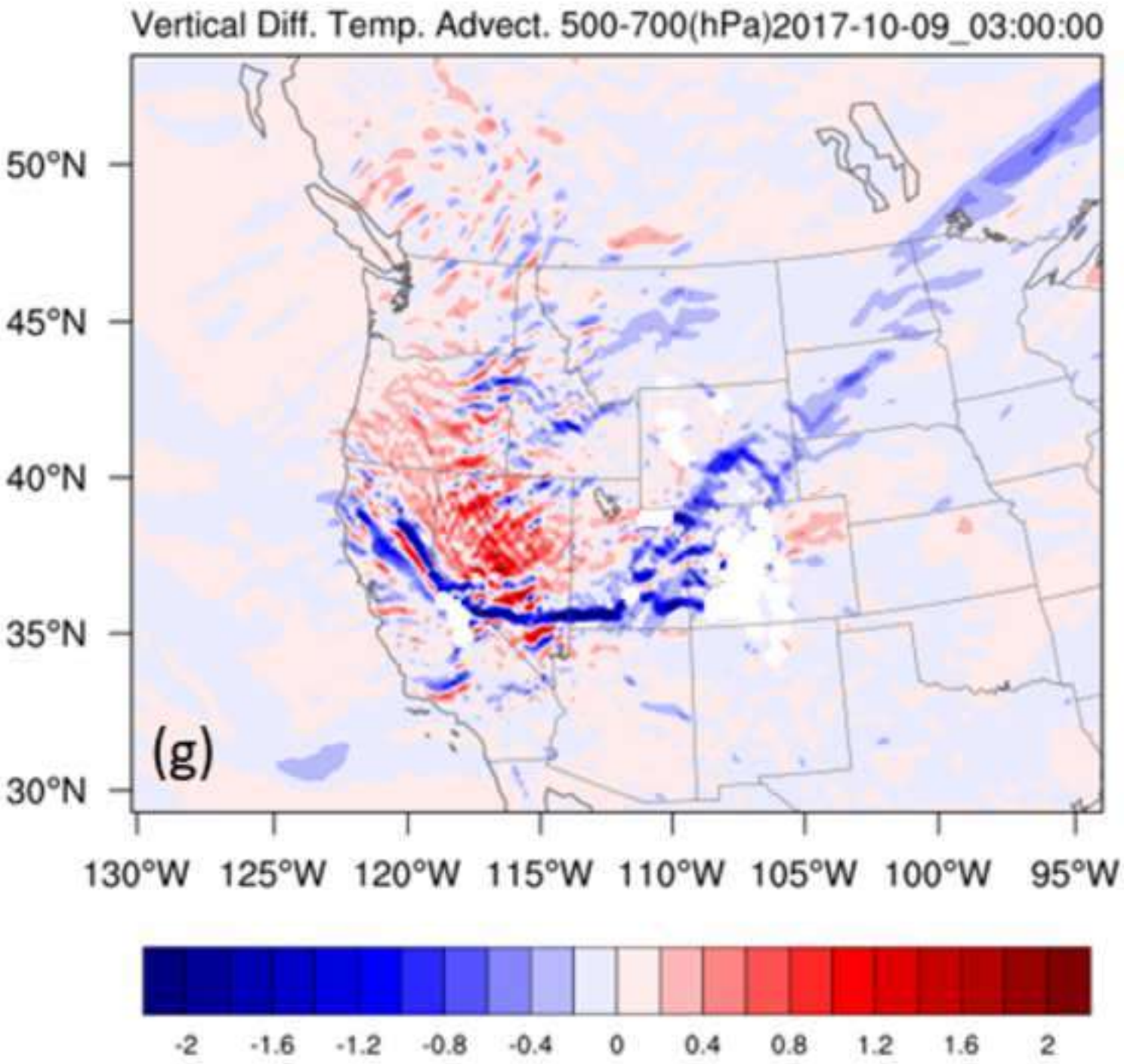

Figure 16

Click here to access/download;Figure;Figure 16.PNG

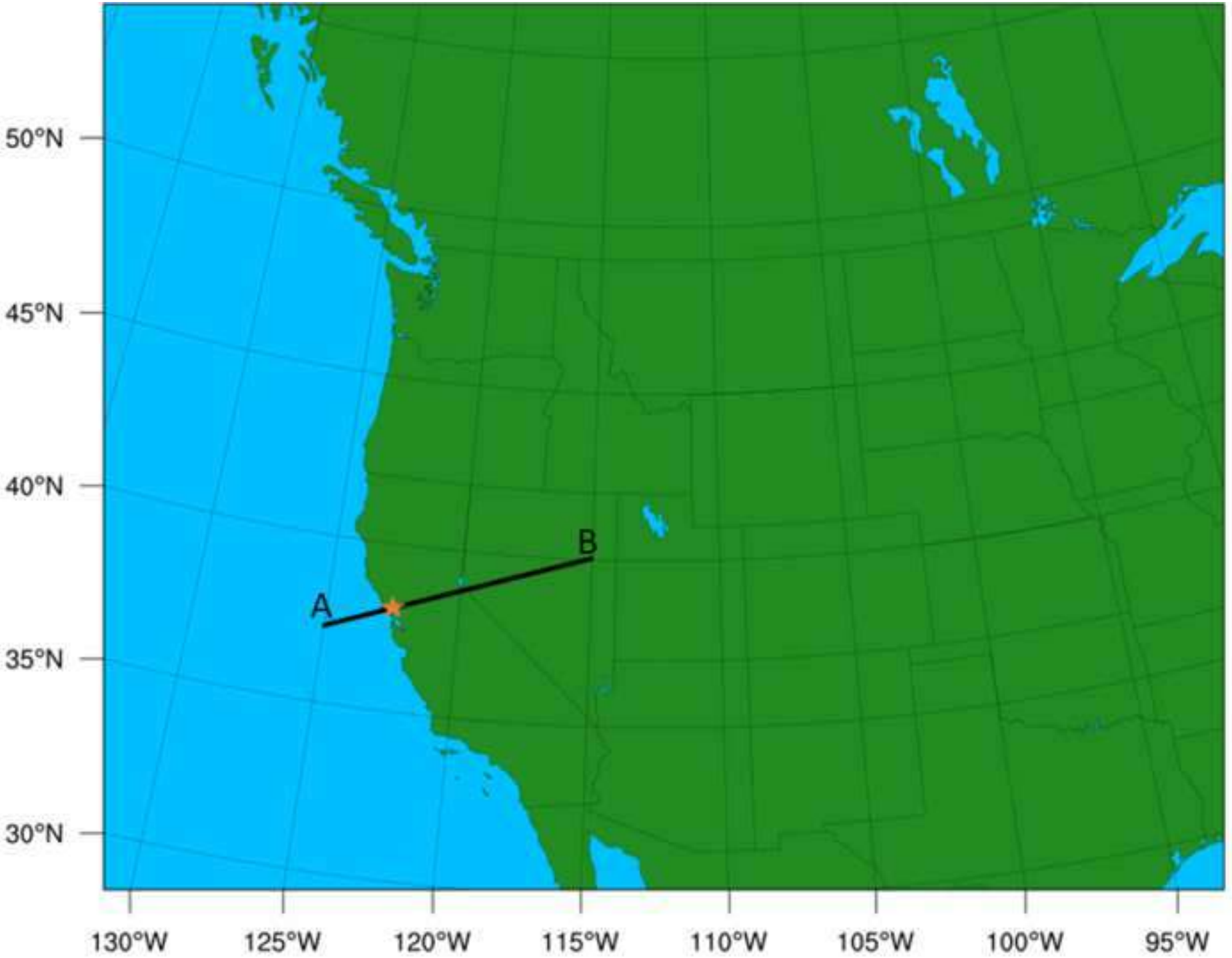

Figure 17a

Click here to access/download;Figure;Figure 17a.PNG

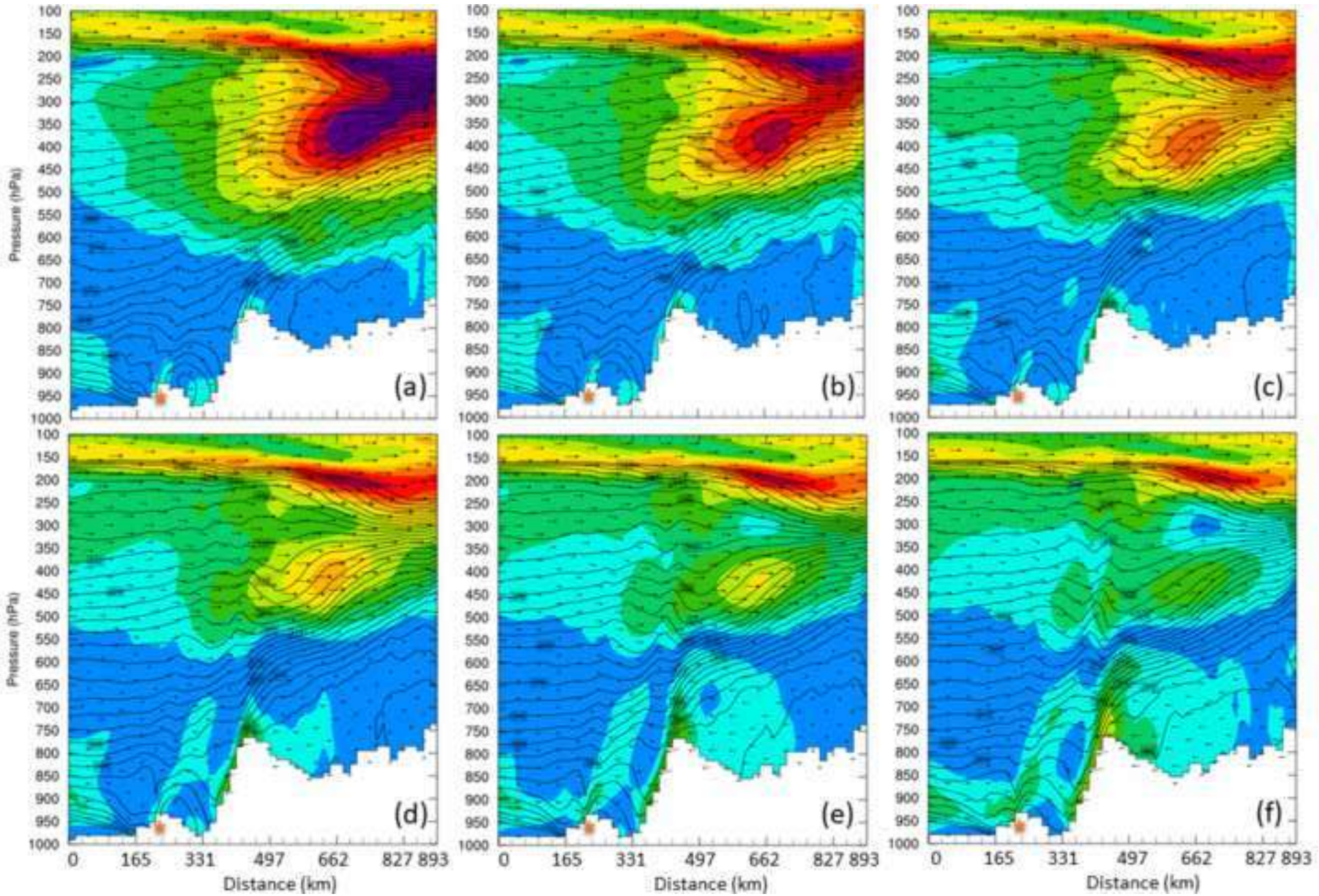

Figure 17b

Click here to access/download;Figure;Figure 17b.PNG

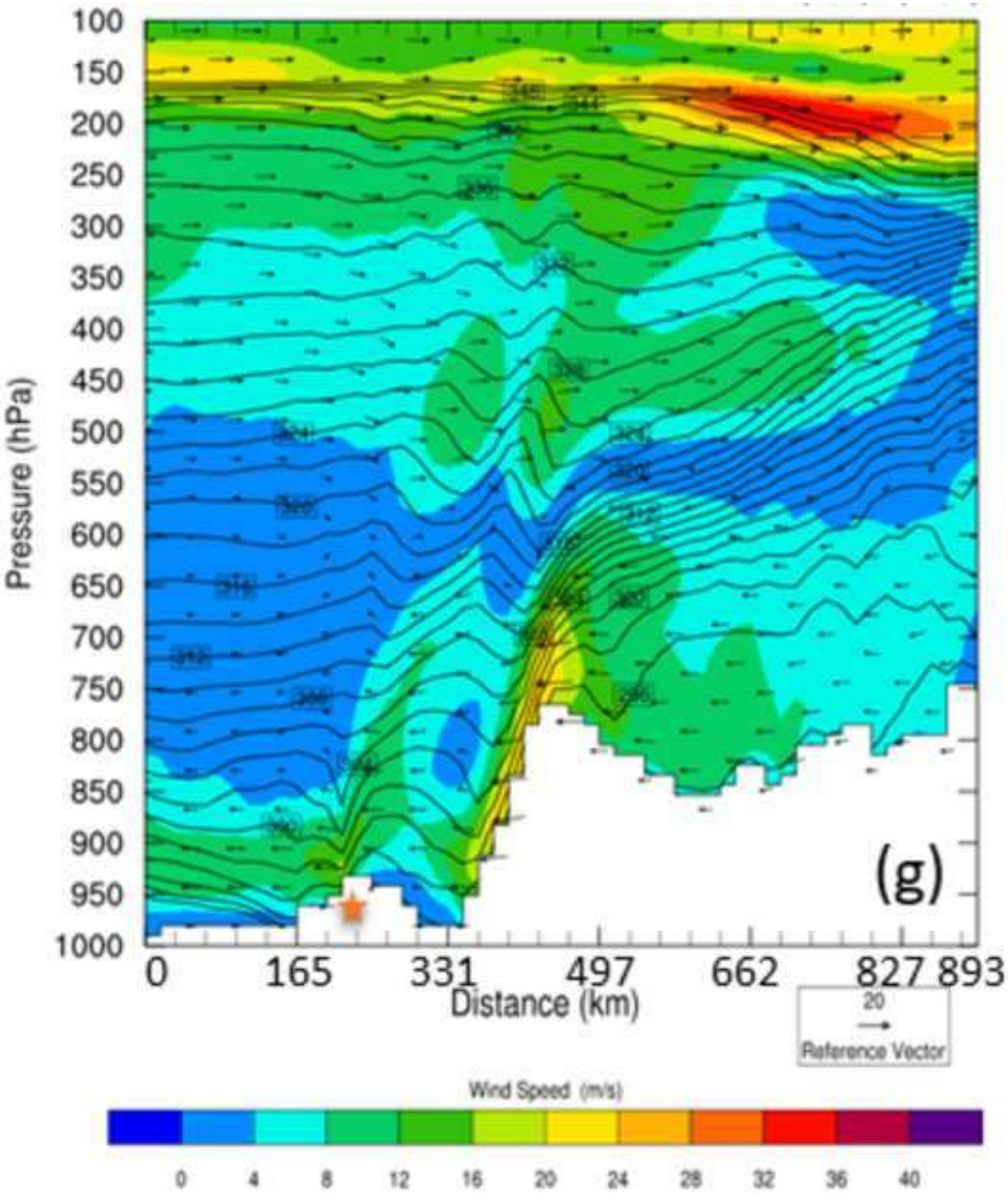

Figure 18a

Click here to access/download;Figure;Figure 18a.PNG

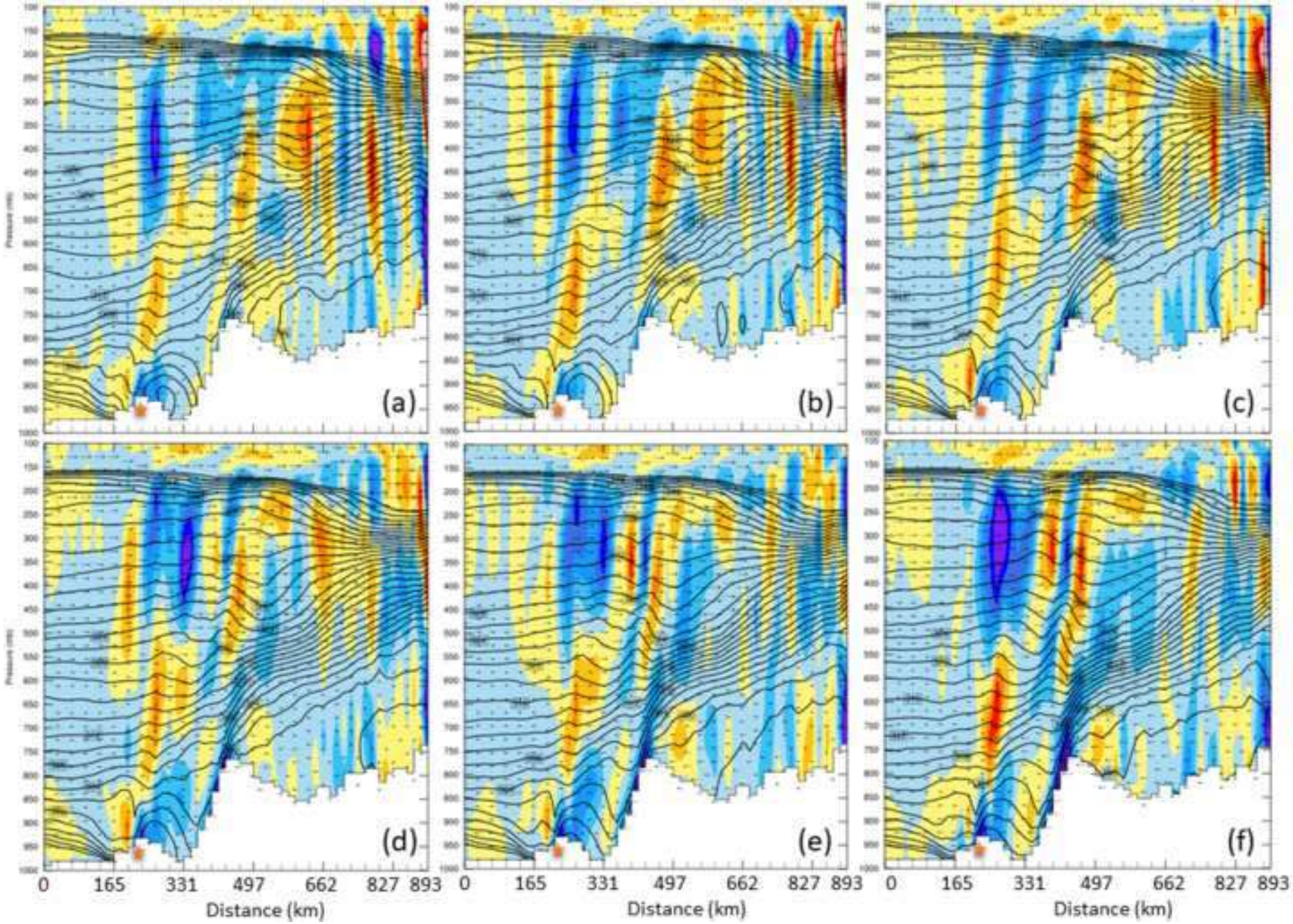

Figure 18b

Click here to access/download;Figure;Figure 18b.PNG

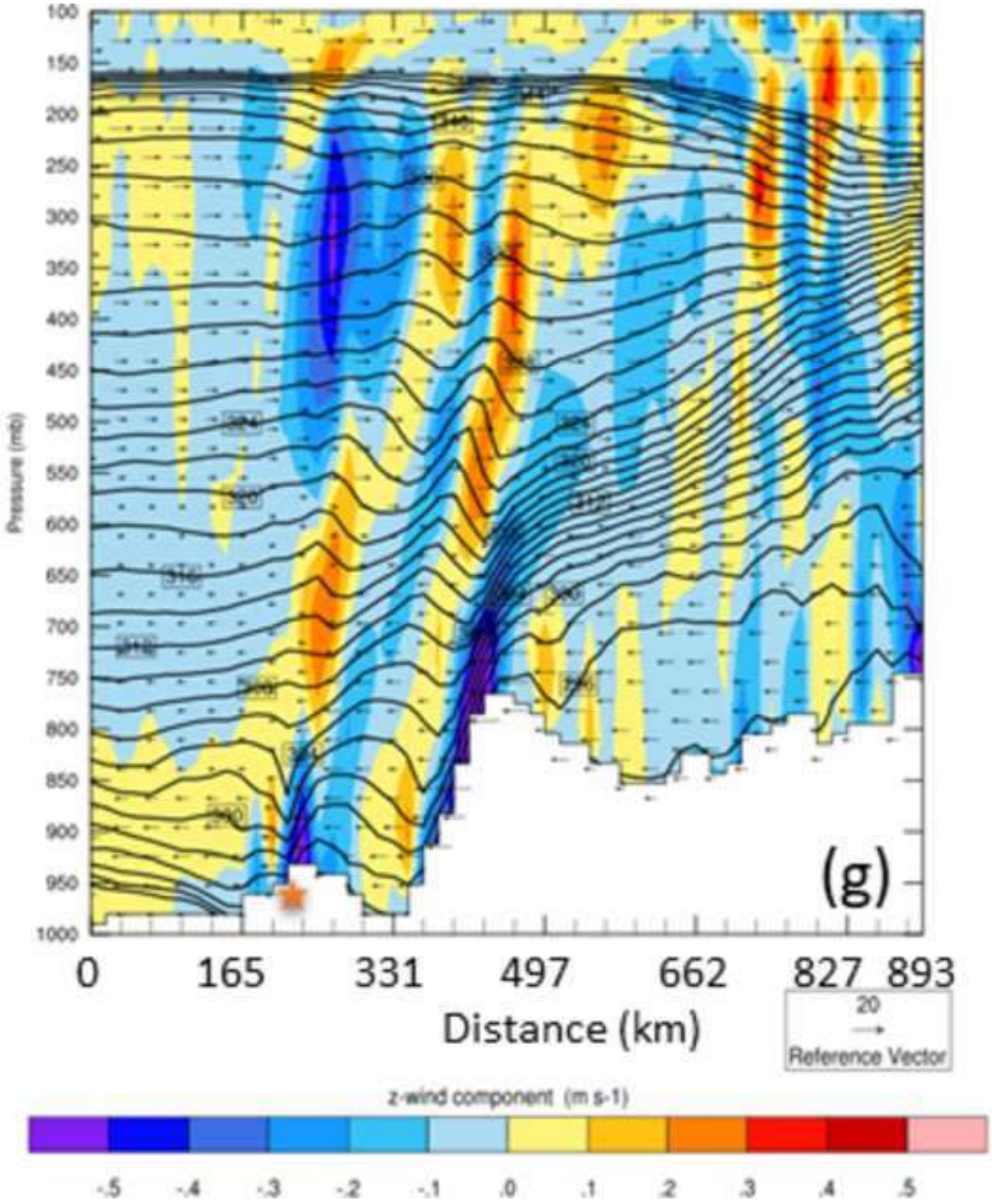

Figure 19

Click here to access/download;Figure;Figure 19.PNG

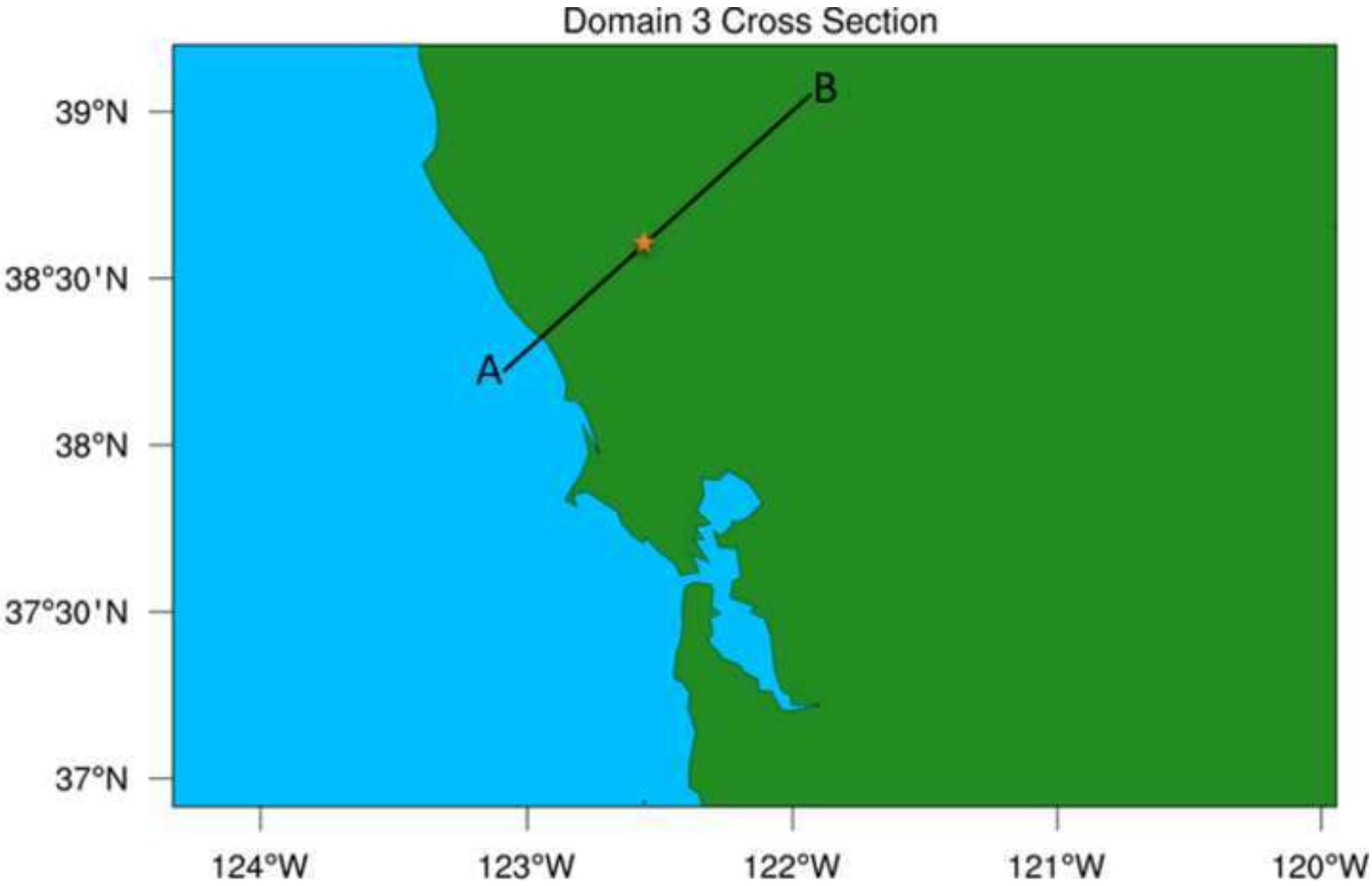

Figure 20

Click here to access/download;Figure;Figure 20.png

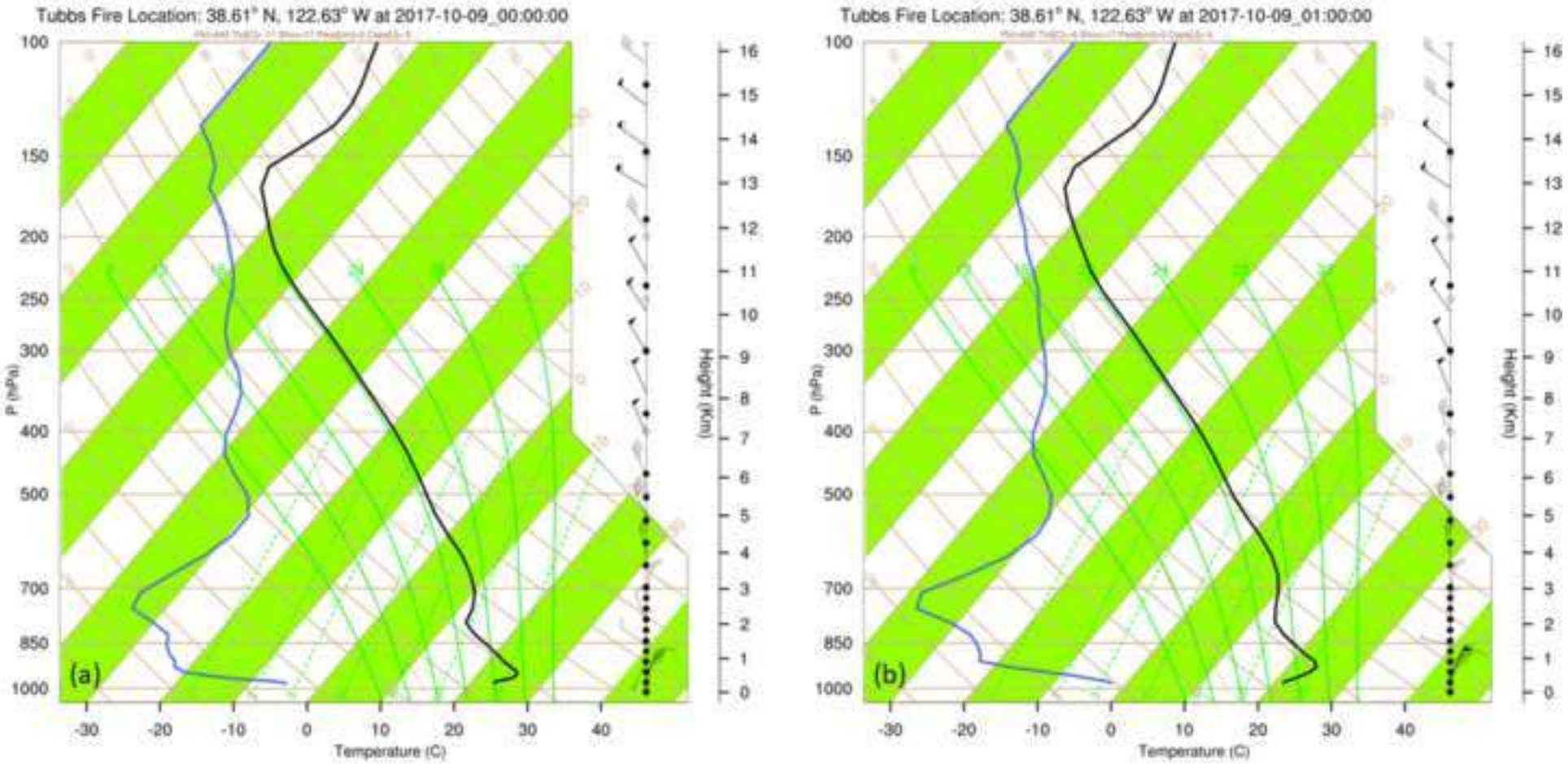

Figure 21a

Click here to access/download;Figure;Figure 21a.PNG

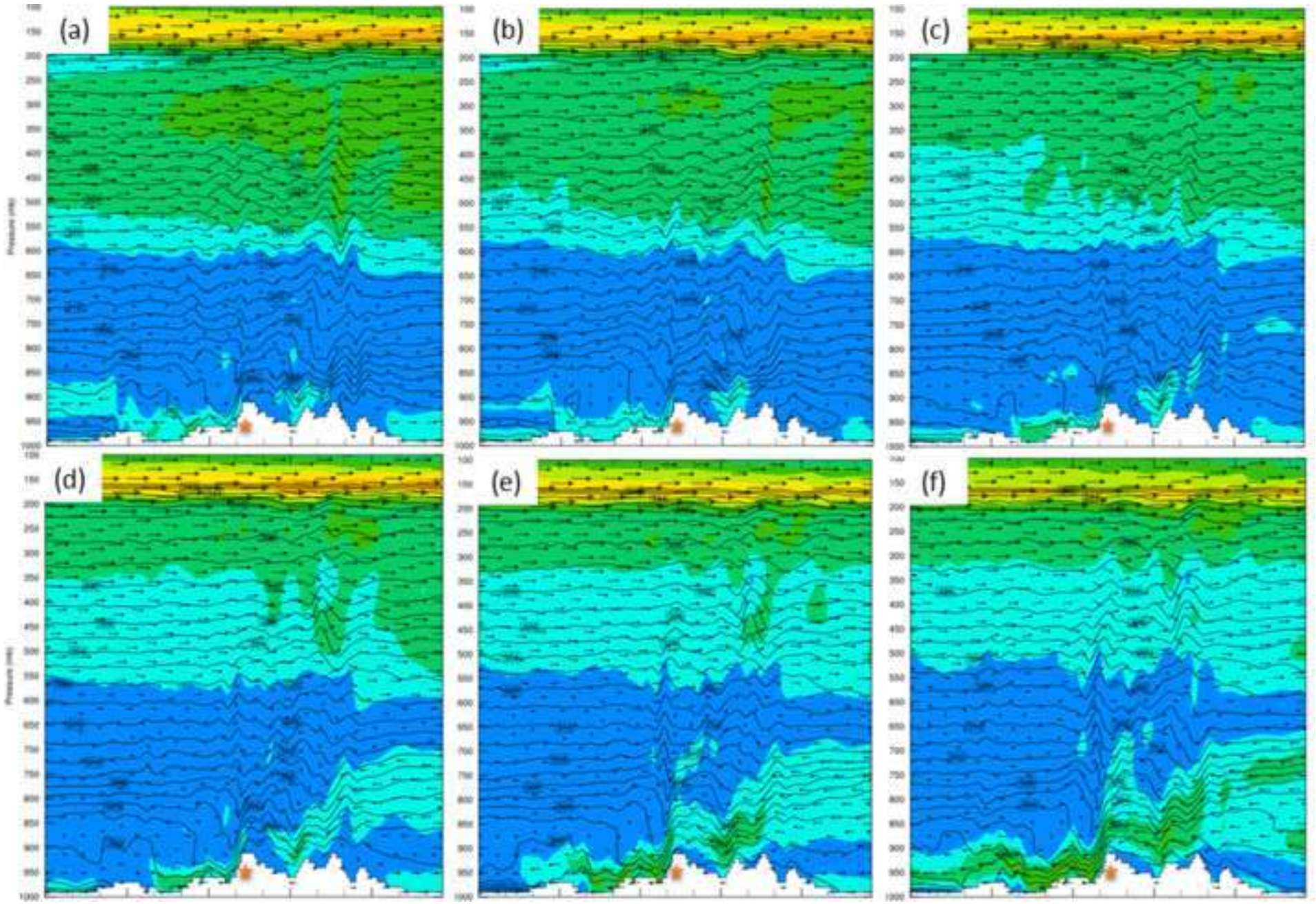

Figure 21b

Click here to access/download;Figure;Figure 21b.PNG

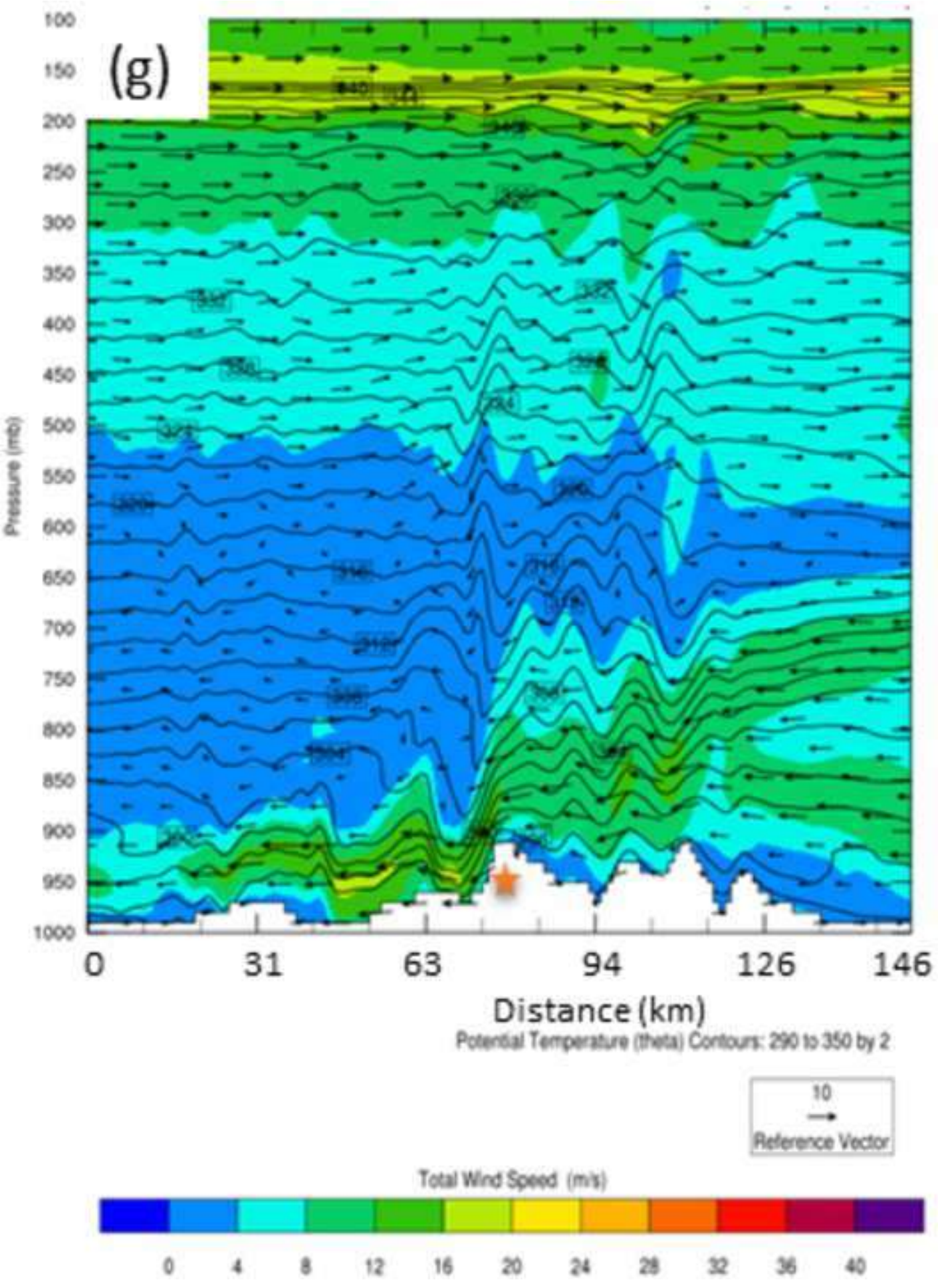

Figure 22

Click here to access/download;Figure;Figure 22.PNG

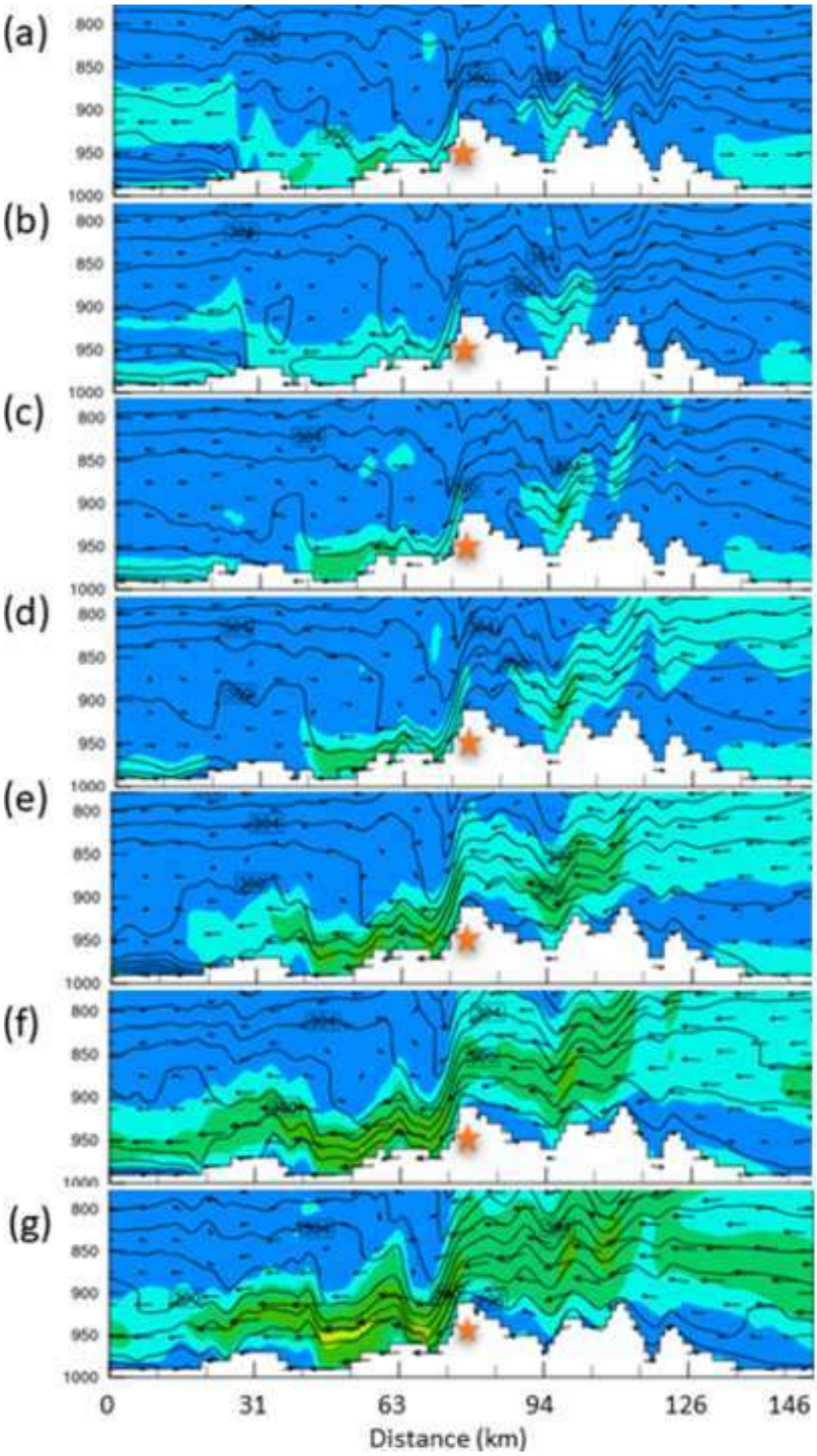

Figure 23a

Click here to access/download;Figure;Figure 23a.PNG

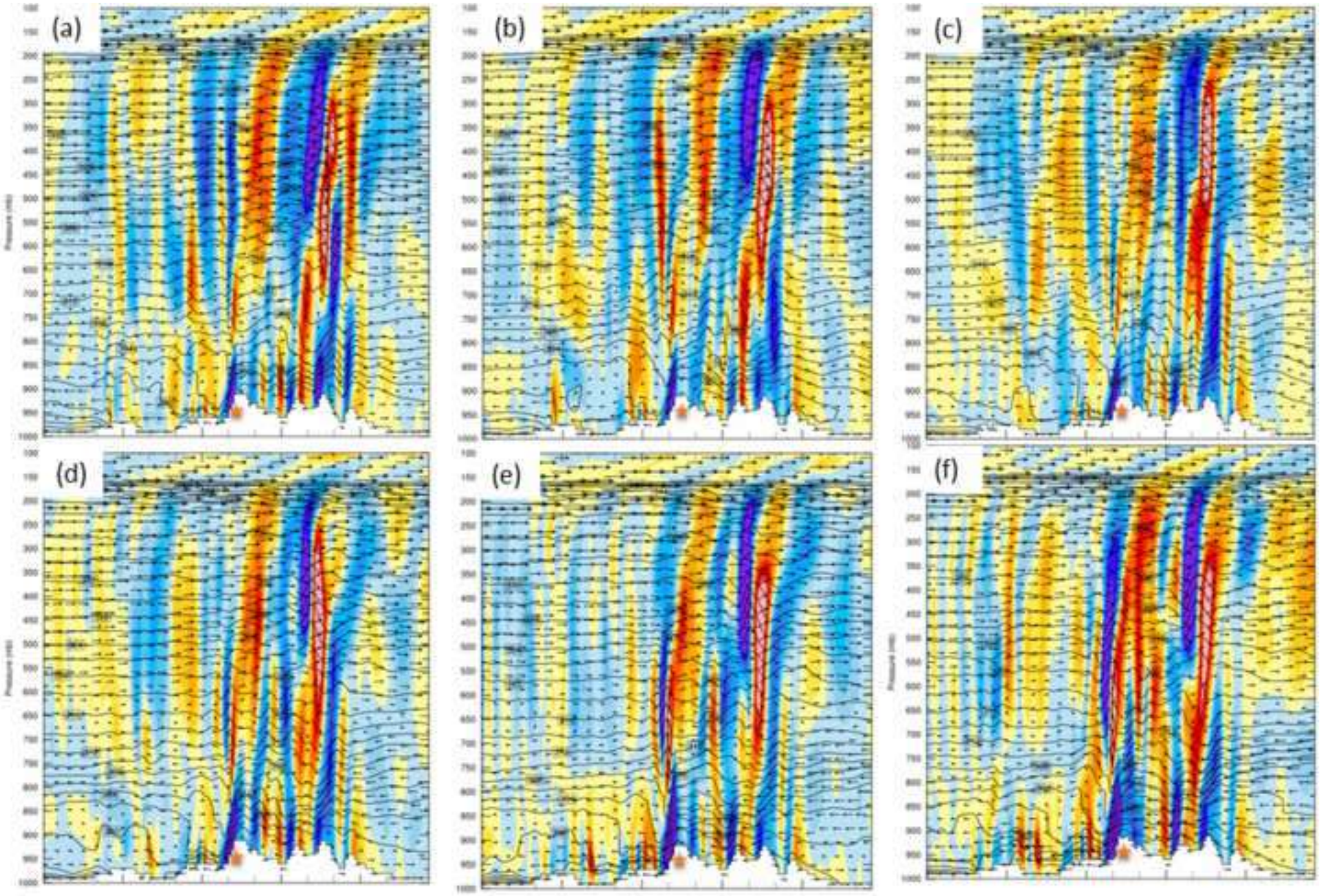

Figure 23b

Click here to access/download;Figure;Figure 23b.PNG

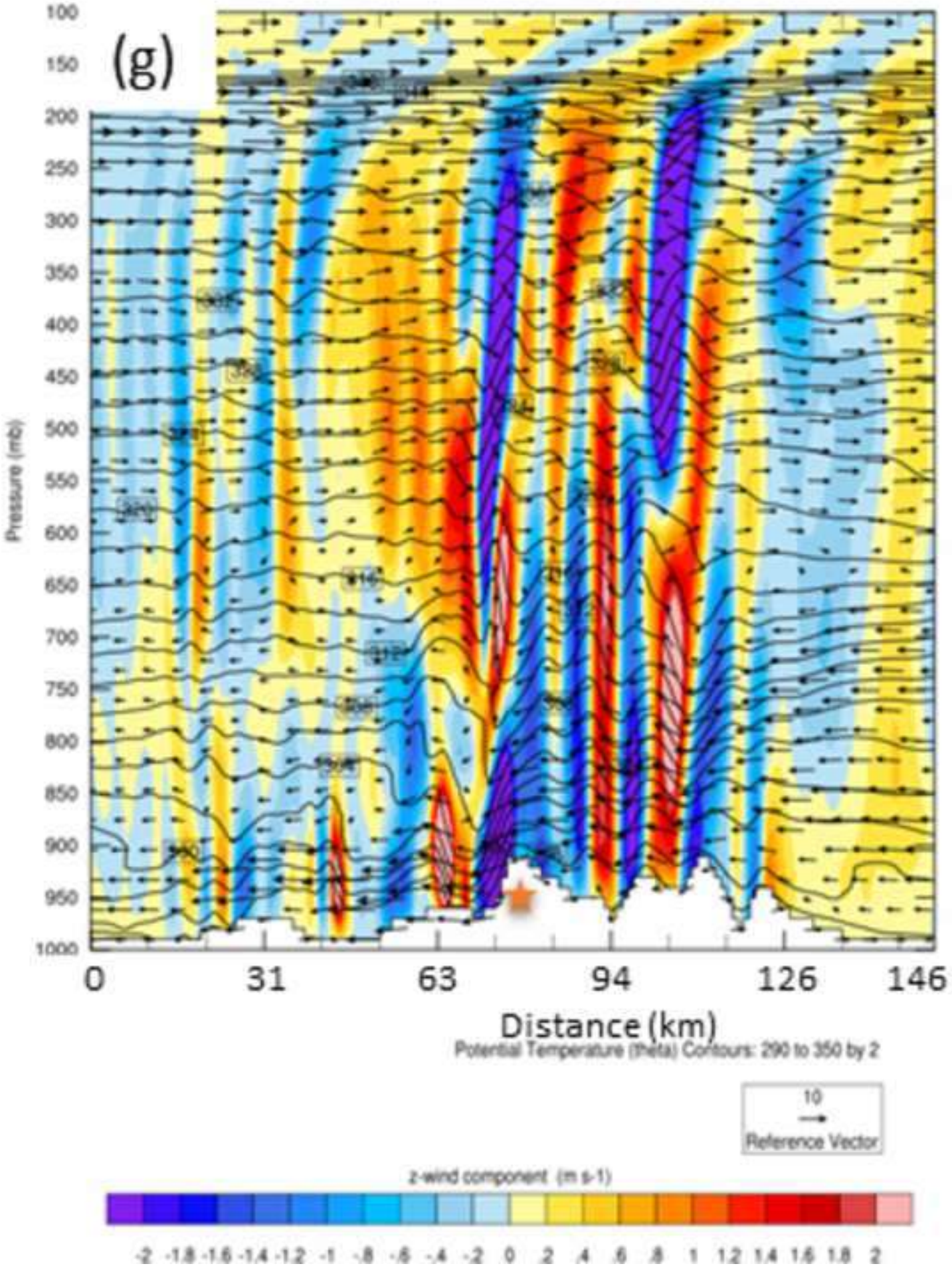

Domain	Grid points	Resolution (dx, dy)	Start	End
1	235 x 186	16km x 16km	October 8, 2017, 12 UTC	October 9, 2017, 12 UTC
2	505 x 369	4km x 4km	October 8, 2017, 15 UTC	October 9, 2017, 12 UTC
3	405 x 269	1km x 1km	October 8, 2017, 18 UTC	October 9, 2017, 12 UTC